Characterization and Modeling of Low Twist Yarn Mechanics in Tubular Braided Composites

by

Benjamin Kin On Cheung

A thesis submitted in partial fulfillment of the requirements for the degree of

Doctor of Philosophy

Department of Mechanical Engineering
University of Alberta

Abstract

Twisted yarns are commonly used in traditional textiles applications, such as in apparel manufacture, but their study and use in composite textiles is limited, especially in the case of continuous multifilament yarns. In textiles applications, small amounts of twist have shown to increase the strength of yarns, yet the increase in fiber obliquity contributes to a decrease in effective stiffness of the yarn. A specific emphasis on low levels of twist exists since higher levels of twist are not practical or feasible. It is proposed that including twist in the manufacturing process for textile composites can have a positive impact on the mechanical performance of tubular braided composites (TBCs), due to their strong correlation of performance to manufacturing parameters. The use and analysis of twisted yarns in TBCs was systematically approached by building up from single textile yarns to single composite strands and eventually up to TBCs. This approach allowed for the impact of twist to be observed at each scale of testing. Dry textile yarns were tested to determine the impact of twist and confirmed what was noted in existing literature; that is, an increase in strength and a decrease in effective stiffness. It was also shown that existing yarn twist models do not accurately capture the stiffness response of low twist yarns. Following this, composite strands were tested under the same twist levels and it was determined that yarn twist has much less of an impact when in the presence of a composite matrix. Finally, TBCs were manufactured with yarn twist to determine the impact at the scale of a composite textile and tested under tension. Digital image correlation (DIC) is used for these experiments in order to capture the full field strain behaviour. The presence of twisted yarns in the TBCs is found significantly increase yield strength without negatively impacting the stiffness response. This increase in stress capacity is then modeled by means of the Ramberg-Osgood equation, which accounts for both an increase in strength as well as a change in plastic strain behaviour. Throughout this thesis, two different yarn materials are used for each study.

The first, Kevlar 49, is a traditional choice for composite reinforcement due to its high stiffness to weight ratio, and there is much literature on the mechanical behaviour of Kevlar 49 as a composite constituent. As well, a more novel cellulose-derived multifilament yarn BioMid was also used in parallel. Using two different types of continuous multifilament yarns also confirms whether or not the effects observed are specific to the material used.

Preface

A portion of Chapter 2, specifically section 2.2, was previously published as a chapter "Handbook of Advances in Braided Composite Materials: Theory, Production, Testing and Applications: Micromechanics". I was responsible for manuscript, equation, and figure generation, while J.P. Carey was the supervising editor. Chapter 3 is my original work. Chapter 4 was submitted for publication to the Journal of Engineered Fabrics and Fibers under the title "Characterizing and Modeling of Low Twist Yarn Mechanics" and was recommended for publication pending minor revisions in April 2019 and accepted for publication on July 4, 2019. Chapter 5 is my original work. Chapter 6 is my own work including sample manufacture, testing, analysis and manuscript generation. Chapter 7 is my original work as well, including all analysis and code. J. P. Carey assisted with manuscript editing throughout this work.

Dedication

This work is dedicated to my daughter, Ruth, who came into this world as I was writing this thesis and put life in perspective. May you grow up asking hard questions and never stop searching for the truth.

Acknowledgements

I would like to take this opportunity to thank the people who have made this work possible. This is far from an exhaustive list, as I believe that “it takes a village to raise a child”. To my supervisory committee, thank you for challenging me and ensuring that I put my best foot forward. Specifically Jason, thank you for your guidance and mentorship along the way, and for allowing me to explore my passions as a teacher and develop my skills as a researcher and member of the academic community. I’m on the other side of the desk now.

Thank you to the members of the Carey Lab, past and present, for your friendship, your support, your discussions, and your banter. May you all find success in your pursuits and may your coffee cup never be empty.

Thank you to my parents, for never assuming I was too young to learn something new.

Last but not least, thank you to my wife Beth. Your love, support, and faith have carried me through much of this journey, and I look forward to the next great adventure.

Thank you all.

Table of Contents

List of Tables

List of Figures

List of Symbols and Abbreviations

σ	Normal stress
ε, ϵ	Strain
E	Modulus
ν	Poisson's ratio
v	Volume
V	Volume fraction
P	Load
A	Cross sectional area
L, l	Length
$[S]$	Compliance
$[R]$	Reuter's matrix
$[T]$	Transformation matrix
θ	Twist angle
α	Surface twist angle
h	Height
R, r	Radius
n_f	Filament count
d_f	Filament diameter
ρ	Density

List of Subscripts

1	Longitudinal direction (aligned with tensile load)
2	Transverse direction (perpendicular to tensile load)
3	Out-of-plane direction (perpendicular to tensile load)
c	Composite
m	Matrix
f	Fiber
y	Yarn

Chapter 1 Introduction

1.1 Motivation

Mechanical modeling of composite materials has traditionally been concerned with constituent properties and orientation. In textile composites, this approach neglects some of the steps taken in textile manufacture, such as yarn twist, since the overall impact on fiber orientation is minimal. In textile applications, such as apparel manufacture, twisted yarns have been shown to exhibit improved strength over their untwisted counterparts [1]. This is true both for short fiber applications, where twist is essential to creating a continuous yarn, and continuous fiber applications where twist is not required [2]. Often, manufacturers will add some level of twist known as producer's twist to improve handling of multifilament yarns in textile applications [3], but the use of yarn twist in textile composites has been limited and in modeling these materials is often ignored or omitted [4]. Here, I propose that the impact of yarn twist is not negligible to mechanical performance of tubular braided composites (TBCs). Tensile testing of dry yarns, unidirectional composites, and TBCs will be performed with and without twisted yarns.

1.2 Outline

This thesis covers a systematic approach to the use of low twisted yarns in multifilament TBCs and aims to highlight the impact twisted yarns have on the mechanical performance of textile composites. The chapters of this work are organised to reflect the approach taken.

Chapter 2 covers a literature review of the fundamental composites and textiles definitions and concepts used throughout, as well as a brief discussion on existing predictive models for TBCs.

In Chapter 3 the experimental methods used are discussed in detail. Some of the content in this chapter may overlap with others due to some of the work being previously submitted for publication.

In Chapter 4, the tensile properties of two different textile yarns are compared at different levels of twist. Kevlar® 49 is used due to its large body of literature as well as its high-performance tensile properties. BioMid® is used as a more novel material, being manufactured from cellulose and to attempt to evaluate its potential as a green alternative to petroleum-derived high-performance fibers. Predictive elastic models are compared to the experimental results.

In Chapter 5 tensile tests on twisted and untwisted composite strands are performed, using the same textile yarns as in Chapter 3. The tensile response of these strands with respect to twist is compared to that of the dry yarns. In this case it is found that the effect of twist can vary across yarn types and that the impact of twist is reduced in the presence of a composite matrix.
In Chapter 6 TBCs are manufactured with and without twisted yarns, and the tensile response is compared. There is a negligible change in stiffness properties of the TBCs, but a significant increase in tensile yield strength.
In Chapter 7 an attempt is made to model the plastic zone of the stress-strain response of TBCs, in response to the significant change in tensile yield strength observed in Chapter 6. The Ramberg-Osgood equation is used to model the plastic stress-strain behaviour of tubular braided composites beyond the elastic zone up to the yield point. Previous studies have covered the modeling of elastic region but to date there have been no studies on modeling this region of the tubular braided composite loading curve.

Chapter 2 Literature review

2.1 Tubular braided composites

Tubular braided composites are a type of textile preform composite. Textile braids are classified by their braid pattern and their cross-section, which are a product of the manufacturing method and parameters used [5]. Figure 2-1 shows a tubular textile braid during manufacture.

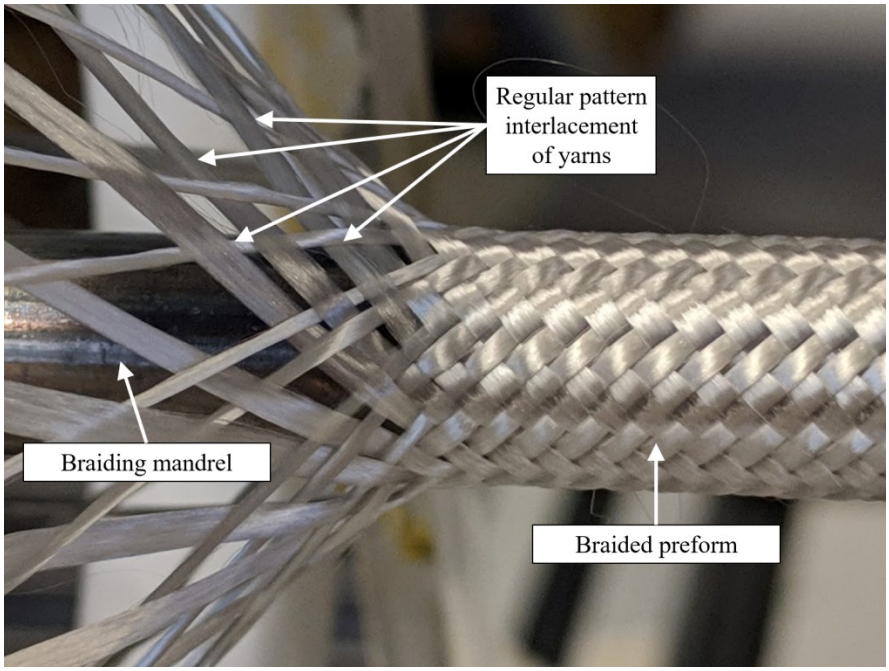

Figure 2-1: Image of braid during preform manufacture.

One of the ways in which braids are manufactured is through the use of a maypole braider [6], as shown in Figure 2-2.

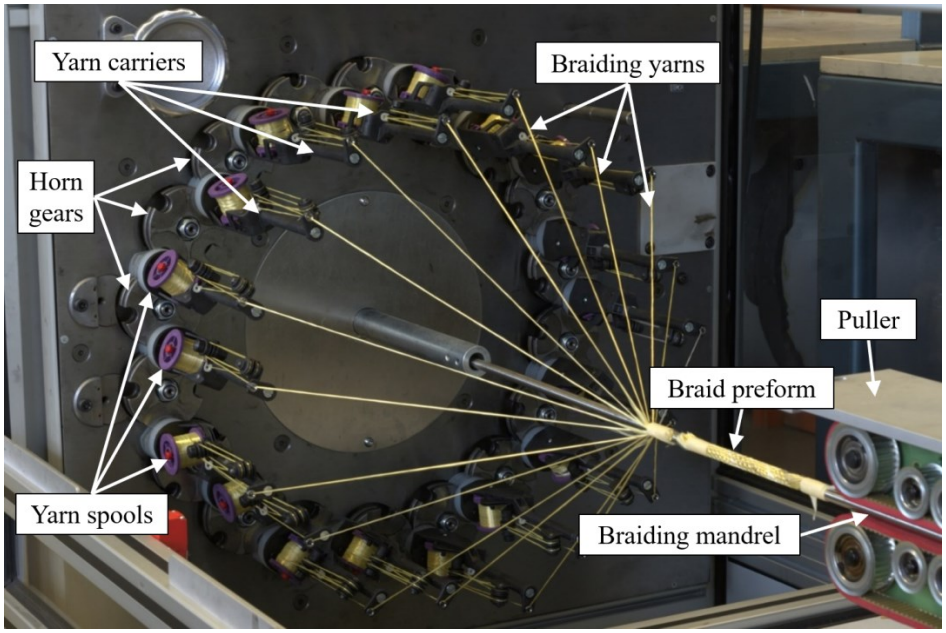

Figure 2-2: Image of braid during preform manufacture.

The maypole braider produces the tubular braid through the relative motion of the braiding mandrel and the braiding yarns [7]. In a circular maypole braider, the braiding yarns each move in a circular path in plane perpendicular to the direction of the braiding mandrel. The braiding yarns interlace with each other as the mandrel moves away from the yarn carriers and the tubular braid is laid onto the braiding mandrel, the final position determined by the tension in the system [8], [9]. A detailed explanation on the braiding process of a maypole braider will be discussed in section 3.3.4.2.

2.1.1 Direction terminology

Given the multiscale aspect of this work, numerous directions and angles will be used throughout. For the sake of consistency these will be defined exhaustively here.

Braid direction refers to the direction collinear with the longitudinal axis of the tubular braid, as denoted by e_1 in Figure 2-3. Yarn direction refers to the direction collinear with the path of the individual braiding yarn (e_y). Filament or fiber direction refers to the direction collinear to the individual filament (e_f). These subscripts will be consistent throughout.

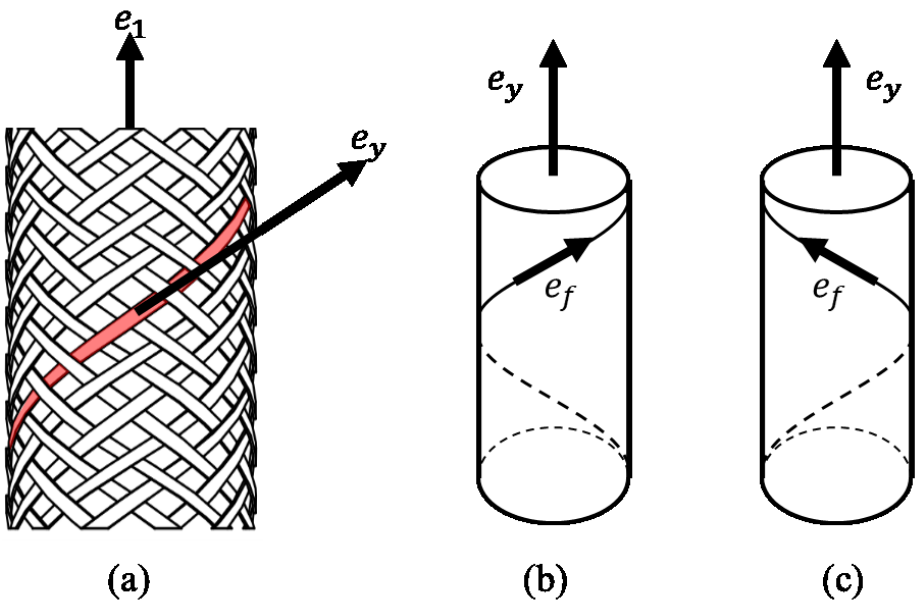

Figure 2-3: Sketches denoting the directions of yarns in a braided structure (a) and twist in twisted yarns (b) and (c). The sketch in (a) shows the braid structure with the longitudinal axis direction e_1 and the direction of the Z-yarn, e_y. This yarn may be twisted in either a Z-twist (b) or S-twist (c) configuration.

When describing helical directions, the textile terminology of "Z" and "S" will be used for identifying both the twist in yarns and the helical paths of the braid yarns. It refers to the direction of the foreground portion of the yarn or filaments (Figure 2-3 (b) and (c)).
In a woven material, the interlacing yarns are referred to as warp and weft yarns [10]. This nomenclature has been use for braids [7], [11], even though this implies they are handled differently in the manufacturing process. For braids, the only difference between each set of yarns is the direction of carrier travel; the tension and handling of each is identical. Thus, in this work we will refer to each set of braiding yarns based on the helical directions, and will use the S- and Z- nomenclature for clarity.

2.1.2 Braid architecture

The interlacement pattern creates the braiding pattern, of which three primary braiding patterns are typically used and are known as Diamond (1/1), Regular (2/2), and Hercules (3/3) patterns [11]. Figure 2-4 provides three views of the Diamond braiding pattern.

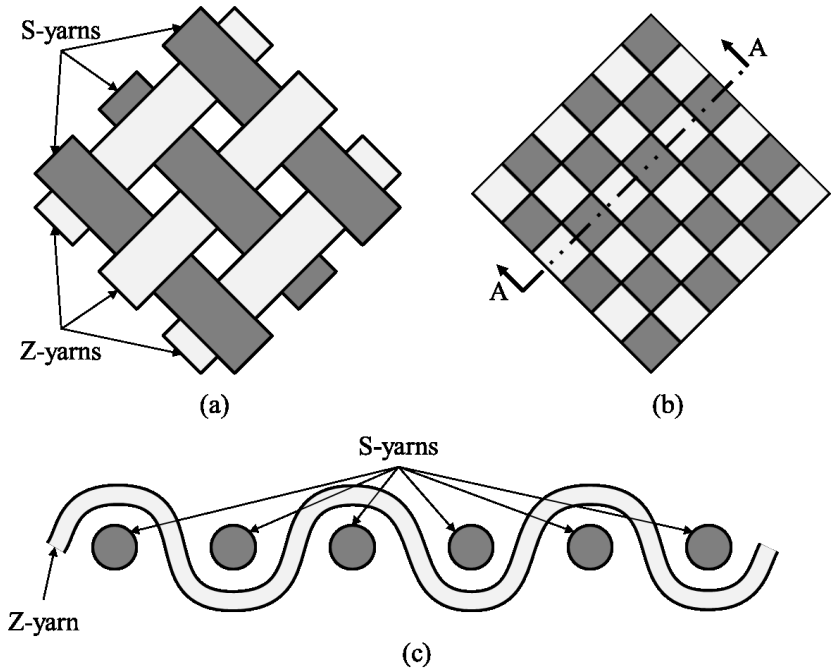

Figure 2-4: Diagrams of Diamond braid architecture;; (a) flattened and exploded view of yarn interlacing, (b) flattened braid pattern, and (c) section view A-A showing one-over, one-under path of braiding yarns in the braiding direction

Here, each yarn passes over and then under the yarns in the opposite helical direction, forming the 1/1 pattern seen in Figure 2-4 (b). This is known as the Diamond or 1/1 braiding pattern. Next the Regular braiding pattern is shown in Figure 2-5.

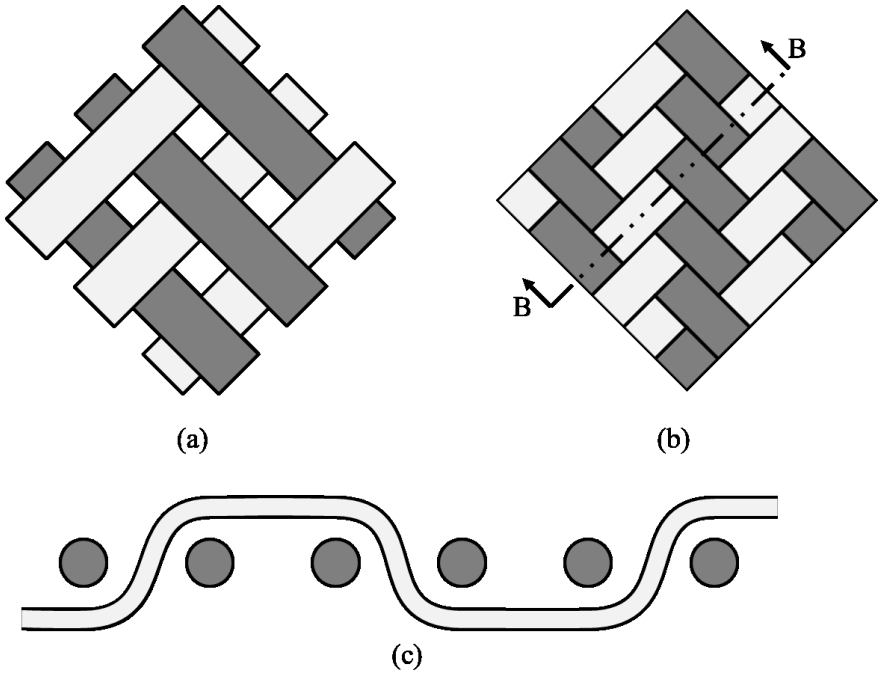

Figure 2-5: Diagrams of Regular braid architecture; (a) flattened and exploded view of yarn interlacing, (b) flattened braid pattern, and (c) section view B-B showing two-over, two-under path of braiding yarns in the braiding direction

In this case each yarn first passes over two interlacing yarns, then under two interlacing yarns. This is known as the Regular, Herringbone, or 2/2 braid pattern. Finally there is a third common pattern known as the Hercules braid, shown in Figure 2-6.

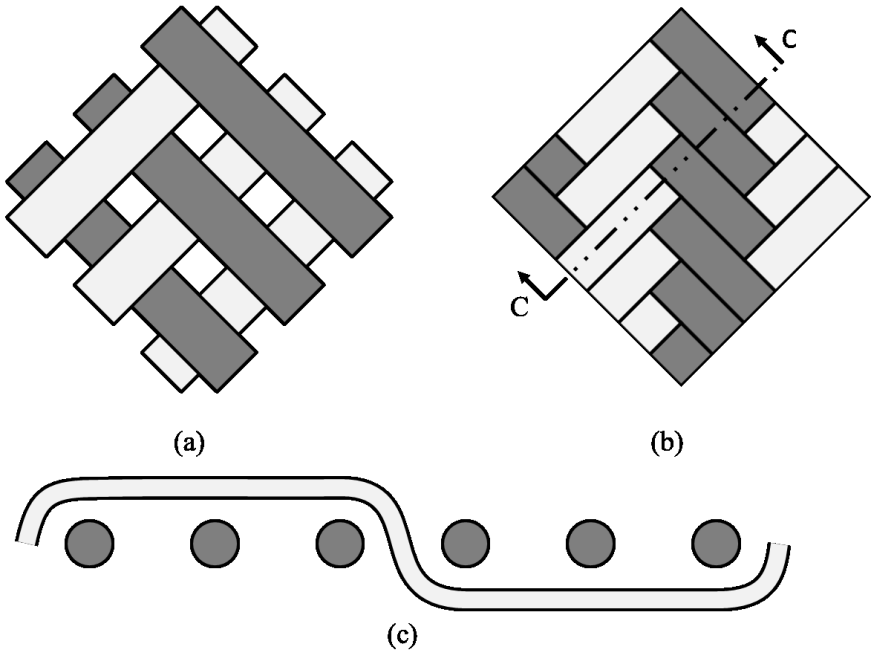

Figure 2-6: Diagrams of Hercules braid architecture; (a) flattened and exploded view of yarn interlacing, (b) flattened braid pattern, and (c) section view B-B showing two-over, two-under path of braiding yarns in the braiding direction

This braid passes over and then under three consecutive interlacing yarns.

Specifically, the type of preform manufactured by the circular maypole braiding process shown in Figure 2-1 is known as a biaxial or 2D tubular braid, referring to the two directions the reinforcing yarns can take within the textile structure [12]. The yarns can be deposited onto a braiding mandrel that is later removed, yielding a hollow tubular structure, or can be deposited onto another core medium for additional reinforcement [13], [14]. Triaxial tubular braids can also be manufactured by adding a set of reinforcing yarns that run parallel to the mandrel direction [6], [15], known as axial or zero degree yarns, further reinforcing the longitudinal axis of the braid as shown in Figure 2-7.

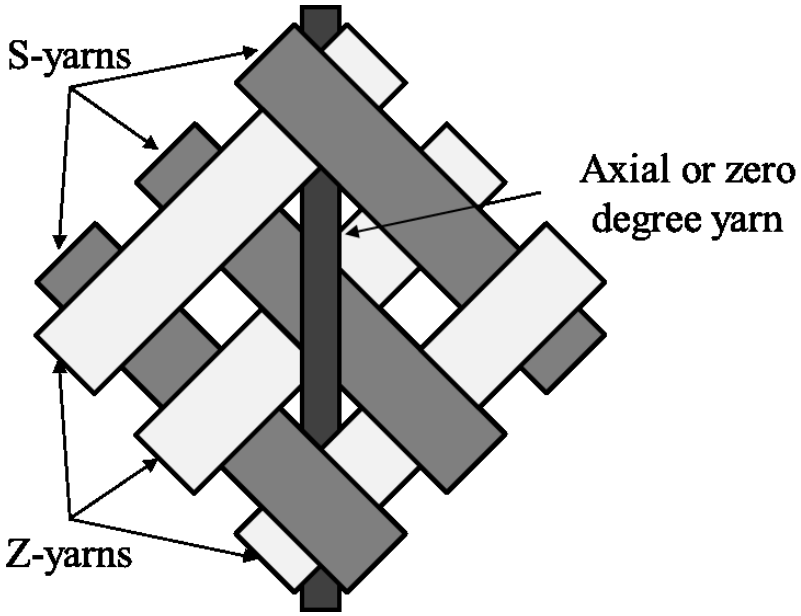

Figure 2-7: Schematic of triaxial Regular braid pattern

Alternative braid manufacturing configurations include flat braids [16]–[18] and various types of 3D braids, including tubular [19] and multi-directional [20]–[22]configurations. This work will be limited to the study of biaxial, single layer tubular braided structures only.

Braids have various applications as a textile preform, but these will not be discussed here. Rather, when impregnated with a matrix such as one made of thermoset epoxy resin, a tubular braided composite (TBC) can be manufactured. These TBCs are being explored for a variety of applications where high stiffness- and strength-to-weight applications are desirable. TBCs are desirable composite structures due to their adaptability to various preform shapes [23], [24] and customizability for stiffness critical applications [25], making it a viable material in aerospace [25], medical [26], [27], automotive [28], and construction [29], [30] applications.

Before attempting to discuss the more complex macro scale modeling of a tubular braided composite, we will begin by establishing conventions and definitions from both the composites and textiles fields. Beginning with a brief introduction to TBCs and directional terminology, we will follow with a basic discussion in micromechanics, the basis of most stiffness modeling in composite materials. Next, we will cover textile definitions and equations with regards to yarn twist. Finally, we will discuss the existing stiffness models for TBCs.

2.2 Micromechanics[1]

2.2.1 Introduction

In order to develop and understand the basic stiffness models developed for twisted yarns and TBCs, it is important to first establish the basic micromechanical models on which these are based. For textile composites this involves defining the heterogeneous relationship of the fiber and matrix. Modeling the interactive behaviour of these constituents typically involves the use of some form of representative volume element (RVE); a building block for the larger scale micromechanical models. For the following sections, the subscripts f, m, c will be used for fiber, matrix and composite, respectively.

2.2.2 Mechanics of materials approach

The mechanics of materials approach is a widely accepted and fairly accurate approach in predicting the elastic behavior of a unidirectional composite. There are a few basic assumptions that must be made in this approach: (1) all the fibers are uniform in properties and in diameter; (2) the fibers are continuous and parallel throughout the composite; and (3) there exists a perfect bond between the fibers and the matrix with no slippage occurring between them. Once these assumptions have been accepted, the load behavior of the respective RVE is considered under different loading conditions.

In this section, load-sharing (or isostress) and deformation-sharing (or isostrain) will be used to describe and derive the relationship between the overall RVE response to loading and the response of the individual composite constituents. Consider the case of a heterogeneous material, such as that of a textile composite. There are two primary cases that can be considered, based on

The first case, known as isostrain or load-sharing, refers to the case where the material constituents are aligned parallel with the direction of load. In this case, the applied load is shared between the two constituents as shown in Figure 2-8; that is each takes on a different portion of the total overall applied load. It is assumed that the deformation of each is equal (hence the term isostrain) and the structural integrity of the original element is maintained.

[1] A version of this section was previously published in Handbook of Advances in Braided Composite Materials Theory, Production, Testing and Applications [6].

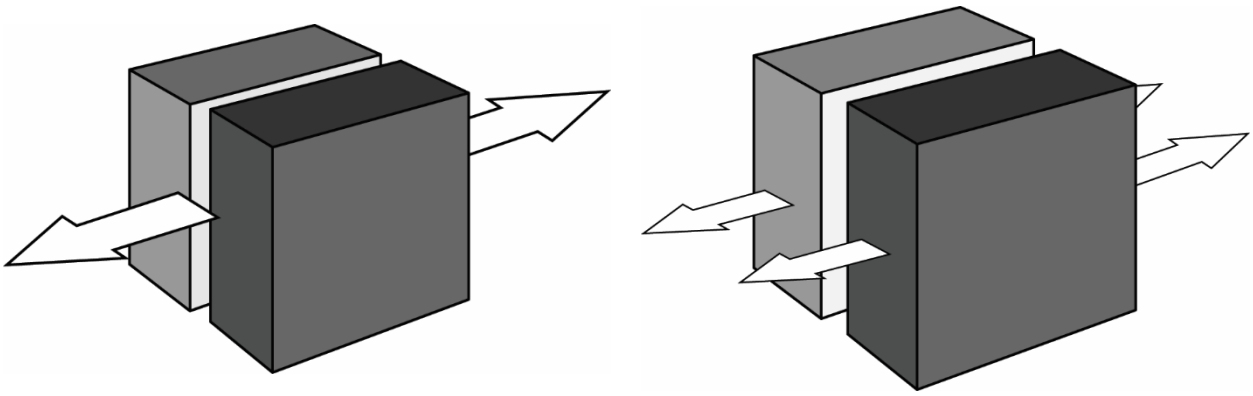

Figure 2-8: Schematic of heterogeneous element under load-sharing. In (a), the overall applied load is shown, where in (b) the division of the load between constituents is emphasized.

The next case is referred to as deformation-sharing, or isostress. As the name suggests, this is the alternative arrangement to load-sharing case where the constituents now share the deformation and the total load is applied to each individual component (hence the term isostress), as shown in Figure 2-9. One may also consider these elements to be loaded "in series".

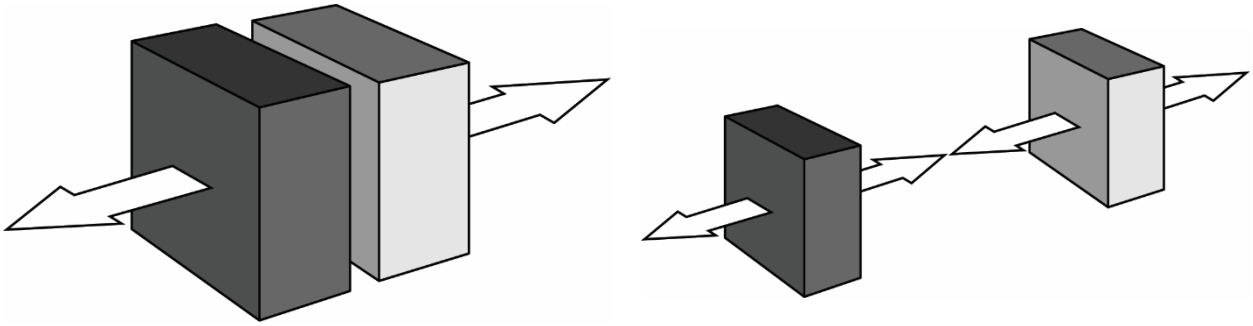

Figure 2-9: Schematic of heterogeneous element under deformation-sharing. In (a), the overall applied load is shown, and in (b) the overall load is still applied to each individual constituent.

These assumptions of load-sharing and deformation-sharing are critical to the understanding and development of the mechanics of materials equations.

2.2.3 Unidirectional composite

Figure 2-10 shows a theoretically perfect unidirectional lamina and conventional composites material axes. The direction nomenclature used is different than that discussed in Section 2.1.1. It is important to note that the fibers contained in a lamina are actually more randomly distributed since perfect alignment and distribution is nearly impossible to obtain unless very large fibers are used [1].

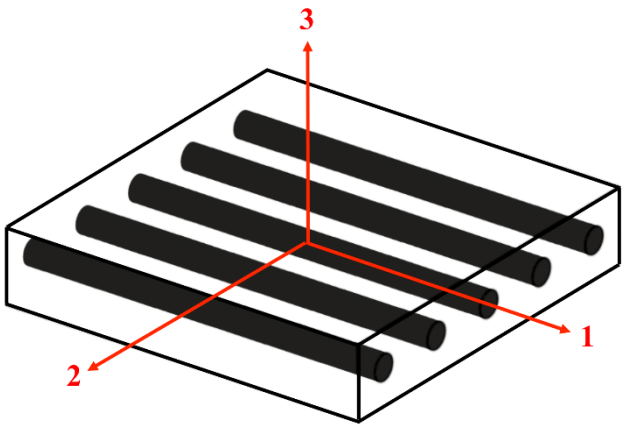

Figure 2-10: Representation of a unidirectional fiber reinforced composite lamina and material directions (1, 2, 3). Note that these directions are convention for composite laminates and are different than the conventions used for braided composites.

Consider previously the discussions of load- and deformation- sharing with regards to the unidirectional composite shown in Figure 2-10. If the composite is loaded in the 1-direction, parallel to the reinforcing fibers, it is a load-sharing/isostrain case mentioned previously. When loaded in either the 2- or 3- directions, it is a deformation-sharing/isostress case.

2.2.4 Lamina mechanics

This section is not intended to be an exhaustive discussion on the single ply (lamina) mechanics, but rather to refresh the reader on some of the core principles which are used in yarn twist and tubular braided composite stiffness modeling.

2.2.4.1 Volume fraction

The volume fractions of the fiber (V_f) and the matrix (V_m) are generically defined as:

$$V_i = \frac{v_i}{v_c}, \quad i = f, m \tag{2-1}$$

where v denotes constituent volumes (m^3) and $V_m = 1 - V_f$. Commonly, the fiber volume fraction will simply be referred to as the 'volume fraction'. Typical values for fiber volume fractions in continuous fiber textile composites range between 0.5 and 0.7 for most practical applications. At lower volume fractions, the fiber content is too low to have a significant impact on the performance of the material. Volume fractions above 0.9 are difficult to obtain as they are physically limited by the spacing and arrangement of fibers within the composite and by the manufacturing methods [4]. This equation assumes that there are no voids in the RVE. For the work presented here, a fiber volume fraction of $V_f = 0.6$ will be assumed.

2.2.4.2 Longitudinal elastic modulus

To predict the longitudinal elastic modulus of a unidirectional composite lamina, consider an RVE loaded in the fiber direction as shown in Figure 2-11. This is a case of load-sharing, as discussed previously.

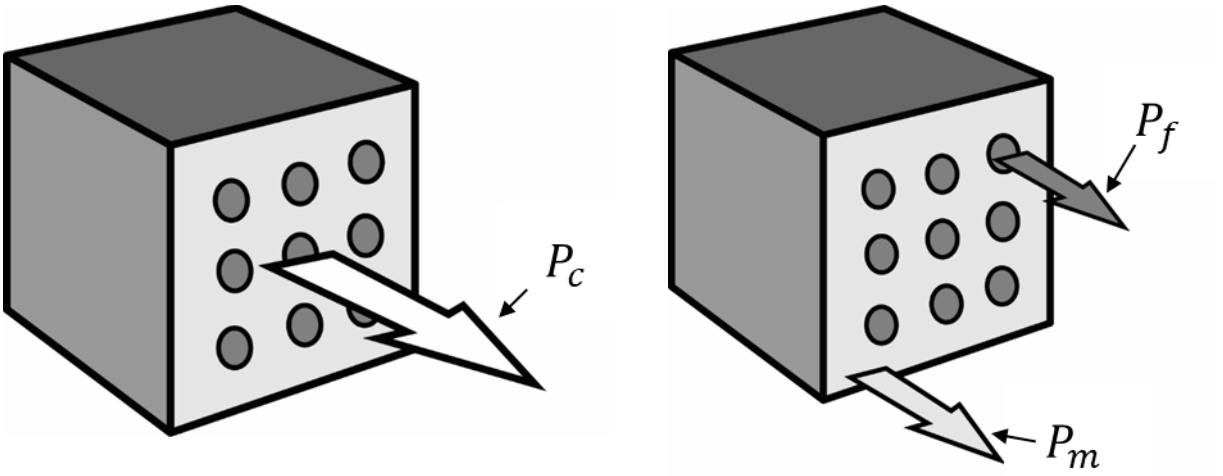

Figure 2-11: Unidirectional model for longitudinal properties: (a) overall load applied to composite P_c and (b) individual constituent contributions to loading P_f (fiber) and P_m (matrix)

In the isostrain case, it follows that the axial strains in both the fiber and matrix must be equal. The overall applied load can be distributed between the fiber and matrix constituents as shown in (2-2) where P_c, P_f, and P_m represent the load applied to the composite, the load taken by the fibers and the load taken by the matrix, respectively. These are related to the individual constituent strains by accounting for the area contribution of each, as shown in (2-3).

$$P_c = P_f + P_m \tag{2-2}$$

$$P_c = \sigma_f A_f + \sigma_m A_m$$

$$P_c = E_f \varepsilon_f A_f + E_m \varepsilon_m A_m \tag{2-3}$$

The relationship can be simplified further given that it has been assumed that all the constituents are under equal strain (that is, $\varepsilon_1 = \varepsilon_f = \varepsilon_m$), as shown in (2-4). As well, the normalized cross sectional area of each constituent is directly proportional to the respective volume fraction, given the fibers and fiber distribution have been assumed uniform, continuous, and parallel. The equation is then normalized with respect to the overall composite cross section, as seen in (2-5).

$$P_c = (E_f A_f + E_m A_m)\varepsilon_1 \quad \textbf{(2-4)}$$

$$E_{11} A_c \varepsilon_1 = (E_f A_f + E_m A_m)\varepsilon_1$$

$$E_{11} A_c = (E_f A_f + E_m A_m)$$

$$E_{11} = E_f \frac{A_f}{A_c} + E_m \frac{A_m}{A_c} \quad \textbf{(2-5)}$$

Assuming the cross-section is constant, the area fraction can be converted to a volume fraction and the final estimate of the longitudinal modulus in the direction of the fibers can be determined as seen in (2-6).

$$E_{11} = E_f V_f + E_m V_m \quad \textbf{(2-6)}$$

2.2.4.3 Transverse elastic modulus

Many models have been developed for the transverse modulus of unidirectional composites, E_{22}. Fibres act as deformation restrictions that result in a higher transverse tensile modulus than the matrix modulus. Figure 2-12 illustrates the transverse model of a unidirectional composite from which the equations in the mechanics of materials approach can be derived.

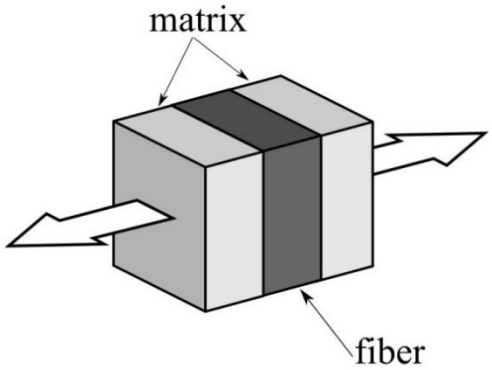

Figure 2-12: Unidirectional model for transverse properties

Again, from our initial assumptions, it is assumed that the fibers have uniform properties and diameter, are continuous and parallel throughout the composite, and are bonded perfectly to the matrix. However, in this case, rather than the individual constituents sharing the applied load,

this arrangement leads to the deformation being shared instead; that is, the total strain experienced by the composite material element is a summation of the strains of each of the individual constituents. The load applied to each constituent is assumed to be the same as the overall applied load.

Assuming an initial length of L_2 for the overall composite in the transverse direction and L_f and L_m for the fiber and matrix components respectively, the strain behavior between constituents can be related as in (2-7).

$$\Delta L_2 = \varepsilon_2 L_2 = \varepsilon_f L_f + \varepsilon_m L_m \tag{2-7}$$

Again, the assumption is made that the volume fractions V_f and V_m are still representative in the RVE and the respective lengths are proportional to these fractions as well. Equation (2-8) is updated to reflect the strain relationship with respect to the volume fraction.

$$\begin{aligned} \varepsilon_2 L_2 &= \varepsilon_f V_f L_2 + \varepsilon_m V_m L_2 \\ \varepsilon_2 &= \varepsilon_f V_f + \varepsilon_m V_m \end{aligned} \tag{2-8}$$

The stress is assumed equal for each constituent and can be modeled as a set of springs in series.

$$\frac{\sigma_2}{E_2} = \frac{\sigma_2}{E_f} V_f + \frac{\sigma_2}{E_m} V_m$$

Equation (2-9) shows the preferred final form of the transverse modulus as determined by the mechanics of materials approach.

$$\frac{1}{E_2} = \frac{V_f}{E_f} + \frac{V_m}{E_m} \tag{2-9}$$

2.2.4.4 Compliance of a unidirectional lamina

The unidirectional lamina is one of the 'building blocks' within the multiscale framework of mechanical modeling in composite materials. Here, it is assumed that a representative volume element of the material can be distilled down to a single planar structure that is transversely isotropic. That is, though there is fiber reinforcement in the longitudinal direction, for all

directions orthogonal to the longitudinal the composite is effectively isotropic. Further still, if out-of-plane loading is ignored, then a plane stress assumption can be made as well. The compliance of a material is defined as the strain response to an applied load as shown in (2-10).

$$\varepsilon_i = S_{ij}\sigma_j \text{ for } i,j = 1,2 \ldots 6 \quad \textbf{(2-10)}$$

Equation (2-11) is the reduced compliance matrix for a generally orthotropic lamina under the plane stress assumption.

$$[S] = \begin{bmatrix} S_{11} & S_{12} & 0 \\ S_{12} & S_{22} & 0 \\ 0 & 0 & S_{66} \end{bmatrix} \quad \textbf{(2-11)}$$

Each of the elements in (2-11) are defined as shown in equations (2-12) through (2-15).

$$S_{11} = \frac{1}{E_1} \quad \textbf{(2-12)}$$

$$S_{22} = \frac{1}{E_2} \quad \textbf{(2-13)}$$

$$S_{66} = \frac{1}{G_{12}} \quad \textbf{(2-14)}$$

$$S_{12} = -\frac{\nu_{12}}{E_1} = -\frac{\nu_{21}}{E_2} \quad \textbf{(2-15)}$$

2.2.4.5 Compliance in global coordinates

The reduced compliance matrix (2-11) only accounts for stresses and strains in the coordinate system of the unidirectional lamina, either in the direction of the reinforcing fibers or perpendicular to them. When the unidirectional lamina is no longer loaded in the longitudinal direction but rather off-axis to the fiber reinforcement, the lamina is then considered to be generally orthotropic. For a generally orthotropic lamina under plane stress in global coordinates, the updated global compliance matrix $[\bar{S}]$is defined as in (2-16).

$$[\bar{S}] = \begin{bmatrix} \bar{S}_{11} & \bar{S}_{12} & \bar{S}_{16} \\ \bar{S}_{12} & \bar{S}_{22} & \bar{S}_{26} \\ \bar{S}_{16} & \bar{S}_{26} & \bar{S}_{66} \end{bmatrix} = [R][T]^{-1}[R]^{-1}[S][T] \quad \textbf{(2-16)}$$

Each of the elements of $[\bar{S}]$ are a function of the elements of the reduced compliance matrix (2-11) and are defined in equations (2-17) through (2-22).

$$\bar{S}_{11} = S_{11}\cos^4\theta + (2S_{12} + S_{66})\sin^2\theta\cos^2\theta + S_{22}\sin^4\theta \quad \textbf{(2-17)}$$

$$\bar{S}_{12} = (S_{11} + S_{22} - S_{66})\sin^2\theta\cos^2\theta + S_{12}(\sin^4\theta + \cos^4\theta) \quad \textbf{(2-18)}$$

$$\bar{S}_{22} = S_{11}\sin^4\theta + (2S_{12} + S_{66})\sin^2\theta\cos^2\theta + S_{22}\cos^4\theta \quad \textbf{(2-19)}$$

$$\bar{S}_{16} = (2S_{11} - 2S_{12} - S_{66})\sin\theta\cos^3\theta + (2S_{12} - 2S_{22} + S_{66})\sin^3\theta\cos\theta \quad \textbf{(2-20)}$$

$$\bar{S}_{26} = (2S_{11} - 2S_{12} - S_{66})\sin^3\theta\cos\theta + (2S_{12} - 2S_{22} + S_{66})\sin\theta\cos^3\theta \quad \textbf{(2-21)}$$

$$\bar{S}_{66} = 2(2S_{11} + 2S_{22} - 4S_{12} - S_{66})\sin^2\theta\cos^2\theta + S_{66}(\sin^4\theta + \cos^4\theta) \quad \textbf{(2-22)}$$

The transformation matrix $[T]$ for an angle θ is defined as in (2-23).

$$[T] = \begin{bmatrix} \cos^2\theta & \sin^2\theta & 2\sin\theta\cos\theta \\ \sin^2\theta & \cos^2\theta & -2\sin\theta\cos\theta \\ -\sin\theta\cos\theta & \sin\theta\cos\theta & \cos^2\theta - \sin^2\theta \end{bmatrix} \quad \textbf{(2-23)}$$

The Reuter's matrix $[R]$ is defined as in (2-24).

$$[R] = \begin{bmatrix} 1 & 0 & 0 \\ 0 & 1 & 0 \\ 0 & 0 & 2 \end{bmatrix} \quad \textbf{(2-24)}$$

2.3 Textiles definitions

In this section, definitions and concepts specific to textile yarns research will be discussed as they apply to this work.

2.3.1 Textile yarns

A yarn refers to a continuous collection of filaments or fibers that can be handled as a single unit in textile applications [23]. Their composition may be of many staple yarns (e.g. spun cotton or wool) or of multiple continuous filaments (e.g. Kevlar, Glass, Carbon, Biomid), or even a single monofilament. This work will focus on continuous multifilament yarns and will not discuss the impact of twist on other types of yarns.

2.3.2 Linear density

Yarns are classified primarily by their material composition and by their linear density. Denier and tex (or dtex) are measures of the linear density commonly used in textiles applications. Denier is the mass in grams of 9000 meters of yarn, tex is the mass in grams of 1000 meters of yarn, and dtex is the mass in grams of 10000 meters of yarn. Use of this system accounts for some variation in production (such as exact filament count and size) and allows for direct

measurement measuring the weight and length of a section of yarn. Conversion is trivial between denier and dtex and they are often used interchangeably within both metric and imperial systems.

2.3.3 Modulus and strength

In order to calculate the applied stress on a material, an accurate measurement of the normal area is required. As will be discussed in section 2.3.6 this is not always trivial. A common textile unit is grams-force per denier (g/d), which accounts for the yarn size by means of normalizing with respect to the linear density of the yarn. Both yarn modulus and strength are reported for textile yarns in units of grams-force per denier.

2.3.4 Yarn shape

The cross-section of a textile yarn has been investigated and modeled in different ways. For a multifilament yarn, the cross-section is often flat and ribbon-like, until it is twisted and will take on another shape [31]. When the yarn is used in a textile structure, the cross section can also take a variety of shapes [32]–[34]. Some assumptions have included circles [35], ellipses [36], lenticular shapes [37], and a so-called racetrack model [38] in an attempt to characterize this form. In this work, we will assume a circular profile, for the simplicity in calculating twist.

2.3.5 Twisted yarns

Yarn twist is often introduced in the manufacturing process yarns manufactured from short fibers, such as wool or cotton to continuous filament yarns. The spinning process allows each of the individual filaments to be consolidated into a single entity (the yarn). For short fiber yarns, there is a minimum amount of twist that must be included to provide sufficient handling strength. Increased twist increases interfilament friction, and subsequently, yarn strength. However, the increased twist also increases fiber obliquity, which decreases overall strength. Thus, there often exists a level of optimal twist where the effects from both of these contributions overlap [39]. Twist can also be applied to continuous filament yarns, which can improve ease of handling [3]. Longitudinal yarn stiffness is negatively affected by yarn twist due to misalignment of the fibers relative to the longitudinal direction, just as in a composite laminate any variation from the longitudinal direction results in a loss of stiffness.

2.3.5.1 Definition

"Twist" refers to the rotation of the yarn about its longitudinal axis. Twist can be applied in one of two ways, referred to either as false or true twist. To apply false twist to a yarn, both ends of the yarn are held fixed while the yarn is rotated about its longitudinal axis. In this case, if the twisting force is released/removed and sufficient tension exists in the yarn, the yarn will self-align again to an untwisted state without moving either end of the yarn. True twist is when one end of the yarn is twisted with respect to the other end. In this case, unless one of the fixed ends is released, the twist will remain in the yarn sample, regardless of the tension applied. Herein, any reference to twist refers to true twist.

2.3.5.2 Twist measurement

The twist can be evaluated by the count of turns per unit length of measure, such as twists per meter (TPM) or twists per inch (TPI). These are direct measures of twist, which do not account for the size of the yarn under twist. This is problematic as the larger diameter yarns will yield higher filament obliquity than smaller ones due to the increased diameter of the helical path the filaments must take.

Other derived measures (such as the twist factor and twist multiplier) can be used to account for the size of the yarn twisted. This is often a better approach for comparing the behaviour of different yarns as it accounts for the variation in size. The reader is referred to ASTM D1423 for conversions between these systems [40].

A third method of measuring twist is by the twist angle. Rather than depending on one of the measures of twist mentioned above, twist can be measured as the angle between the filament direction and the primary axis of the yarn. One downside to this approach is the variation of angle for each filament throughout the yarn, as theoretically the angle of twist will increase the farther the filament is from the central axis. Surface twist accounts for the size of the yarn and the number of turns, but does not account for the distribution of angles throughout the structure. Assuming a constant circular cross-section for the yarns, the surface twist can be found according to (2-25), where, h is the length of yarn required for one complete helical path of an outer filament and R is the radius of the yarn.

$$\tan \alpha = \frac{2\pi R}{h} \tag{2-25}$$

The length of yarn for one complete helical path of the filament is simply the inversion of the direct count measurement as shown in (2-26).

$$h = \frac{1}{TPM} = \frac{1}{TPI} \tag{2-26}$$

Equation (2-27) gives the conversion between direct measurement and surface twist.

$$\tan \alpha = 2\pi R \times TPM \tag{2-27}$$

What remains is to calculate an appropriate radius R for the helical path. While this can be directly measured, it is not a trivial matter given the relatively small size of textile yarns. It can, however, be derived from the area assumptions regarding the structure of the composite yarn, as discussed in Section 2.3.6.

2.3.6 Yarn area estimations

Area measurement of the textile yarn is required to determine yarn stress as well as the twist angle, as mentioned in section 2.3.5.2. Direct measurement would be a simple solution, however with small samples and specimens with no fixed cross section, this area can be difficult to measure. Here we will discuss two ways in which this area can be estimated.

2.3.6.1 Filament area estimate

One of the ways to estimate the effective cross sectional area in a sample is to assume a standardized cross sectional area of the yarn based on filament count and filament size. Manufacturers sometimes provide the filament count (n_f) and the filament diameter (d_f), and the area can then be estimated as shown in (2-28).

$$A_y = n_f \times \left(\frac{\pi d_f^2}{4}\right) \tag{2-28}$$

One of the issues with this estimate is that it assumes the diameter and the filament count are constant and well known within the sample. Additionally, filament packing can vary throughout a sample, and the actual yarn area can differ greatly from what is calculated in this approach [41].

2.3.6.2 Density estimate

Another way to calculate the effective area is using the linear density and density of the textile yarns. Assuming both are constant throughout the entirety of the yarn, the area of the yarn can be

determined through a volume calculation of the yarn. If the linear density and density of the sample is known, then the area can be calculated as shown in (2-29).

$$A_y = \frac{den}{\rho} \tag{2-29}$$

This approach is suggested by ASTM D2343 for estimating the fiber contributions to a composite strand [42].

2.3.6.3 Comparison to manufacturer values

A third means of determining the cross-sectional area is to infer the area used by the manufacturer. This can be done by comparing the area-derived and area-independent values provided by the manufacturer, for example by comparing the yarn strength in units of stress in comparison with the breaking load in units of force.

Below in Table 2-1 is a comparison of the area estimation methods across the values for three different textile yarns. Detailed calculations of these values are provided in Appendix B.

Table 2-1: Summary of manufacturer values and area estimates

Yarn	**Kevlar 29**	**Kevlar 49**	**BioMid**
Denier (den)	1500	1140	1650
Filament count	1000	768	900
Filament diameter (micron)	12	12	11
Modulus (g/d)	555	885	315
Reported modulus (GPa)	70.5	112.4	42
Density (g/cm^3)	1.44	1.44	1.53
Filament area estimate (mm^2)	0.1131	0.08686	0.0855
Density estimate (mm^2)	0.1157	0.08796	0.11619
Estimate from manufacturer values (mm^2)	0.1158	0.08803	0.11768

It should be noted that there exists a distribution of filament diameter, filament count, and linear density in the manufacture of textile yarns, as demonstrated by Wagner et al with aramid yarns [43]. Thus, even the most accurate of estimates will still be an estimate and subject to the inherent variability present in manufacturing.

2.3.7 Yarn stiffness

2.3.7.1 Geguaff's helical filament model

The earliest stiffness modeling of a twisted yarn is presented by Gegauff [44]. Gegauff's model is a simple application of helical geometry to the concept of strain [45]. This model accounts for the off-axis orientation of each fiber as well as the variation in twist angle with respect to radial position within the yarn, as shown in Figure 2-13.

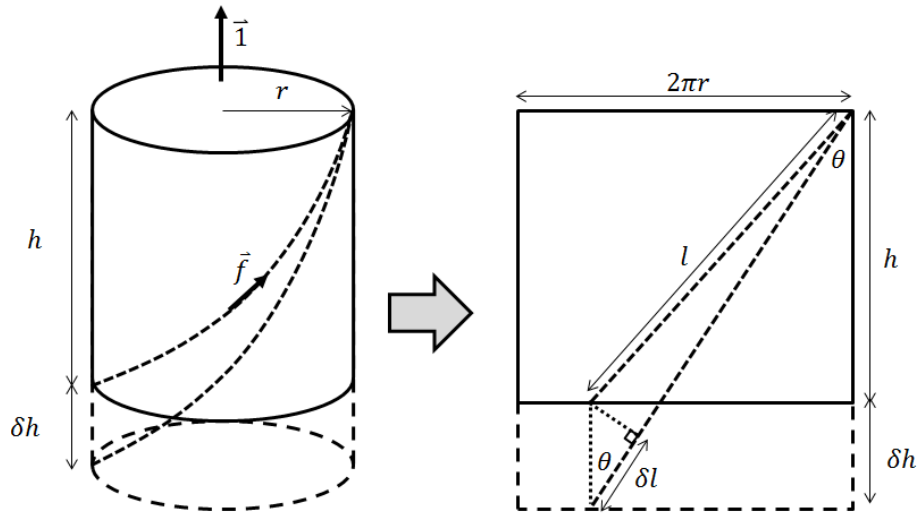

Figure 2-13: Schematic showing Gegauff's classical yarn model for yarn mechanics [44] **showing the unwrapping of a cylindrical yarn element into a single filament layer**

On the left in Figure 2-13 is a representation of the overall yarn shape assuming a circular cross section, while the path of a single yarn filament is shown to follow a helical path at a radius r with angle θ to the longitudinal direction. If a longitudinal load P is applied to the yarn, the yarn with height h will extend with length δh, or in terms of engineering strain, $\varepsilon_1 = \frac{\delta h}{h}$, while subject to a normal stress of σ_1 on the cross section. The Young's modulus can be calculated as a ratio of the stress and strain as shown in (2-30).

$$E_1 = \frac{\sigma_1}{\varepsilon_1} = \sigma_1 \cdot \frac{h}{\delta h} \tag{2-30}$$

Considering the unwrapped helical geometry, the height h can be related to the filament length l by the off-axis angle θ (here θ will be used in the derivation as α is reserved specifically for the surface twist angle) as in (2-31).

$$h = l \cos\theta \tag{2-31}$$

Additionally, the angle of twist θ is related to the radial position of the yarn r through simple geometry as in (2-32). Similarly, for the outermost yarn, the limiting case is true regarding the surface twist angle α.

$$\tan\theta = \frac{2\pi r}{h}; \quad \tan\alpha = \frac{2\pi R}{h} \tag{2-32}$$

Small deformations must be assumed such that the surface twist angle α does not change with application of load. Thus the relationship between the nominal longitudinal extension δh and the actual filament extension δl can be written as in (2-33).

$$\delta l = \delta h \cos\theta \tag{2-33}$$

The filament strain $\varepsilon_f = \frac{\delta l}{l}$ can be related to the longitudinal extension of the yarn as in (2-34).

$$\frac{\delta h}{h} = \frac{\delta l}{\cos\theta} \cdot \frac{1}{l \cdot \cos\theta} = \frac{\delta l}{l} \cdot \frac{1}{\cos^2\theta}$$

$$\varepsilon_1 = \frac{\varepsilon_f}{\cos^2\theta} \tag{2-34}$$

Note that this same $\cos^2\theta$ term appears in the transformation matrix for a generally orthotropic lamina, as shown in (2-23).

Equation (2-34) relates the filament and yarn strains for a twisted yarn, but in order to relate the stiffnesses the area contribution of each layer must be considered. First, consider the normal stress acting on a single yarn filament as in (2-35).

$$\sigma_f = E_f \varepsilon_f \tag{2-35}$$

The longitudinal component of stress, σ_1, acting on the same filament, as shown in (2-36).

$$\sigma_1(\theta) = \sigma_f \cos\theta \tag{2-36}$$

An integral approach must be taken since the twist angle, and thus the filament angle, is a function of the radial position of the filaments. The differential area element dA is made up of filaments at an angle θ as shown in (2-37).

$$dA = 2\pi r dr \cos\theta \tag{2-37}$$

The portion of the longitudinal load acting on a single differential ring dP is (2-38).

$$dP = \sigma_1 dA$$

$$dP = \sigma_f \cos\theta \, (2\pi r dr \cos\theta) \tag{2-38}$$

The integration is then carried out from the center of the yarn to the outer radius R, substituting in equations (2-34) and (2-35) where appropriate. As well, since $\theta = \theta(r)$ and $\alpha = \theta(R)$ at the outer surface of the yarn, then the normal load acting on the yarn P is given in (2-39).

$$P = \int_0^R \sigma_f \cos\theta \, (2\pi r dr \cos\theta)$$

$$= \int_0^R E_f \varepsilon_f 2\pi r dr \cos^2\theta$$

$$= \int_0^R E_f 2\pi r \, \varepsilon_1 \cos^4\theta \, dr \quad \textbf{(2-39)}$$

$$= \pi R^2 \varepsilon_1 E_f \cos^2\alpha \quad \textbf{(2-40)}$$

Knowing that $\frac{P}{\pi R^2} = \sigma_1$ and $\frac{\sigma_1}{\varepsilon_1} = E_1$, the relationship for a twisted yarn is shown in (2-41) to be a function of the stiffness of the filament E_f and the surface twist angle α.

$$E_1 = E_f \cos^2\alpha \quad \textbf{(2-41)}$$

2.3.7.2 Comparison to micromechanical model

Equation (2-17) shown in section 2.2.4.5 defines the $\overline{S_{11}}$ term in global coordinates for a generally orthotropic lamina. For a yarn under tensile load, this is the term of particular interest as it relates the strain response to an applied load. In the case of a textile yarn without a composite matrix, the transverse terms approach zero and the updated compliance is as shown in (2-42).

$$\bar{S}_{11} = S_{11}\cos^4\theta + \cancel{(2S_{12} + S_{66})\sin^2\theta\cos^2\theta} + \cancel{S_{22}\sin^4\theta}$$

$$\bar{S}_{11} = S_{11}\cos^4\theta \quad \textbf{(2-42)}$$

This is the same $\cos^4\theta$ term also observed in (2-39), and the subsequent integration in the radial direction in (2-40) results in the relationship shown in (2-41).

2.3.7.3 Other twist models

Gegauff's model is the starting point for many of the other theoretical twist models. Perhaps the most important concept communicated in this model is that the deviation of modulus is due primarily to the declining orientation of fibers in the longitudinal loaded direction. However,

there are some corrections that have been made over the years to try and narrow down the disagreement between model and experiment.

Hearle et al. [46] include the perpendicular interfilament forces acting within the yarn structure as shown in (2-43).

$$\frac{E_1}{E_f} = \frac{1}{(1+\nu)} \frac{\cos^2 \alpha}{(1-\cos^2 \alpha)} \left[\frac{4+3\nu}{2(1+\nu)} - \frac{1+\nu}{2\nu} \cos^2 \alpha - \frac{2\nu^2+2\nu-1}{2\nu(1+\nu)} \cos^{2(1+\nu)} \alpha + \log_e \cos \alpha \right] \tag{2-43}$$

Note that ν is the Poisson's ratio of the fibers. As can be seen, a small assumption can result in a drastic change in model complexity.

Rao and Farris consider the rotation of the stiffness matrix created by the misalignment and orientation of the filament direction due to radial displacement and twist. Equation (2-44) below results from considering the rotation of the stiffness matrix as well as the radial displacement of the filament within the yarn structure.

$$E_1 = E_f \times \left[\frac{3T_0 + 1}{2\, d\, T_0} + \frac{(1-d)^2}{d^3 \tan^2 \theta} \cdot \ln \left(\frac{(1-d)T_0 + d}{T_0} \right) \right] \tag{2-44}$$

where $T_0 = \cos^2 \theta$ and $d = \frac{E_z}{E_s}$ (the anisotropic ratio, the ratio between the longitudinal (E_z) and shear (E_s) moduli of the fiber but determined through curve fitting).

Naik and Madhavan also consider the effects of deviation from idealized helical geometry, including both migration and microbuckling effects [47]. Migration is considered in the outermost radial positions of the filaments within the yarn. Since the filament path is much greater than that of the average yarn, it is proposed that some of these outer filaments will migrate inward towards the core of the yarn. Microbuckling is considered within the core region, where these filaments with the shortest path will buckle to compensate for the additional length of these filaments. Naik and Madhavan consider cases up to 1.5% migration and 0.6% microbuckling based on the predicted size of the respective migration and microbuckling zones. In practice these would have to be determined through direct measurements.

Table 2-2: Summary of Twisted Yarn Models

Author	Model details	Variables
Gegauff [48]	$\cos^2\theta$ geometry	E_f (longitudinal filament modulus) and θ (surface twist angle)
White [49]	$\cos^2\theta$ with interfilament friction	
Rao and Farris [44]	$\cos^2\theta$ with stiffness rotation	E_f, θ, and d (anisotropic ratio)
Naik and Madhavan [47]	$\cos^2\theta$ with stiffness rotation, migration and microbuckling effects	

Baets et al. [50] also compare these models, as well as an additional elliptical cross-section adjustment to the Naik model. For yarns with low twist (<10º) the difference between the Gegauff and White models and between the Rao and Naik models, respectively, is negligible.

2.3.8 Yarn strength

Strength modeling of twisted yarns presents a different challenge than stiffness modeling, as the mechanism of failure must also be determined, which is not trivial given the heterogeneous structure of a composite material. Generally, the addition of twist to a strand of yarn will improve the yarn strength up to a singular optimal point, where it will begin to decrease again. This has been attributed to an increase in interfilament friction; that is, as the twist increases, the outer filaments 'squeeze' the remaining filaments together, helping the yarn to behave as a single unit rather than individual filaments. However, at some point, the obliquity of the fibers takes over, and the advantage from the squeezing effect cannot overcome the loss of strength from the fibers being at an angle to the loading direction. The reader is directed to work by Shah [51], Subramanian [52], and Naik and Mudzingwa [53] for further research on the subject.

2.3.9 Sample yarn properties

Throughout this work, two different Kevlar 49 yarns and BioMid fiber yarn will be referenced. A summary of properties of the yarns used is provided in Appendix A. BioMid is a regenerated cellulose fiber which differs from other naturally sourced fibers in that it is composed of continuous filaments similar in structure to Kevlar [54]. Other natural fiber yarns require twist for structure [55] or must be commingled with other continuous yarns for use [56].

2.4 Stiffness modeling of TBCs

Modeling of tubular braided composites, and textile composites in general, typically relies on the assumption that the primary determinant of stiffness and strength within the structure is based on the alignment of the reinforcing fibers with respect to the direction of the application of load [6]. In unidirectional composites this is a trivial task, but with increasingly complex composite structures the textile structure must be well understood for models to be accurate and to reflect the true nature of the composite. The properties of the reinforcing matrix cannot be overlooked either, as they play a critical role in how the composite behaves as a cohesive unit. For this work the modeling of other braided structures, such as ropes and core-filled braids [57], will not be discussed as these are beyond the scope of this research.

2.4.1 Review of existing models

One of the fundamental models is the classical laminated plate theory, and many of the stiffness models are some variation based on this approach [58], [59]. The repeating unit cell is assumed to consist of three distinct types of regions, as shown in Figure 2-14.

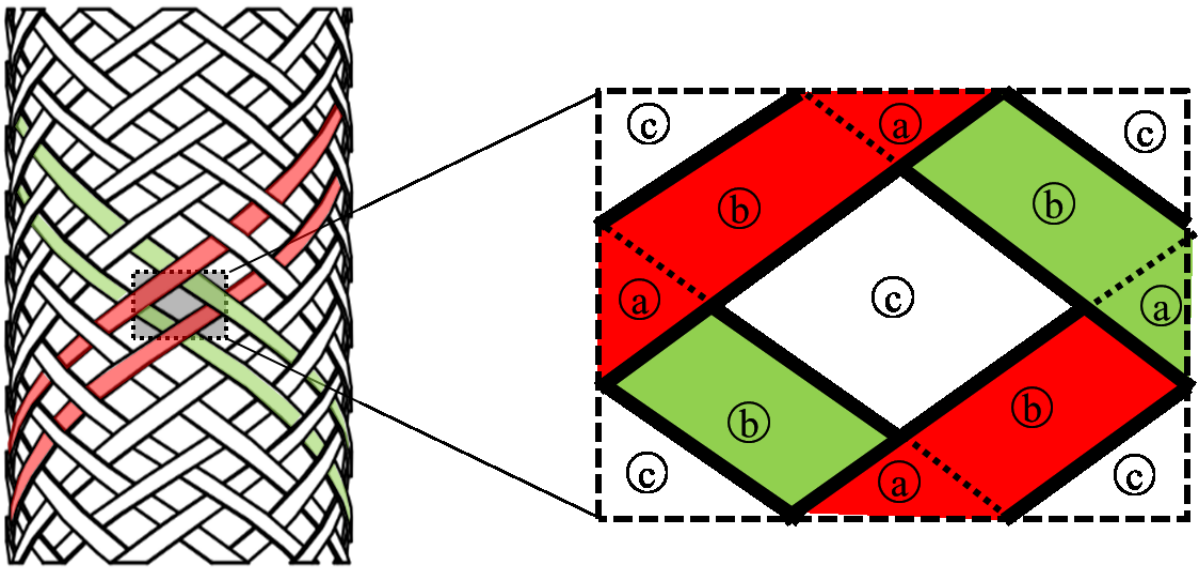

Figure 2-14: Schematic of braid along with close-up of repeating unit cell used in modeling, where (a) are the overlapping yarn regions, (b) are the undulating yarn regions, and (c) are the resin-rich regions.

First, there are regions where the braiding yarns are perfectly overlapping and are also orthogonal to the out-of-plane direction. Next, there are undulating regions, where the yarns pass from one overlapping section to another and move from an "over" position to an "under" position, breaking the plane and reinforcing the braid in the through-thickness direction. Finally, the third region contains no reinforcing fibers, known as the resin-rich or matrix-only region. This region contributes very little to the structure of the braid and could potentially be a site for failure initiation. This type of approach is not unique to braiding and is a common approach to modeling in the field of composite materials. However, certain considerations must be made when it comes to TBCs given their unique geometry.

Carey proposed that TBCs can be modeled with a modified Classical Laminated Plate Theory (CLPT) model assuming the TBC is composed of thin laminae subject only to in-plane loading. Ayranci and Carey then proposed that the size of the unit cell relative to the size of the braid tube is such that curvature should not be neglected [60].

Another approach that has been used is to take the global geometric structure of the braid and use sine geometry to predict the undulation path and behaviour of the yarns with respect to the braid [11], [15]. Two transformations of the stiffness matrix are required to determine the inclination of the yarn with respect to the longitudinal direction of the braid. The first transformation transposes the local yarn direction to that of the undulation direction, the second transformation then takes these stiffnesses into the global direction. Alpyildiz [15] discusses the theoretical

mathematical model of the individual yarn paths, considering the helical (due to the structure of the TBC) and undulating (due to the interaction of yarns) behaviours of the braiding yarns. Melenka [11] expands on these by integrating this geometry, lenticular yarn cross-section shape assumptions, and the volume averaging contributions of each distinct region of the TBC in order to form this model. As well, some work has gone into the development of simulating braids in order to develop a model for FEA use [61].

2.4.2 Modulus terminology

Similar to the discussion regarding directional nomenclature, consistency is required in the terminology used to describe the stiffness of constituents. Young's modulus, elastic modulus, and longitudinal modulus will be used interchangeably but typically referenced with context. For example, the yarn elastic modulus refers to the modulus aligned with the yarn direction, while the braid elastic modulus refers to the modulus aligned with the primary braid direction.

2.4.3 Stress-strain behaviour of TBCs

The stress-strain behaviour of TBCs can be broken down into three distinct sections, as shown in Figure 2-15.

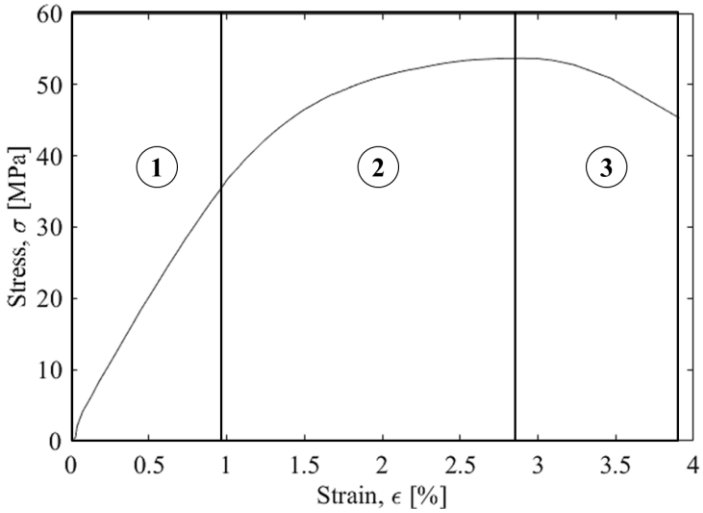

Figure 2-15: Plot of a representative stress-strain of longitudinal tensile behaviour of a TBC. Phase 1 is the elastic response, phase 2 is the plastic deformation up to the ultimate strength, and phase 3 is the yarn scissoring as the braid approaches the jamming point.

At the onset of tension, there is a region of linear extension within the linear elastic range of the material. Behaviour of TBC's in this region has been well documented [11], [58], [59]. Next, there is a plastic deformation phase, where the response is no longer linear. This region has previously been ignored for TBCs as the unidirectional composites of the same constituents do

not express this behaviour. Following there is a necking phase, where the progressive degradation of the composite matrix allows for overlapping yarns to shear relative to each other in a scissoring fashion [62]. The effect resembles that of a necking metal sample, as the diameter of the TBC decreases during this phase. The yield point occurs right before this point and represents the transition between plastic deformation and necking. Stress can vary in this region, due to the complex nature of this phase. In this study, for example, the stress most often decreased with the constant extension rate. This step often involves very large deformations and is often not practical to test with typical tensile frame setups or traditional strain measurement systems. Finally the TBC will approach 'jamming' point, a point where the yarns can no longer physically move relative to one another [23],[33]. Here, the stress may rapidly increase again as this limit is met and the TBC soon fails.

2.4.4 Plastic zone modeling

The majority of efforts have focused only on modeling the linear elastic portion of the stress-strain curve for composites. Bogetti et al. use the Ramberg-Osgood equation to model the nonlinear behaviour of a composite laminate [63], but this is restricted to the interlaminar shear direction and not applied to the longitudinal or in-plane shear. Cao et al. analyze the in-plane behaviour of a carbon-Dyneema® hybrid woven composite and use the Ramberg-Osgood equation to define the nonlinear behaviour of the Dyneema textile [64]. For these reasons and through observation of its yield behaviour the Ramberg-Osgood equation is a good candidate for application to TBCs. Beard and Chang attribute the nonlinear behaviour to the scissoring that occurs during the compressive longitudinal crushing of TBCs by continually updating the stiffness model as the braiding yarns rotate relative to each other [28]. However, if that same logic is applied to this study, that would imply the stiffness of TBCs increases during failure, which is contrary to the behaviour that has been observed.

2.4.4.1 Ramberg-Osgood equation

The Ramberg-Osgood equation is an analytical power law equation that can be used to describe the plastic deformation of the stress-strain curve of a material [65]. Technically, the Ramberg-Osgood equation can take multiple forms so long as both the elastic modulus and an exponent are involved, but in this work the form of the equation that uses the yield strength and offset will be used:

$$\varepsilon = \frac{\sigma}{E_0} + \alpha \left(\frac{\sigma}{\sigma_y}\right)^n \quad \textbf{(2-45)}$$

Where σ and ε are the stress and strain responses of the material, E_0 is the initial linear elastic modulus, α is the strain at the measured offset point and σ_y is the yield stress of the material as determined by the offset yield. The parameter n is the fit parameter that governs the stress-strain curve behaviour beyond the linear elastic region.

2.4.5 Twisted yarns in TBCs

Previous studies have neglected the presence and effects of twisted yarns within TBCs [58], and there is little documentation on the use of twisted yarns in other textile composites. Ma et al. investigated the effect of twisted sisal fiber yarns in unidirectional composite laminates [66]. Xu and Qian have developed a model to predict the stiffnesses of a four-directional braided composite (4DBC) by including the effects of yarn distortion, including yarn twist, but does not account for change in strength and is only compared to three experimental samples [21]. Other studies have researched the effect of twist in woven composite structures [66]–[69], while many studies on yarn twist in textile structure focus on non-composite applications, such as ropes [70], yarns [71]–[73], or woven fabrics [1], [74]. No studies on the impact of twist in TBCs has been documented thus far.

2.5 Visualization of textile composite structure

Both traditional microscopy and computed tomography have been used for the purposes of exploring textile structure, yarn architecture, and composite microstructure. Optical microscopy is a valid yet time-consuming approach with polymer composites [75]

X-ray computed tomography (CT) allows for nondestructive evaluation of the internal structure of materials [76]. With polymer composites the issue of contrast between constituents must be addressed [77], [78], but it has still shown to be a viable method in characterizing textile and textile composite structures for the purposes of computer rendering, reconstruction, finite element analysis, and failure analysis [79]–[85]. These methods have sufficient resolution to resolve individual filaments within the composite structure [86].

Chapter 3 Experimental methods

In this chapter, the procedures and methods used throughout the body of this work in detail will be discussed. As some of the subsequent chapters have been submitted or accepted for publication, some overlap may occur in terms of content provided. Included are an overview of the materials used, followed by a detailed procedure of specimen fabrication, material testing, and data analysis.

3.1 Definitions

Before going into detail regarding the various specimens manufactured throughout this work we will attempt to clarify the terminology used as some terms have been used interchangeably throughout the literature. Some additional adjectives (such as “dry”) have been used that are not traditionally necessary, but add clarity in the context of this work

- dry yarn: a multifilament textile yarn with no supporting matrix
- composite strand: a cured composite consisting of a single multifilament yarn and a supporting matrix
- braid or braided preform: a textile structure manufactured from textile yarns with no supporting matrix
- TBC (tubular braided composite): a cured composite made from the impregnation of a braided preform with a supporting matrix

3.2 Materials

The materials used in this work fall into two categories, textile yarns and polymer resins. The combination of Kevlar 49® and Epon 826 / Lindau LS-81K as a composite system has been used extensively by our research group in the past and the systems and processes in place have largely been based on the use of these materials [11], [29], [87], [88]. Recent efforts within the group and within the scientific community as a whole have focused on the use of naturally derived textile yarns and epoxies in composite materials [39], [54], [89]. Thus, the use of BioMid™ and EcoPoxy® as a greener alternative to the Kevlar 49® and Epon 826 / Lindau LS-81K system was trialed throughout, as this system has yet to be well characterized.

3.2.1 Textile yarns

3.2.1.1 Overview

Two different yarn materials were used for testing, Kevlar 49® and BioMid™. Both materials have been previously used in the manufacture of TBCs [54], [90].

Kevlar 49 ® is a multifilament aramid fiber yarn produced by DuPont™ [91]. It is a high strength, high modulus fiber than is bundled into multifilament yarns for the purposes of textile applications. A well established body of literature exists for the use of Kevlar 49® as a dry yarn and as a composite reinforcement [25], [44], [72], [92], as well as the use of other polyaramids such as Kevlar 29® [3], [93].

BioMid™ is a multifilament regenerated cellulose yarn produced by the BioMid Fiber company as a joint development of Gordon Shank Consulting and ENC Korea. Unlike other cellulose derived fibers, it does not use the viscose process, but claims to be produced on a "zero-waste, closed-loop production line", with the only inputs as water, cellulose and electricity [94]. Details on the manufacturing process are currently unavailable and likely protected at this time as a trade secret. Limited previous work has been documented with this material [54], [95].

3.2.1.2 Yarn selection

Yarn deniers were selected based on availability as well as range of test equipment. Currently, only 1650 denier BioMid™ yarns are available. Thus, the denier of Kevlar 49® was selected such that the testing procedure between yarns was consistent.

For the dry textile yarns and the composite strands, 380 denier Kevlar 49® was used as the maximum capacity of the tensile frame was 500 N, and this placed the ultimate failure load of the two yarns within the same order of magnitude.

During the braiding process it was important that the cover factor of the braid be similar between samples. Based on the braiding geometry, the use of 380 denier Kevlar 49® would have resulted an open mesh braid with large gap and resulting resin rich regions [96], as shown in Figure 3-1.

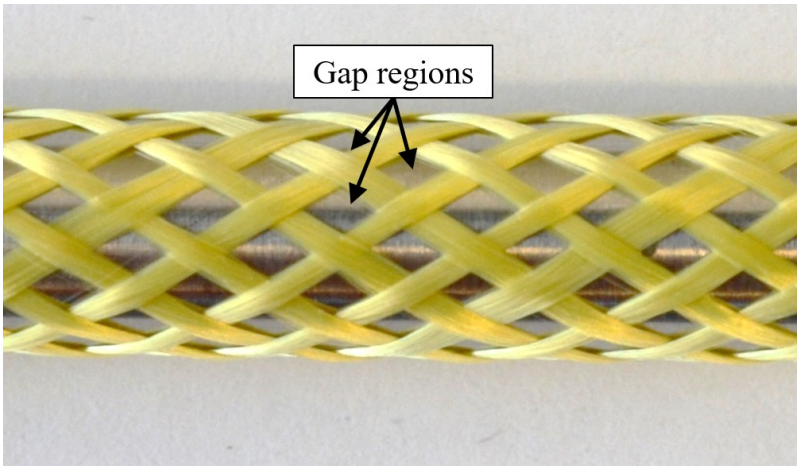

Figure 3-1: Image of open mesh braid preform with large gap regions

To maintain consistency between sample types as much as possible, an 1140 denier Kevlar 49® yarn was used. The individual filaments for both Kevlar 49® yarns have the same properties, and the change in denier only changes the number of filaments present.

3.2.2 Curing systems

3.2.2.1 Overview

Two different curing systems were used for manufacturing the composite matrix in the composite strands and in the TBCs. The Epon 826 / Lindau LS-81K resin and hardener combination is an industry recommended curing system for composite pultrusion and filament winding applications [97]. This combination has been previously used in the laboratory and is part of an ongoing work to create a pultrusion-based continuous composite braid manufacturing line [29], [98].

EcoPoxy® Clear Resin and Hardener is a commercial non-toxic epoxy for composites manufacturing and wood laminating [99], [100]. Similar to BioMid™, the documentation of this particular epoxy in the scientific literature is limited [54], [101].

3.2.2.2 Application

Initially, it was intended that both systems be used throughout testing only with their aforementioned counterparts; that is, that all Kevlar 49® specimens be cured with the Epon 826/Lindau LS-81K system and all BioMid™ specimens be cured with the EcoPoxy® system. This was the case for the composite strand testing.

However, during the manufacture of TBC specimens, it was found that the EcoPoxy® resin did not debond well from the surface of the PTFE curing mandrels and removal resulted in significant damage to the specimens. Thus, for the TBC manufacturing, only the Epon 826/Lindau LS-81K curing system was used. An area for future study would be to improve the manufacturing process or identify an alternative resin that would meet the 'green' criteria.

3.3 Specimen preparation

All specimens for testing were prepared in-house. This included the dry yarn samples, the composite strands, and the TBCs.

3.3.1 Safety and other precautions

Nitrile gloves were used for handling of all materials, both for user protection and to avoid contamination. All handling of uncured resin constituents was performed with an N95 dust mask in a negative pressure enclosure to limit inhalation.

3.3.2 Dry yarn preparation

Specimens were taken directly from the manufacturer spools immediately prior to testing, and twist was added once the sample was mounted in the test clamps. No further preparation was required. The six different types of specimens used are summarized in Table 3-1.

Table 3-1: Summary of dry yarn specimens prepared

Material	Twist level		
	None	Low	High
380 denier Kevlar 49	0 tpm	80 tpm	160 tpm
1650 denier BioMid	0 tpm	40 tpm	80 tpm

Ten successful specimens for each type were required during testing.

3.3.3 Composite strand preparation

For the composite strands, specimens were prepared in groups of approximately 5-8 specimens each, rather than individually, due to the multiple preparation steps required in manufacture. Specimen lengths of 250 mm were used for testing, due to space constraints in the curing oven. Figure 5-3 provides a schematic of the process used for sample preparation.

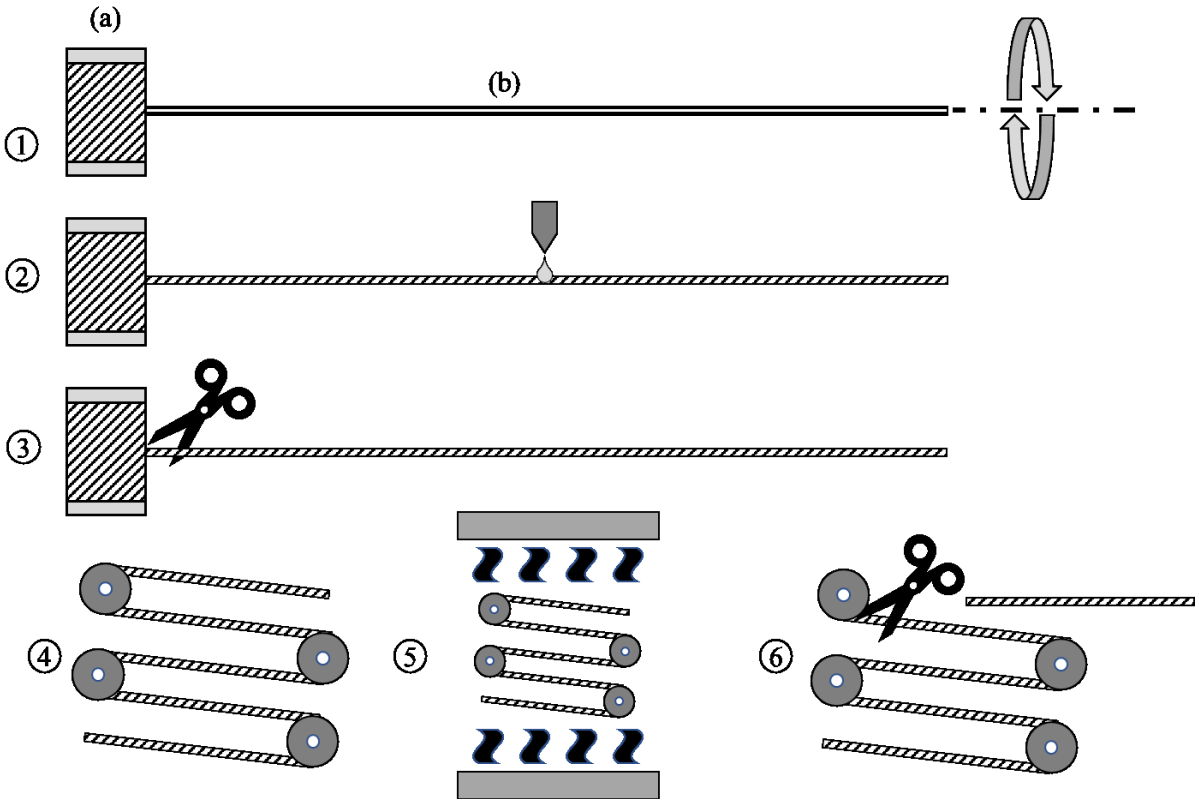

Figure 3-2: Schematic of specimen preparation for unidirectional composite strands, where (a) is the spool of untwisted yarn and (b) is the length of yarn extracted for preparation.

3.3.3.1 Procedure

The following process was used for preparing the composite strand samples,

1. A length of yarn was first measured out and fixed on one end. Twist was then applied, if necessary, by rotating the free end until the desired measure of twist was obtained.
2. The epoxy and hardener combination was mixed at the appropriate ratios and the resin manually applied to the length of yarn. Excess resin was removed by carefully squeezing along the length of the yarns. The samples were permitted to rest for a few minutes, well within the handling time of the resin. During this time, excess resin would bead on the surface of the yarn, and was then removed a second time to ensure no resin beads would remain during the curing process.
3. The length of yarn was carefully removed, without altering the twist
4. The impregnated yarn was wound around a custom curing rack, allowing for multiple specimens of 300 mm to be cured from the same strand

5. The entire curing rack and impregnated strand assembly was placed into the laboratory oven.
6. Once cured and cooled, straight sections of cured composite strands were cut from the assembly and placed into a sealed plastic bag to avoid subjecting the strands to changes in humidity.

Table 3-2 provides a summary of all the specimen types prepared for testing. Note the samples prepared were identical in twist treatment to those prepared for the dry yarn testing.

Table 3-2: Summary of composite strand specimens prepared

Material	Twist level		
	None	Low	High
380 denier Kevlar 49, Epon 826 / Lindau LS-81K	0 tpm	80 tpm	160 tpm
1650 denier BioMid, Ecopoxy	0 tpm	40 tpm	80 tpm

Again, ten successful specimens were required during testing. Thus, approximately 20 specimens of each type were prepared beforehand. Even though it was attempted to remove as much excess resin as possible prior to curing, some samples still produced resin beads during the curing process. These did not affect testing so long as the beads were not in the clamp region of the test grips.

3.3.3.2 Curing oven

A laboratory oven was used for the curing of samples that were prepared with EPON 826 resin. The oven was controlled via a PID temperature controller (Omega CN5700 Microprocessor Based Temperature Process Control, Omega Engineering Inc., Norwalk, Connecticut, USA). For the EPON 826 / Lindau LS-81k resin, the recommended temperature profile from the manufacturer as described in Appendix A was used. The temperature controller was programmed with a ramp and hold profile to match the recommended profile, with 10 minute ramp periods between the hold temperatures. When preparing specimens with the EPON 826 / Lindau LS-81k resin, the oven was held at 66°C. Once the specimens were loaded into the oven the program shown in Figure 3-3 was run to achieve full sample cure.

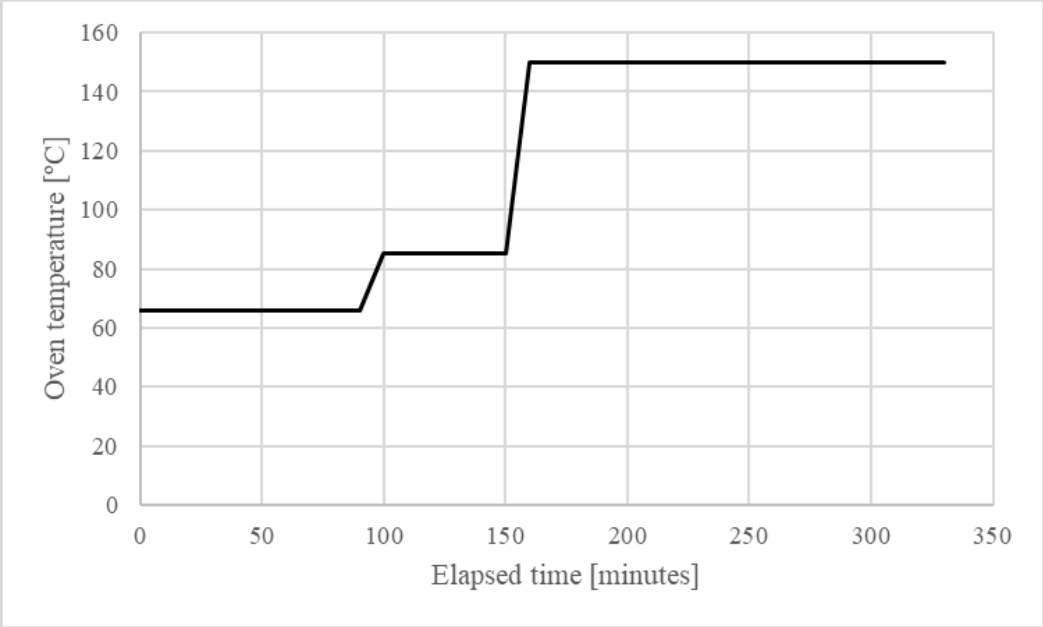

Figure 3-3: Graph of temperature controller input program showing ramp and hold temperature profile

The controller was auto-tuned to the oven prior to use and thus custom PID settings were not applied. Once the curing cycle had been completed, the specimens remained in the oven and were allowed to cool passively to room temperature prior to handling.

3.3.4 TBC specimen preparation

3.3.4.1 Twist counter

A custom twist counting device was used throughout sample preparation in order to obtain the correct level of twist, as shown in Figure 3-4.

Figure 3-4: Images of custom twist counter. The handle (a) is rotated to turn the braider bobbin (b) and twist the yarn (c) about its axis. The analog counter (d) records the number of turns of the braider bobbin.

This simple device counted the number of rotations performed by the output shaft. With the other end of the yarn fixed from rotation, the free end was attached to the twist winder and the number of rotations were then measured by the analog counter. The device was manufactured from a film winder and custom 3D printed parts.

3.3.4.2 Maypole braider

A small medical type braider (Steeger K80-72, Steeger USA Inc., SC, USA) was used for manufacturing all tubular braid preforms. An image of the braider in operation is shown in Figure 3-5.

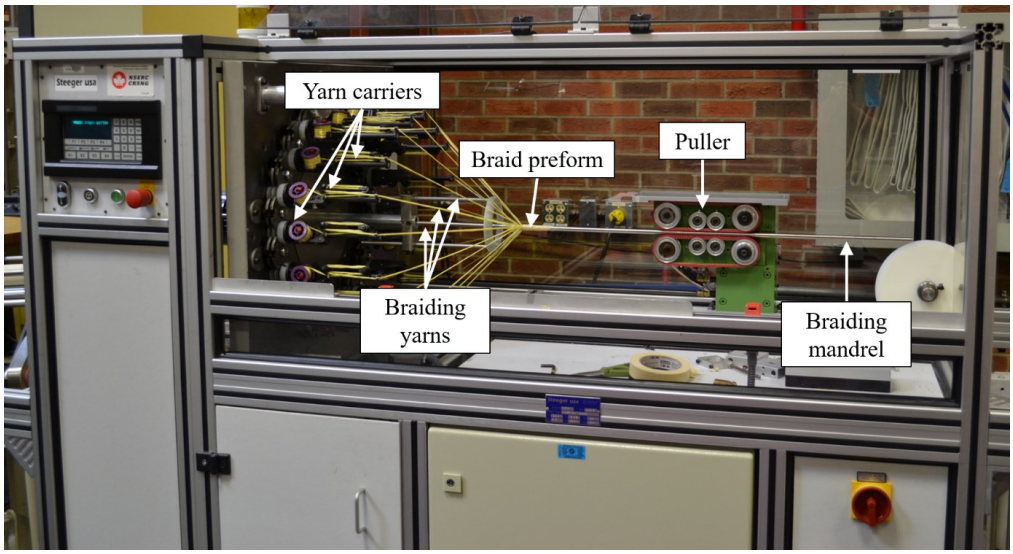

Figure 3-5: Image of maypole braider during braid preform manufacture.

This braider was originally intended for the manufacture of wire stents but has since been repurposed for the braiding of multifilament yarns. Identification of critical components in the braiding process is provided in Figure 3-6.

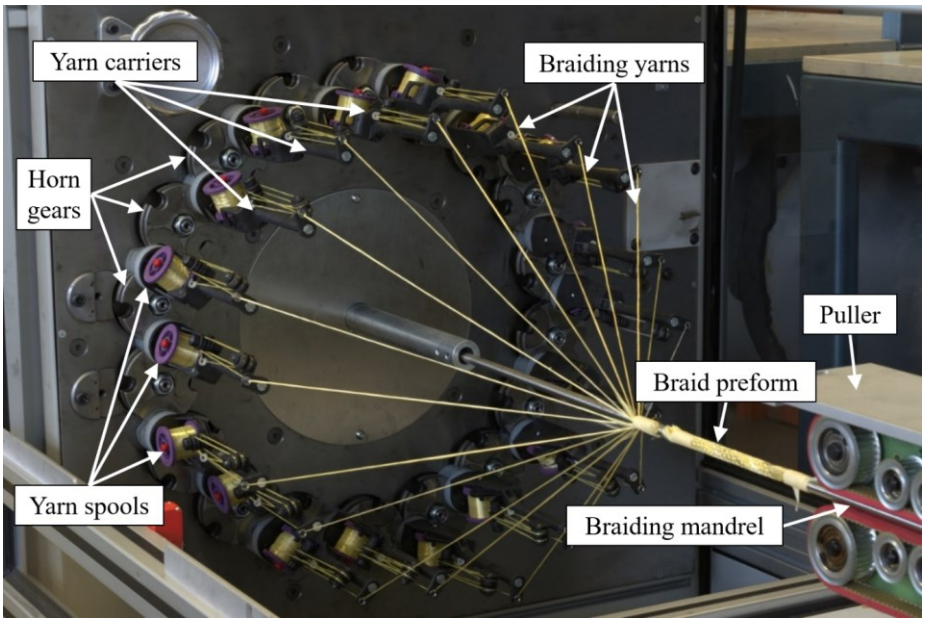

Figure 3-6: Close-up image of maypole braider during preform manufacture

The full load capacity of the braider is 36 carriers. Each carrier holds a single spool of yarn for braiding, as shown in Figure 3-7.

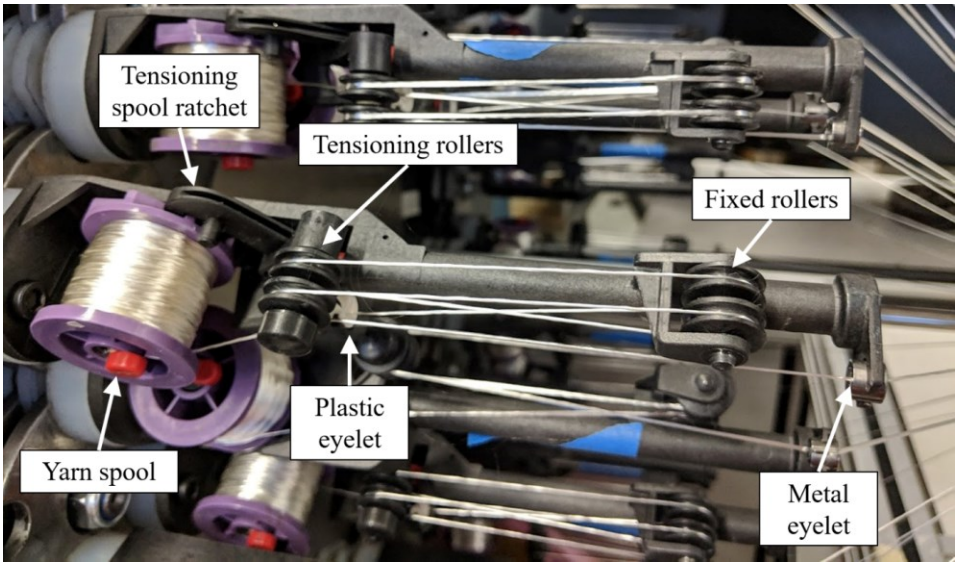

Figure 3-7: Image of braiding yarn carrier

During braid manufacture, the spur gears of adjacent horn gears mesh and result in a circular serpentine path for each of the braid carriers. An image of the exposed horn gears is shown in Figure 3-8.

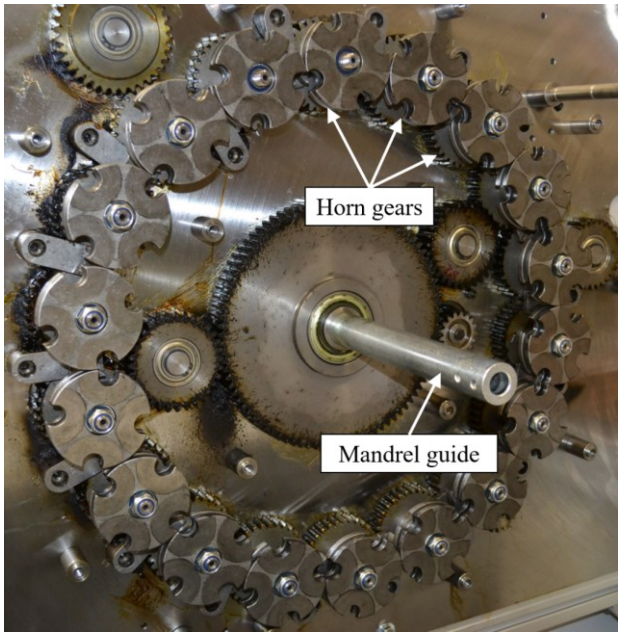

Figure 3-8: Image of exposed braider horn gears

During the braiding process, the carriers are inserted into the horn gear slots in a specific pattern depending on the desired braid pattern, as shown in Figure 3-9a. Since each adjacent horn gear meshes at a 1:1 ratio with its neighbours, each adjacent horn gear spins in an opposite direction. This is what creates the serpentine motion shown in Figure 3-9b.

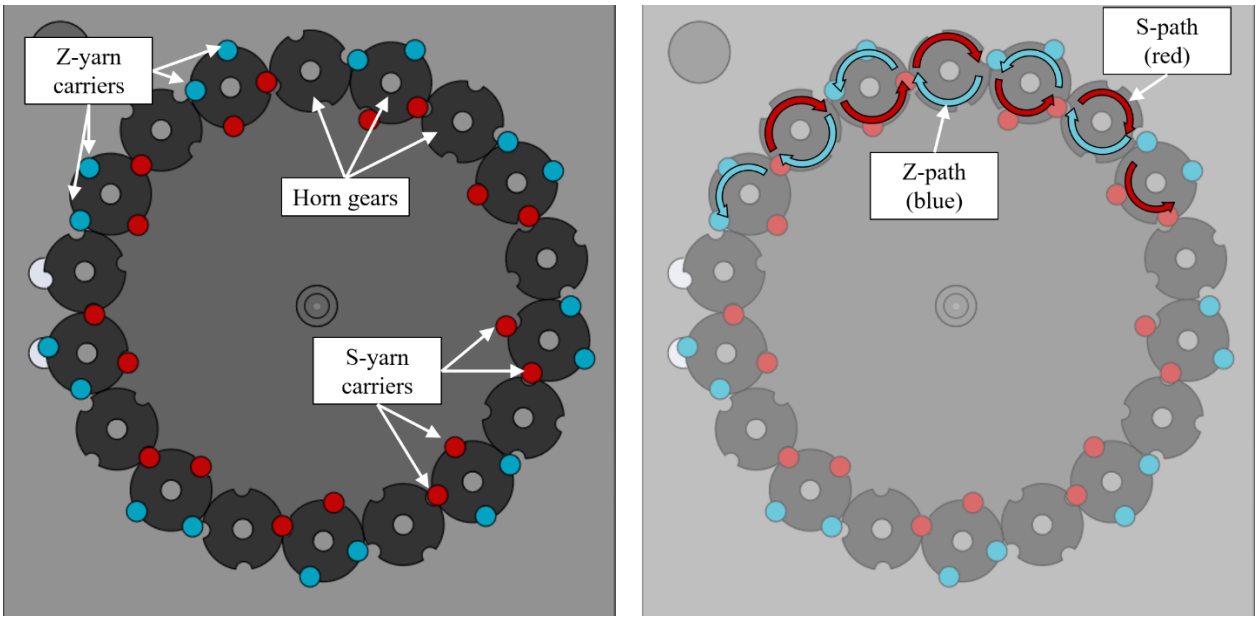

(a) **(b)**

Figure 3-9: Schematic of (a) Regular braid pattern settings and (b) path of each set of yarns

It is the interlacing of the yarns that creates the braid pattern. In Figure 3-10 the interlacing of the two over, two under pattern of the Regular braid can be seen to be forming in the convergent

zone of the braiding process. The fell point is where the braiding yarn contacts and begins to wrap around the braiding mandrel. The convergent zone is defined as the region between the braid carrier outlets and the fell point, where the yarns converge to form the braid.

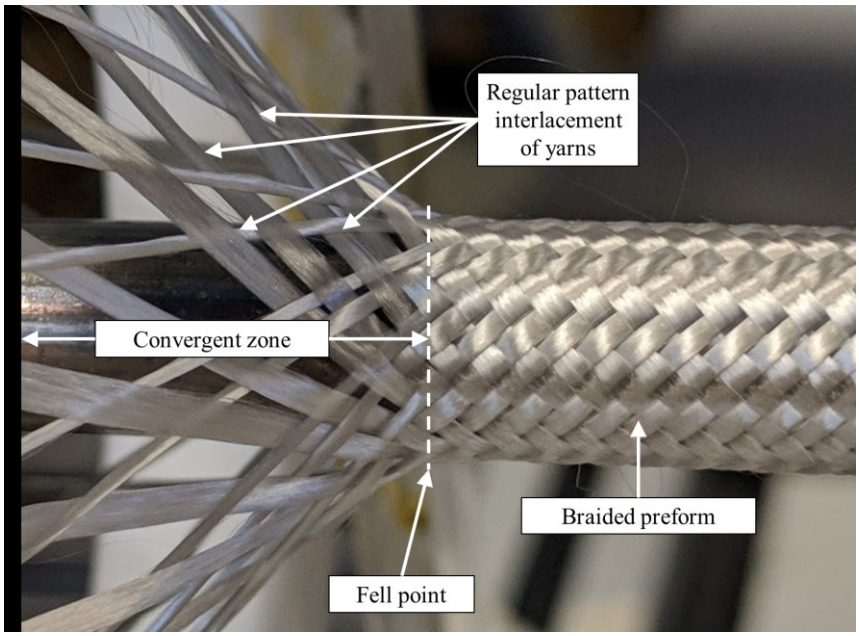

Figure 3-10: Image of convergent zone and fell point of braiding process for Regular braids [7]

Figure 3-11 provides a close-up look at the Regular braid pattern. Again, each yarn passes over and then under two consecutive interlacing yarns as it wraps around the braided preform.

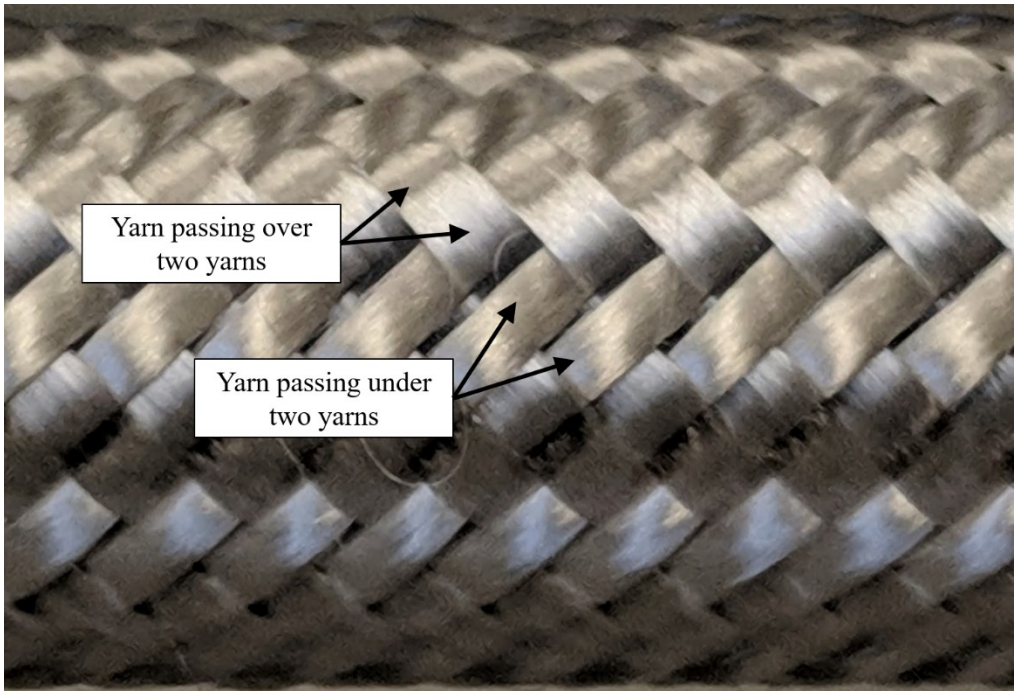

Figure 3-11: Close-up image of Regular braided preform

Both the interlacing motion of the braider yarns as well as the puller advancement of the preform mandrel are controlled by the braider. The ratio of the braider and the puller determines the geometry of the braid [7] and with this particular braider the ratio is controlled indirectly through an input of PPI (picks per inch). The braider was operated at 15 PPI using 3/8" steel mandrels, which yielded the 45° braid angle targeted.

3.3.4.3 TBC manufacture

The process shown in Figure 3-12 was used to produce all the braid preforms and manufacture the TBCs in house.

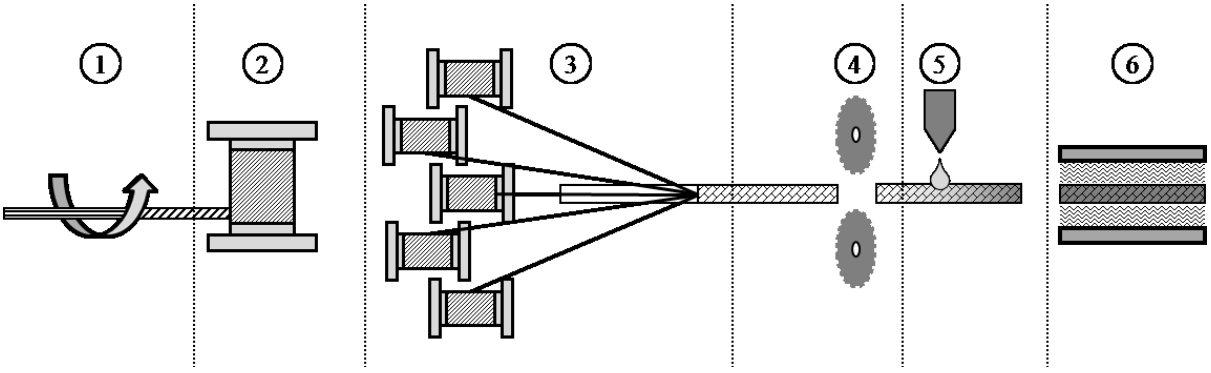

Figure 3-12: Schematic of tested and proposed twisted braided composite process.

1. Lengths of yarn were twisted to a level of 80 tpm using the custom twist counter described in section 3.3.4.1.
2. The yarns (twisted and untwisted) were wound onto the braider bobbins.
3. Braids were manufactured with a Regular braiding pattern, at a braid angle of 45°, onto steel mandrels with an OD of 9.525 mm. Approximately two meters of each braid type were manufactured continuously. Masking tape was used to mark the portion of braid at which the fell point and convergent zone of the braiding yarns achieved a steady state, to avoid variation in the braid angle [7].
4. The braided preform was cut into 20 cm lengths, with tape around the ends to prevent unraveling. Figure 3-13 shows a sample preform prior to impregnation.

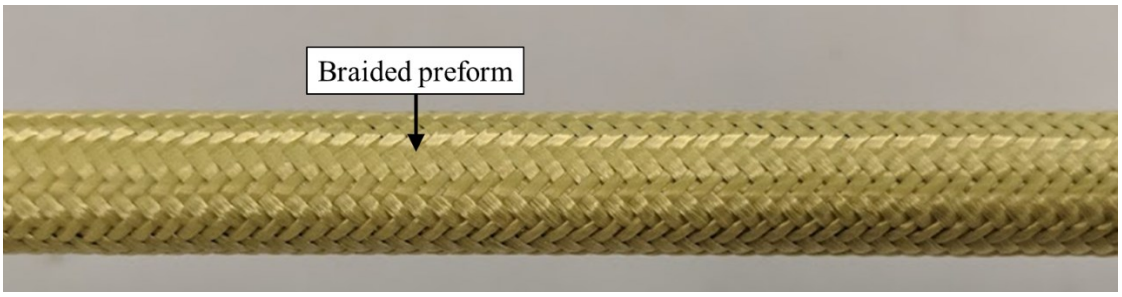

Figure 3-13: Image of braided preform prior to resin impregnation

5. Cut preforms were mounted onto PTFE sleeved mandrels, with an OD of 9.525 mm. The epoxy and hardener were then mixed and manually applied to the samples. Resin was poured onto the samples and allowed to soak into the braid, followed by a manual massaging to ensure complete impregnation. Light pressure was applied to remove excess resin.
6. Specimens were vertically mounted and placed in the oven and subject to the cure profile shown in Figure 3-3.
7. Once cured and cooled, specimens were removed for testing. A small amount of torque applied to the TBC easily released it from the PTFE sleeve without damaging the specimen. Figure 3-14 shows a cured specimen prior to removal from the mandrel.

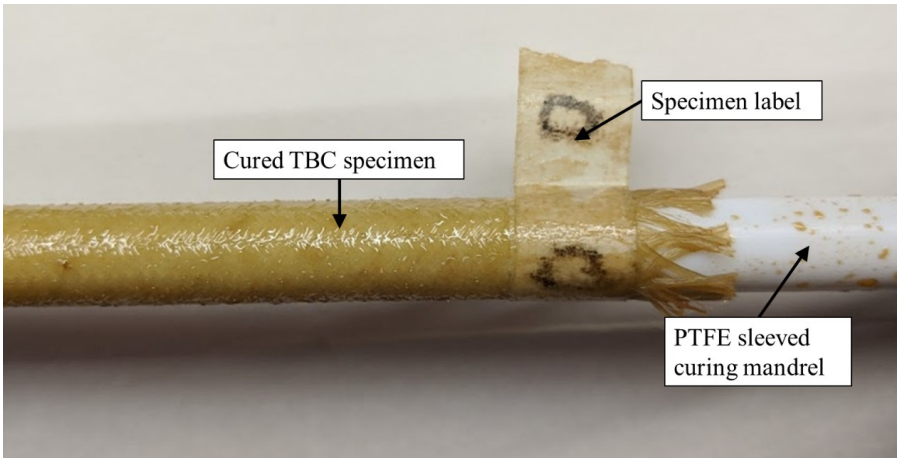

Figure 3-14: Image of cured TBC specimen prior to removal from PTFE sleeved mandrel

8. Samples were trimmed to about 120 mm to 150 mm in length with a saw and custom mitre trimming guide. Regions of the TBC with non-uniform braid angle or other defects were removed as a type of quality control. Exact length was not required nor necessary as specimens were each measured prior to testing. Figure 3-15 provides an example of the material discarded during this step.

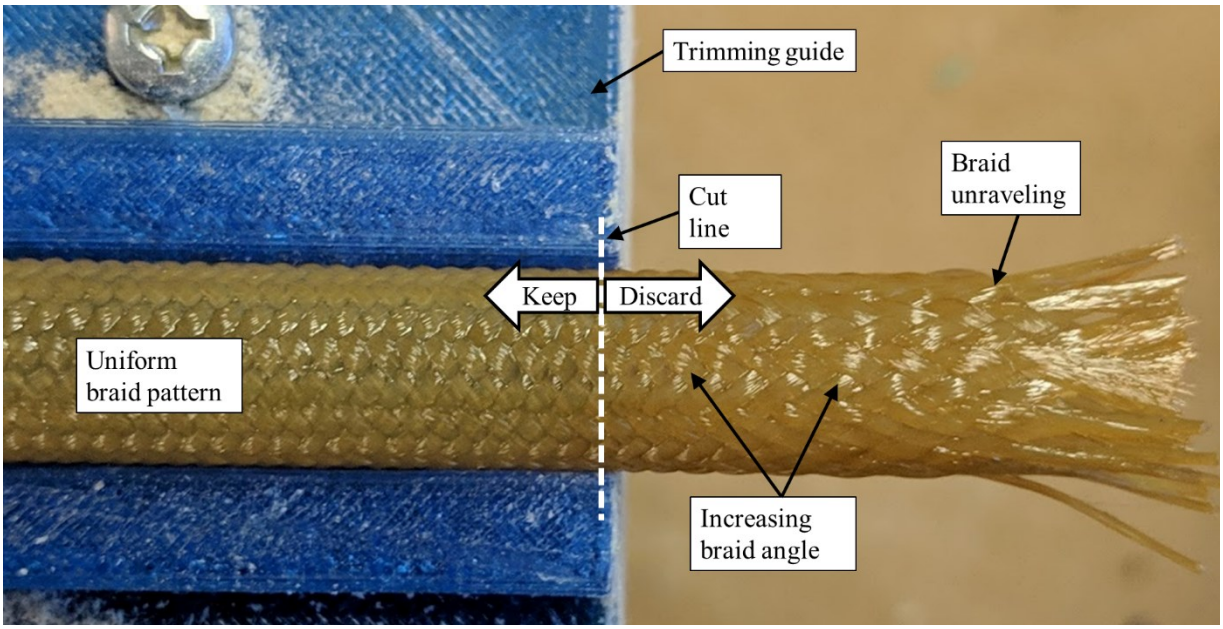

Figure 3-15: Image of cured TBC sample after removal from curing mandrel and prior to trimming. Note the change in braid angle and unraveling of braid in the region past the cut line.

This concluded the necessary specimen preparation to achieve the mechanical structure of the TBCs. Table 3-3 provides a summary of the eight different types of specimens prepared throughout this process.

Table 3-3: Summary of TBC specimens prepared

Material	Twisted yarns		
	No twist	Half-twist	Full-twist
1580 denier Kevlar 49, Epon 826 / Lindau LS-81K	Z-0/S-0	Z-S/S-0	Z-Z/S-S, Z-S/S-Z
1650 denier BioMid, Epon 826 / Lindau LS-81K	Z-0/S-0	Z-S/S-0	Z-Z/S-S, Z-S/S-Z

Additional steps were required in order to prepare the TBC specimens due to the end tabs required for tensile testing and the DIC strain measurement used.

3.3.4.4 TBC preparation for tensile testing

The tubular shape of the TBCs requires special mounting for tensile testing. Samples were first measured and then mounted on custom end tabs according to the following procedure.

1. The length, internal diameter, and outer diameter of each specimen was measured using a telescoping bore gauge (TESA USA, North Kingstown, RI) and a precision micrometer set (Mitutoyo 103-907-40, Kawasaki, Japan). Each measurement was repeated at three

distinct points on the sample and recorded to a precision of 0.0001”. Measurements were taken for every sample, and the mean value used for processing.

2. The tapered stem of an end tab (see Figure 3-16) was then glued to the end of each specimen using a two-part high shear strength epoxy (Loctite E-60HP, Henkel Corporation, Germany).

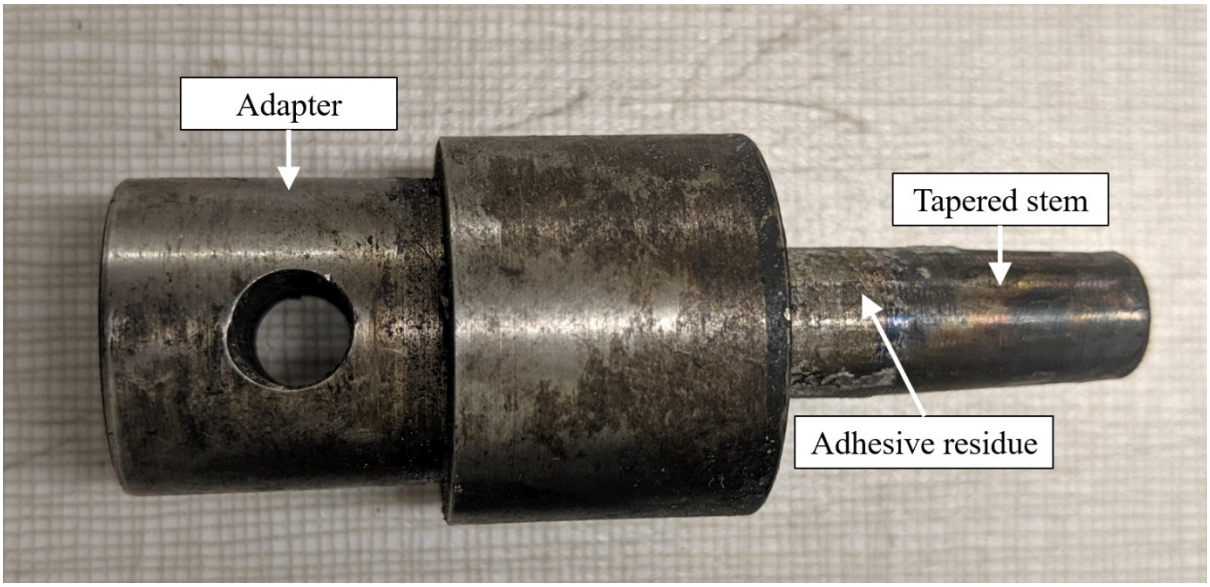

Figure 3-16: Image of end tab used for attaching TBC specimens to electrohydraulic test frame

3. Once sufficient gel strength had been obtained in the epoxy adhesive to prevent adhesive from flowing, samples were mounted horizontally and the end tabs fixed to a length of steel 90° angle L-bracket. This ensured the tabs and sample were mounted concentrically and that only tension and no bending was applied to the specimen during testing, as shown in Figure 3-17.

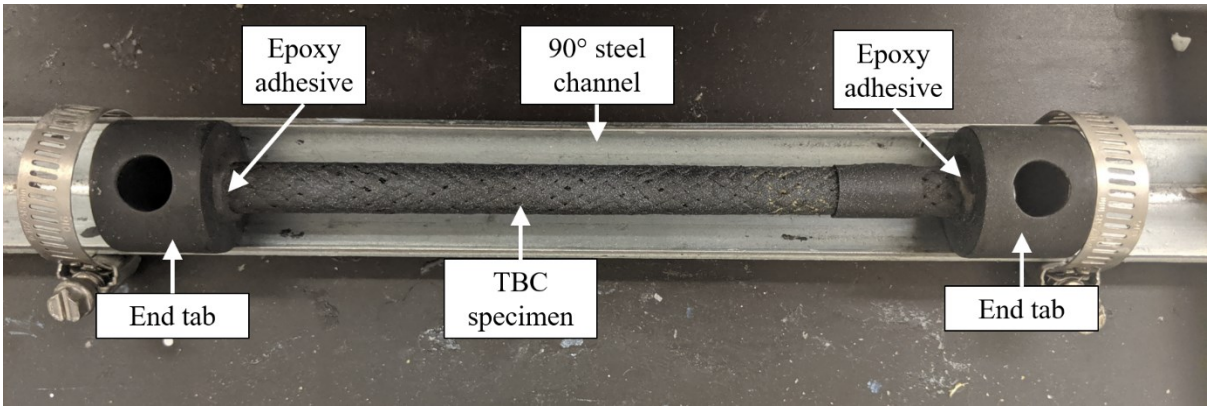

Figure 3-17: Image of end tab curing setup

4. Specimens remained fixed for 24 hours to ensure complete curing of the mounting adhesive.

3.3.4.5 TBC preparation for DIC analysis

Strain measurement for the TBC specimens was performed using a digital image correlation process. This required additional preparation to ensure sufficient contrast on the surface of the specimen. All painting was performed within a fume hood to prevent inhalation of gases and paint particles.

1. Flat black enamel spray paint (Flat black V2400 Economy Enamel, Rust-Oleum, Illinois, USA) was applied to the exterior of each sample and allowed to dry completely.
2. White airbrush paint (White Air Opaque, Badger Air-brush Co., IL, USA) was mixed to an appropriate viscosity and loaded into a manual airbrush (Paasche H Single Action Siphon Feed, Paasche, Wisconsin, USA) for sample speckling. Air pressure was kept at approximately 16 psi.
3. Samples were lightly sprayed with airbrush paint to achieve the desired speckling pattern and allowed to dry completely prior to testing. Visual inspection was used to determine the quality of the speckling pattern. Figure 3-18 shows a monochromatic image of the speckled specimen ready for image capture.

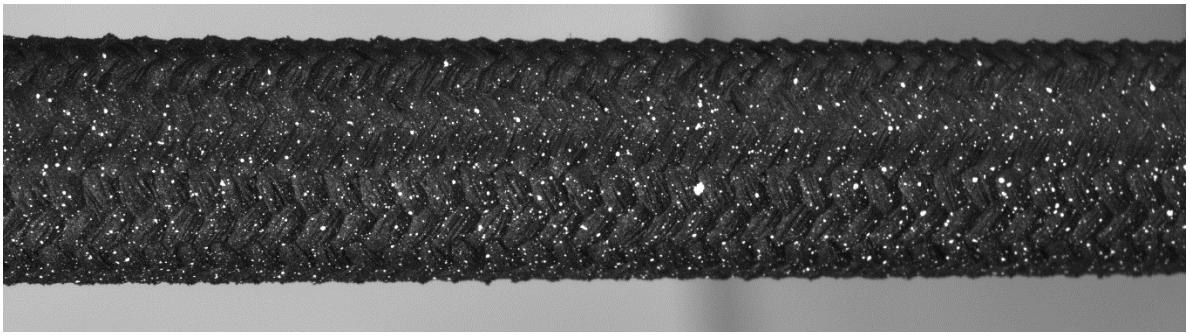

Figure 3-18: Image of sample TBC specimen with speckling pattern applied.

Due to the time-consuming nature of the overall specimen preparation and testing process, fewer specimens were manufactured than the two previous experiments. Approximately ten specimens of each configuration were prepared, and approximately five successful specimen tests were targeted for each configuration and material.

3.4 Tensile testing

All three types of specimens were subject to tensile testing. Standards were followed where reasonable or applicable [42], [102], [103]. Samples were tested under constant rate of extension with quasi-static rates.

3.4.1 Dry yarn testing

For the dry yarn samples, each specimen was handled from preparation through testing individually. Samples were tested using the Bollard type test grips in the electromechanical tensile frame.

3.4.1.1 Bollard type test grips

Standard clamp-style test grips are not appropriate for use with tensile yarns, as a stress concentration occurs right at the grip face and initiates failure prematurely. In order to prevent this, Bollard type test grips are recommended [103]. A pair of these were designed and manufactured for the test frame. The specimen passes over a guide pulley prior to clamping in order to reduce the stress concentration at the clamp face, while theoretically maintaining an even tension throughout. A thumbscrew is used to tighten the clamp faces together and secure the sample. A close-up view of the test grip as well as the experimental setup is provided in Figure 3-19.

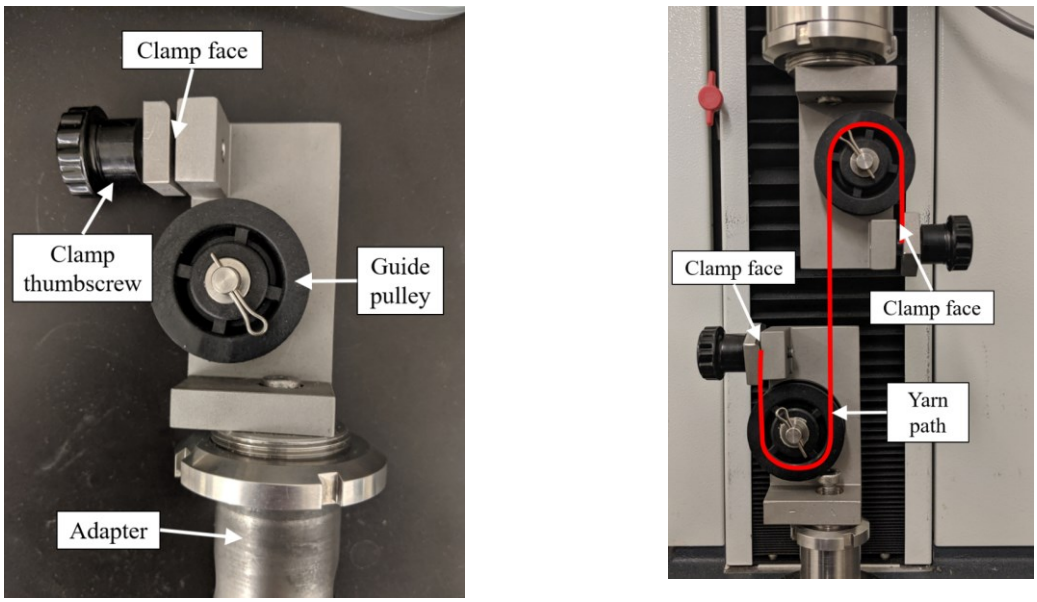

(a) (b)

Figure 3-19. Images of (a) close-up view of custom Bollard-type yarn grip, and (b) testing setup including overlay of yarn path during testing

The manufacturing drawings for these Bollard-type grips is provided in Appendix D.

3.4.1.2 Electromechanical tensile frame

The dry yarns and composite strands were tested on an electromechanical tensile test frame (MTS Synergie 400, MTS, Eden Prairie, MN, USA.) with a 500 N uniaxial load cell (MTS, Eden Prairie, MN, USA). Machine control and data acquisition were performed with the supplied software (TestWorks 4, MTS, Eden Prairie, MN, USA). Extension data (in millimeters), load data (in Newtons), and time data (in seconds) were captured for each specimen, tested under constant rate of extension.

3.4.1.3 Procedure

1. A yarn approximately 600 mm in length was taken from the yarn spool.
2. The yarn grips were fixed such that the clamp face to clamp face length measured 500 mm. Each sample was loaded into the grips and the clamps lightly closed.
3. Yarns were twisted by rotating one of the yarn grips while fixing the other. Yarns were permitted to slide in the grips to avoid pre-tensioning.
4. Yarns were re-mounted to ensure even twist throughout the specimen, with care taken to not remove or add any twist at this point.
5. A small amount of pre-tension was applied (<2 N) to limit start-up slack during testing.
6. Yarns were tested at a constant cross head rate of 100 mm/min up to failure. Specimens that failed at or near the clamp faces were discarded from results.
7. Broken yarns were removed from testing setup and disposed of. Grip position was reset to ensure 500 mm specimen lengths.

3.4.2 Composite strand testing

Composite strands were tested similarly to the dry yarn procedure described in section 3.4.1 with a few exceptions. Twist was not applied in the test grips as samples were already twisted, sample length was decreased to 250 mm. and the rate of extension was decreased to 2 mm/min.

3.4.3 TBC testing

Samples were tested under constant rate of extension via an electrohydraulic tensile test frame.

3.4.3.1 Electrohydraulic tensile frame

The TBCs were tested on an electrohydraulic tensile test frame (MTS, Eden Prairie, MN, USA) with a 5 kN uniaxial load cell (MTS, Eden Prairie, MN, USA).

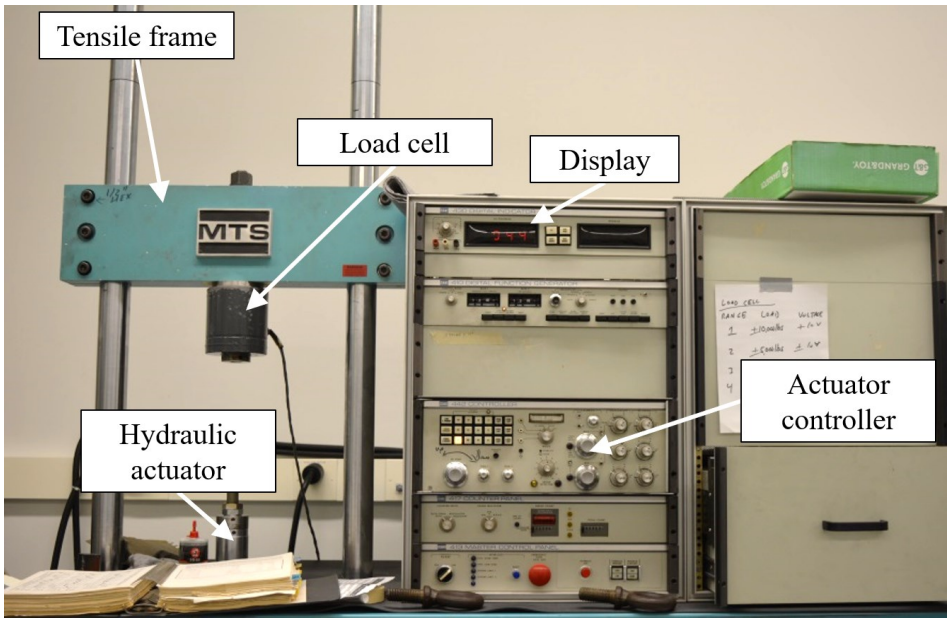

Figure 3-20: Image of electrohydraulic tensile testing machine

Each of the components of this machine are independently controlled. Samples were tested under stroke control, that is the extension rate was directly controlled and input. Voltage readout from the load cell can be read directly from the display during operation, but is used as a general indication of load only.

3.4.3.2 Load data acquisition

The voltage output from the load cell was converted to a digital signal using a multifunction DAQ device (NI USB-6211, National Instruments, TX, USA). This digital signal was then read into a custom data acquisition program in Matlab (Matlab R2017a, Mathworks Inc., MA, USA) for conversion into load data. No load feedback was used for control.

3.4.3.3 Procedure

This section details the procedure used in the testing of the TBC samples. However, the details regarding image capture and DIC processing will be discussed in detail separately in section 0 for the sake of clarity. Image capture occurred simultaneously to tensile testing, as both imaging and load data were acquired using the same custom program.

1. The specimen was loaded into the test frame. The end tabs were pinned to the hydraulic actuator and load cell. A slight amount of pre-tension was applied to verify alignment and pinning of specimen.
2. The desired test rate was set such that failure, in this case defined by maximum load capacity, of the sample occurred within one to two minutes of testing. For Kevlar 49® TBCs this was a rate of approximately 2 mm/min while for the BioMid™ TBCs, this was approximately 1 mm/min.
3. The imaging and data acquisition program was started.
4. Once the image acquisition had begun, the programmed ramp function on the electrohydraulic test frame was started.
5. Once a maximum load had occurred prior to specimen necking, the ramp rate was increased to speed up failure of the specimen.
6. Failed specimens were removed and imaging and acquisition program stopped.

3.4.4 Digital image correlation (DIC) methodology

3.4.4.1 Experimental setup

Two CCD cameras (AVT Prosilica GT3400, Allied Vision Technologies GmbH, PA, USA) were used to capture images in a stereo image configuration during tests.

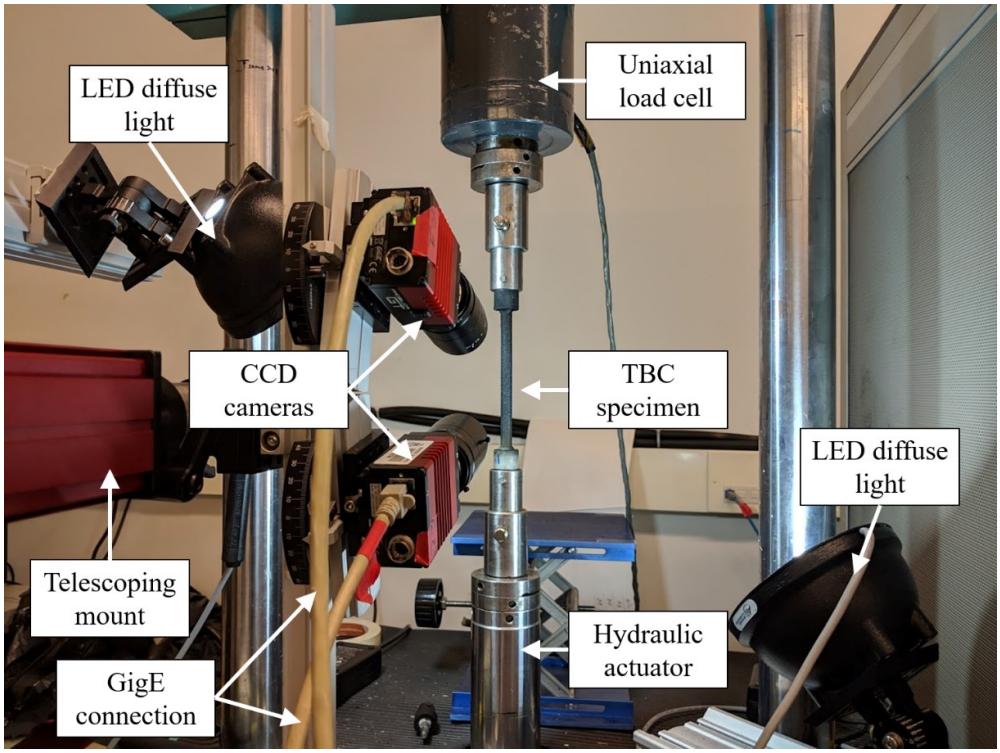

Figure 3-21: Image of imaging setup for tensile tests

Light was provided by two LED diffuse lights mounted at oblique angles to the specimen. These lights limit glare by providing a diffuse source, but it was found that during testing even lighting of the sample required careful placement of the lights such that a direct reflection into one of the cameras did not occur.

Each camera was fitted with a 1" C-mount 35 mm fixed focal length lens (LM35SC, Kowa USA, CA USA) at an approximate aperture of f8. The pair of cameras were mounted on sliding rotation platforms (XT66RP1, Thorlabs, Inc., NJ, USA) which allowed for the angle of the camera to be easily determined during setup, as shown in Figure 3-22.

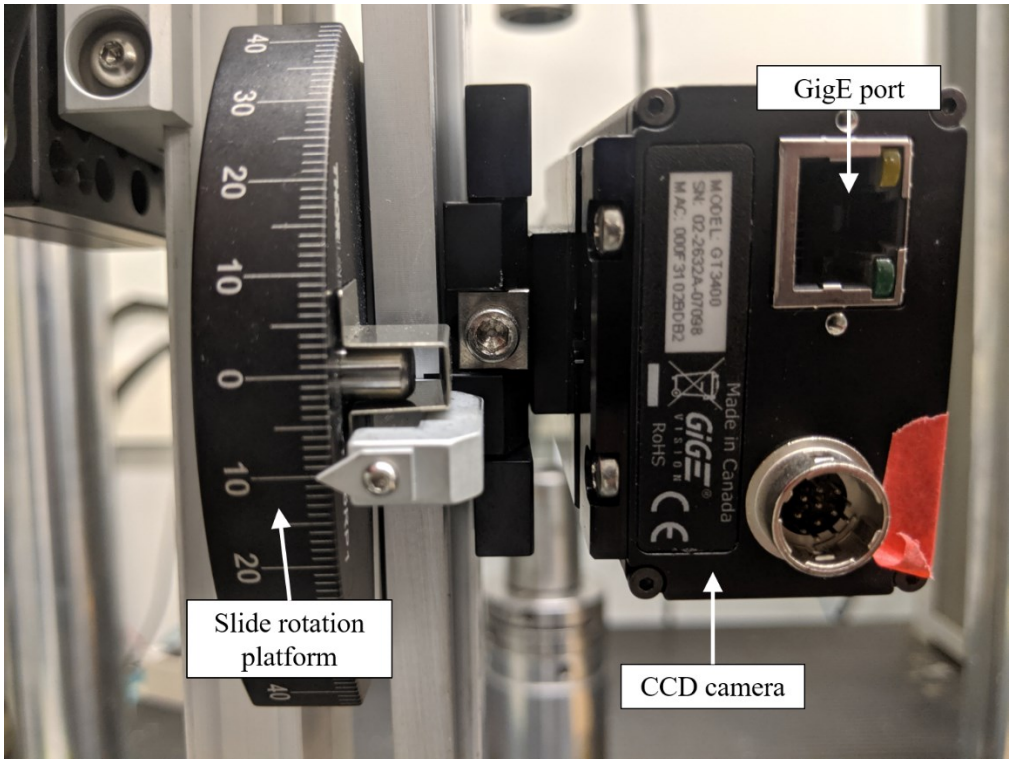

Figure 3-22: Image of close-up view of sliding rotation platform and mounted camera

The target stereo angle between the two cameras was 22.5°. Best practices dictate a stereo angle between 15° and 35° [104]. Each camera was thus positioned at an angle of 10° to 12° relative to the horizontal plane, as shown in Figure 3-23.

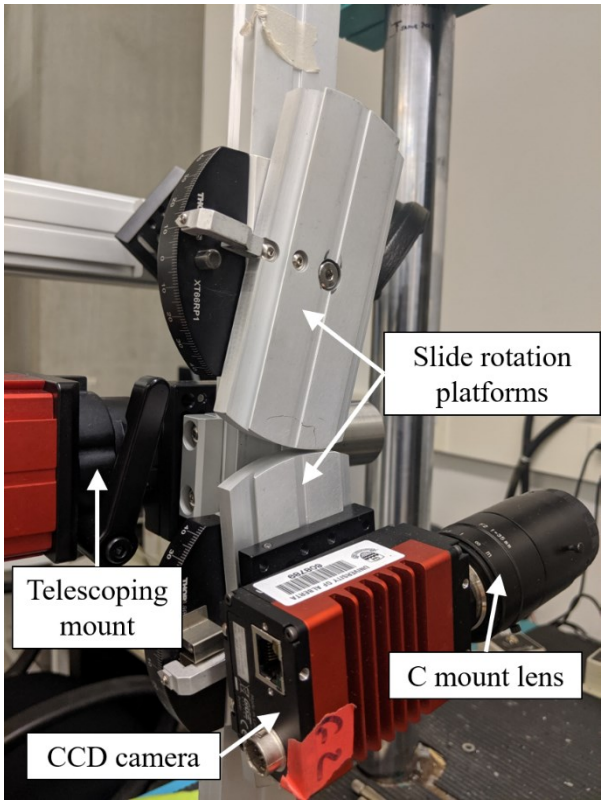

Figure 3-23: Image of slide rotation platforms mounted in stereo configuration on telescoping mount

The slide rotation platforms were mounted together on a single rail so that images would be captured along the same plane. This limited the amount of out-of-plane rotation between the two cameras to the desired stereo angle only. The rail was then fixed to a telescoping mount so that the entire setup could be easily adjusted without changing the stereo configuration. Finally, the whole setup was mounted on a breadboard supported by a passive isolation support frame (B2448Fand PFP6090-8, Thorlabs, Inc., NJ, USA) to prevent vibration transfer to the cameras during operation.

The field of view for each camera was approximately 40 mm by 60 mm. The combined ROI, after image cropping, was approximately 10 mm by 60 mm. Selecting the field of view was a compromise between resolution of the speckled surface and length of specimen captured during tests due to the high aspect ratio of the TBC. A stand-off distance of 40 mm allowed for sufficient speckling resolution while capturing enough of the sample to provide useful and meaningful results.

3.4.4.2 Camera calibration

Given the field of view of the experimental setup, a custom 3D stereo calibration target was designed and machined from 6061 aluminum. This calibration target has feature diameters of 1.2 mm, a feature-to-feature distance of 5 mm, and a height separation of 1 mm. An image of the target is provided in Figure 3-24 and a detailed manufacturing drawing is provided in Appendix D.

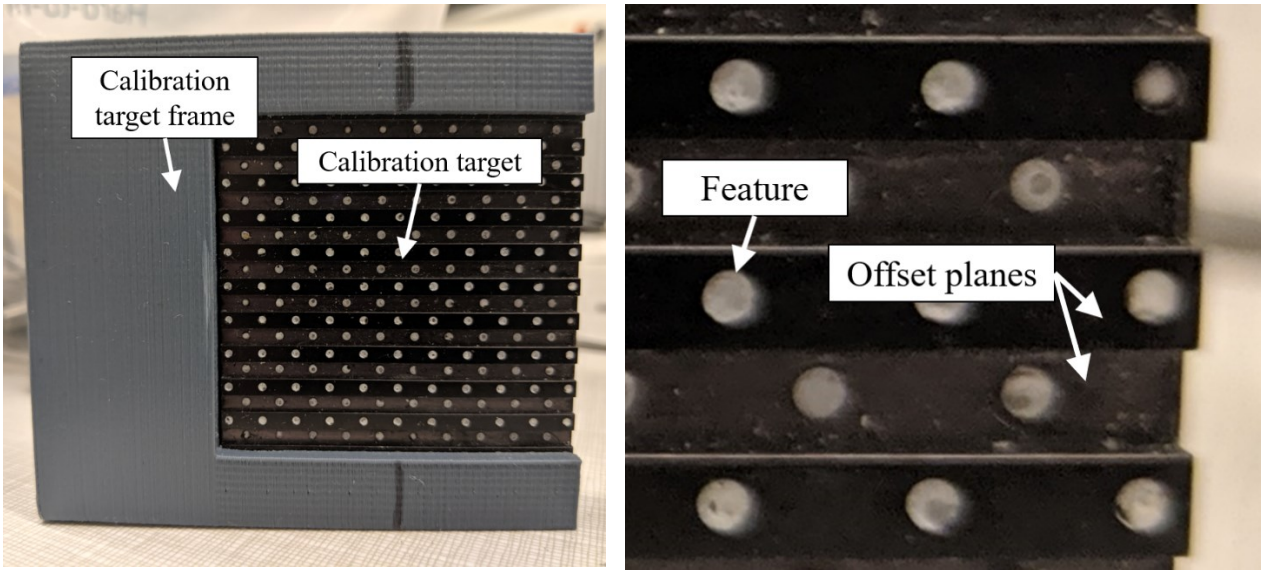

(a) (b)

Figure 3-24: Image of calibration target (a) in frame and (b) close up to view features and offset between planes

Camera calibration was performed prior to testing and was performed each time the cameras were moved or adjusted. This consisted of taking an image while the calibration target was in view of the cameras. A sample pair of images is provided in Figure 3-25.

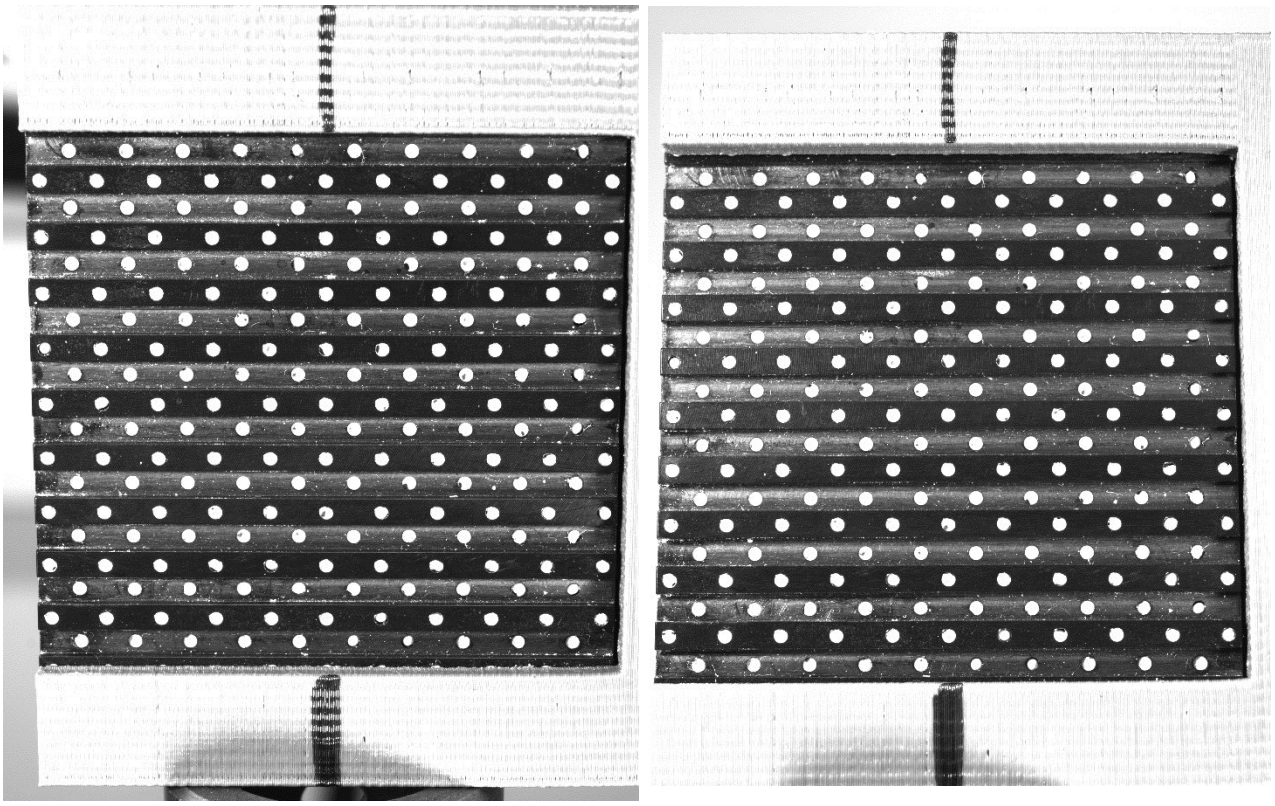

(a) (b)

Figure 3-25: Pair of images taken during calibration with a view from (a) the upper mounted camera one and (b) the lower camera. Note the difference in perspective of each image.

The calibration of camera positioning was performed in the DaVis workspace, which includes feature recognition and detection, fitting to a pinhole model, and scaling of the image sets to the correct spatial resolution.

3.4.4.3 Image setup and parameters

Optimal image exposure and gain settings were set once at the beginning of the test and remained fixed throughout to avoid any error due to automatic gain compensation. Care was taken to not cause any changes in lighting throughout each experiment, as these would negatively impact the correlation results. Image pairs were captured at a rate of 2 Hz and stored as .TIFF files. The time of each image capture was stored alongside in a separate data array along with the trigger time. This allowed for synchronization of the results with the load data once the test was complete. Cameras were connected to the acquisition computer via GigE protocol and a dedicated Ethernet camera capture card.

3.4.4.4 Image processing and correlation

Image preprocessing was done in DaVis. The following steps were taken with each image data set. Note that exact parameters may have varied for each test, but the general approach mentioned here was followed each time.

1. Image pairs combined into a single data set, time sequenced as pairs
2. Camera attributes (i.e. pixel size) applied to each set
3. Images masked to ROI (i.e. portion of image with TBC specimen)
4. Image filter applied to normalize intensity histogram across ROI (i.e. even out bright/dark regions)
5. Seeding points selected in reference image for use with LSM algorithm [105]
6. Image correlation performed using LSM algorithm

3.4.4.5 Postprocessing and interpretation

Once the deformation data had been acquired for each frame, strain could be interpreted from the deformation results. This was done both as full field strain and also using a virtual strain gauge. The deformation data was viewed both as a vector arrow display and as a colourized strain map, for parameters such as maximum normal strain, shear strain, and longitudinal strain. Though visually appealing, conclusions should not necessarily be drawn on the strain map data alone. Thus, this view was primarily used to guide discussion only rather than obtaining any numerical results.

The virtual strain gauge (VSG) averages the deformation results over a portion of the sample and provides a numerical value for uniaxial strain that can be used as if a physical strain gauge or extensometer was present during testing. Here, the VSG results were used to confirm the testing rate of each of the samples.

One of the advantages of using DIC during testing is that the data is preserved for future follow-up analyses. In this work, the DIC results have mostly been used as a guide. However, if there are specific directions to take with future work, the data is preserved and can be used again.

3.5 Data processing

Data was post-processed using Matlab (Mathworks) for all tests. Generally speaking, post-processing involved truncation of excess data (such as start-up slack and post-failure data), conversion between unit systems, and linear regression. In addition, three custom Matlab codes

were developed that are of specific importance to this thesis and are discussed in detail in Appendix E. The values sought for each test were generally elastic modulus, failure strain, and failure stress.

3.6 Statistical analysis

Once the data had been processed in Matlab and relevant values calculated, the following was performed on each set of data to determine the significant difference, if any, between twist treatments.

1. Mean and standard deviation of each grouping were calculated
2. One-way ANOVA was performed across the groupings at a significance of $\alpha = 0.05$
3. If the results were significantly different, the Tukey Honestly Significant Difference (HSD) post-hoc analysis was used to determine where the significant differences occurred, again at a significance of $\alpha = 0.05$

Mean and standard deviation were reported, as well as any significance between groupings. Additionally, the uncertainty of measurement was determined and is reported in Appendix C.

Chapter 4 Low twist yarn mechanics

A version of this chapter was submitted to the Journal of Engineered Fibers and Fabrics as "Characterization and modeling of low twist yarn mechanics" and has been accepted for publication.

4.1 Introduction

The use of twisted yarns in textile applications is a necessary step for yarns made up of short fibers to ensure that individual filaments do not separate during handling. For multifilament textile yarns composed of continuous filaments, twist is not required for a cohesive yarn, but can be added for improved handling. However, it has also been shown that the addition of twist at low twist angles has an impact on the longitudinal yarn modulus and the specific strength of high modulus yarns. In this work, the effect of low yarn twist on the mechanical properties of Kevlar 49 and BioMid yarns is explored. It is determined that twist does significantly affect both the stiffness and strength properties of multifilament yarns, and that existing models do not adequately capture the behaviour in the low twist region, and that the experimental results are better defined with a linear fit.

4.2 Background

A multifilament yarn is composed of many fibers, or filaments. For untwisted continuous multifilament textile yarns, filaments are oriented in a straight line with the longitudinal axis of the yarn, while twisted continuous filament yarns are oriented in a helical path. The addition of twist impacts multifilament yarns in a number of ways. Handling is improved, as the yarn maintains a more stable cross-section and cohesiveness of individual filaments is increased [2]. Some testing standards (such as ASTM D7269 and ASTM D885) require textile yarns to be tested at a specified level of twist [102], [103]. This is to ensure filaments within the yarn fail as uniformly as possible, rather than in a progressive fashion. It has also been shown by Rao and Farris [44] that the addition of twist even at relatively low twist angles has an impact on the longitudinal yarn modulus and the specific strength of high modulus yarns. Specifically, increasing the twist angle resulted in a decrease in the longitudinal modulus of the yarn. Small increases in yarn twist, up to 5°, increased the yarn strength. However, beyond this point additional twist has also been shown to reduce yarn strength.

Shah et al. [51] attribute these to two separate effects, the resistance to filament rupture and the resistance to filament slippage. As twist increases, the contraction force between filaments as well as the obliquity to the loading direction also increase. The contracting of filaments is believed to improve yarn tensile strength, while filament obliquity has a negative effect. The effect of twist is also different depending on the type of yarn used. These effects have been well documented for some of the more common synthetic yarns (Kevlar 29, Kevlar 49, etc. [44]) as well as some natural staple yarns ([66], [106]). BioMid is a textile yarn composed of regenerated cellulose with similar appearance to a synthetic multifilament yarn, and studies regarding the effect of twist on mechanical performance have not yet been performed on this material. Further exploration into the performance of BioMid could open up new opportunities to use sustainably sourced materials in structural composite applications.

4.2.1 Fiber twist models

The addition of twist into a yarn is expected to affect both stiffness and strength of the yarn under loading. In a twisted yarn, the orientation of the individual filaments increases in eccentricity to the longitudinal direction as the twist increases. This off-axis eccentricity results in a loss of longitudinal stiffness, the effect of which has been modeled previously. One of the earliest models, known as either the $\cos^2\theta$ model or as Gegauff's classic model [44] takes the change in fiber orientation into account, by accounting for change in fiber length respective to the change in length of the yarn. As shown in Figure 4-1, the helical path of an individual filament is shown relative to the yarn direction. Gegauff's model relates yarn strain to filament strain based on the helix angle.

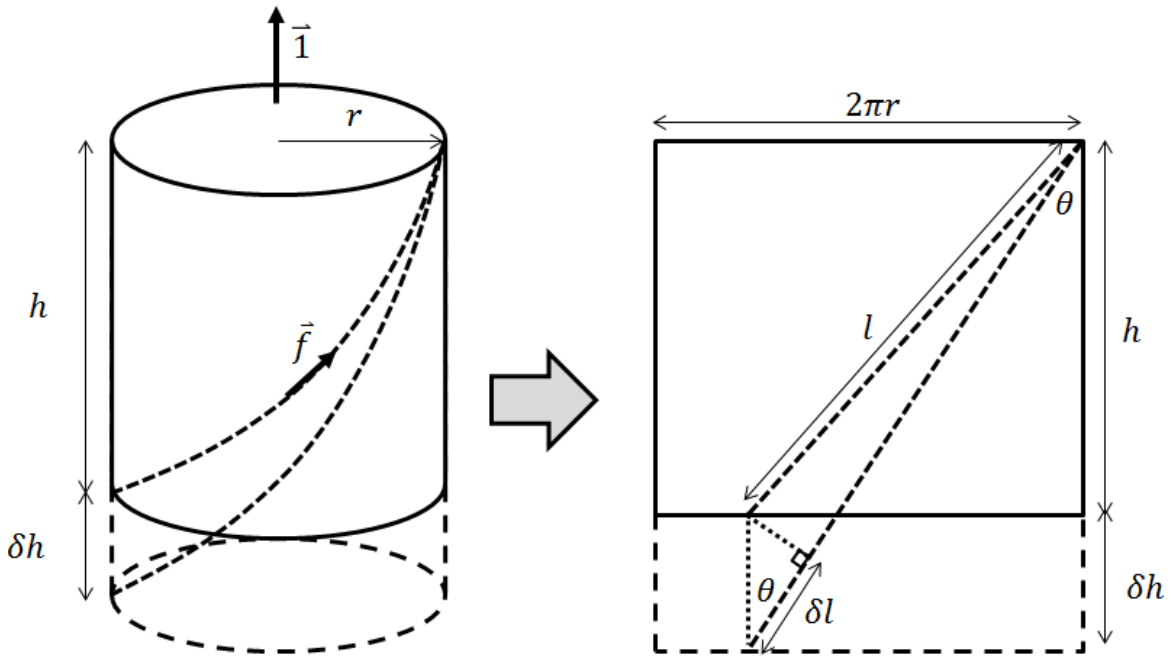

Figure 4-1: Schematic showing Gegauff's classical yarn model for yarn mechanics [44]**. On the left, the cylinder represents a twisted filament yarn in $\vec{1}$ direction and the helical path of an individual filament represented by the dashed line and $\vec{f}$. The unwrapped cylinder on the right shows the relationship between longitudinal yarn strain and filament strain.**

By accounting for the geometric relation between the height of the yarn h (same as the longitudinal length) and the individual filament length l the following relationship can be derived considering the variation of yarn twist with radial filament position [44] as seen in (4-1).

$$E_1 = E_f \times \cos^2 \theta \tag{4-1}$$

Where E_1 is the longitudinal yarn modulus, E_f is the elastic modulus of the filament and θ is the surface yarn twist angle. This model only takes into account the geometry of the filament and yarn and only accounts for the tensile filament strain. White [49] additionally accounts for the interfilament friction induced by the transverse forces applied from the added twist. In order to use this model, the magnitude and radial variation of the frictional yarn force must be known. Rao and Farris consider the rotation of the stiffness matrix created by the misalignment and orientation of the filament direction due to radial displacement and twist. Equation (4-2) results from considering the rotation of the stiffness matrix as well as the radial displacement of the filament within the yarn structure:

$$E_1 = E_f \times \left[\frac{3T_0 + 1}{2\,d\,T_0} + \frac{(1-d)^2}{d^3 \tan^2\theta} \cdot \ln\left(\frac{(1-d)T_0 + d}{T_0}\right)\right] \quad \textbf{(4-2)}$$

where $T_0 = \cos^2\theta$ and $d = \frac{E_z}{E_s}$ (the anisotropic ratio, the ratio between the longitudinal (E_z) and shear (E_s) moduli of the fiber but determined through curve fitting).

Naik and Madhavan also consider the effects of deviation from idealized helical geometry, including both migration and microbuckling effects [47]. Migration is considered in the outermost radial positions of the filaments within the yarn. Since the filament path is much greater than that of the average yarn, it is proposed that some of these outer filaments will migrate inward towards the core of the yarn. Microbuckling is considered within the core region, where these filaments with the shortest path will buckle to compensate for the additional length of these filaments. Naik and Madhavan consider cases up to 1.5% migration and 0.6% microbuckling based on the predicted size of the respective migration and microbuckling zones. In practice these would have to be determined through direct measurements. The effects of these parameters on the overall elastic properties is minimal and will not be considered here. Table 4-1 provides a brief summary of the yarn models discussed.

Table 4-1: Summary of twisted yarn models

Author	**Model details**	**Variables**
Gegauff [48]	$\cos^2\theta$ geometry	E_f (longitudinal filament modulus) and θ (surface twist angle)
White [49]	$\cos^2\theta$ with interfilament friction	
Rao and Farris [44]	$\cos^2\theta$ with stiffness rotation	E_f, θ, and d (anisotropic ratio)
Naik and Madhavan [47]	$\cos^2\theta$ with stiffness rotation, migration and microbuckling effects	

Baets et al. [50] also compare these models, as well as an additional elliptical cross-section adjustment to the Naik model. For yarns with low twist (<10º) the difference between the Gegauff and White models and between the Rao and Naik models, respectively, is negligible.

4.2.2 Objectives

The purpose of this paper is to investigate and compare the effects of yarn twist on the bulk properties of dry textile yarns, using both a traditional synthetic high performance para-aramid fiber yarn (Kevlar 49) and a regenerated cellulose fiber yarns (BioMid). The results will then be compared to the Gegauff $\cos^2\theta$ (4-1) and Rao and Farris twist models (4-2) to verify the applicability of these models in predicting yarn modulus for both materials. These two models were chosen as they can be applied without the need for additional properties, such as interfilament friction, as in the White model, and rely only on the elastic properties of the yarn. The degree of twist used will be relatively low, well below the point at which twist is expected to decrease the breaking tenacity of the yarn.

4.3 Methods

4.3.1 Materials

Two materials were select to assess differences in behavior and the performance of the proposed model, Kevlar 49 and BioMid. Kevlar 49 is the commercial name of a synthetic para-aramid yarn manufactured by DuPont [91]. It has been used in a variety of high-performance applications, as it features excellent strength-to-weight characteristics, including high chord modulus, high strength, and low elongation at break.

BioMid is a continuous 100% cellulose yarn that is composed of by-products from the lumber industry. BioMid is derived by separating the cellulose, dissolving into a pulp and then spinning it in order to produce a continuous fiber, rather than being produced in a viscose process like other regenerated cellulose fibers [107]. As it is composed of lumber by-products, it is proposed as a sustainable and more environmentally friendly alternative for other synthetic multifilament yarns, such as E-glass or Kevlar.

The aramid yarns tested were Kevlar 49 Para-Aramid yarns (DuPont, Richmond VA, USA) with 380 denier, while the regenerated cellulose fibers were BioMid Cellulose Fibers (GS Consulting, Burnaby BC, Canada) with 1650 denier yarns. Manufacturer provided values are summarized in

Table 4-2.

Table 4-2: Summary of manufacturer values for Kevlar 49 and BioMid yarns [91]

	Kevlar 49	BioMid
Denier (den)	380	1650
Filament diameter (micron)	12	11
Filament count	256	900
Elongation at break (%)	2.4	4.5
Tenacity (gf/den)	23.6	8.5
Modulus (gf/den)	885	315

Aramid and regenerated cellulose yarns can be manufactured into textiles with zero-twist, as each of their respective manufacturing processes allows for the production of continuous filaments. However, standards dictate the testing of both of these yarns be performed with a certain level of twist to avoid high variability between results [2-3].

Yarns were tested at three different twist levels: zero twist, 80 turns per meter (tpm), and at a third point, depending on each fiber type. 80 tpm was the standard used by each manufacturer, from which a comparison could be made to provide values for breaking strength, strain, and elastic modulus. The third test point for each was determined by comparing the surface twist angle for each sample. Since the BioMid contained a significantly higher count of fibers, the effective twist angle at 80 tpm was much higher than the Kevlar 49, thus the third point for the BioMid fibers was taken at 40 tpm and for Kevlar 49 at 160 tpm. This resulted in three different twist angles tested of roughly 0º, 2.5º, and 5º. Actual twist angles were determined by yarn geometry, which has been shown to be a valid method to estimating the surface angle [31].

4.3.2 Static testing

Two different standards are applicable to static testing, ASTM D885 (for cellulose fibers) and ASTM D7269 (for aramid fibers). Where possible, aspects of the testing that fit both standards were chosen, such as sample length and crosshead travel rates. All yarns were tested at a gage length of 500 mm with a crosshead travel rate of 100 mm/min. A minimum of 10 samples were collected for each yarn and twist combination. Custom yarn grips were used as shown in Figure 4-2, where the yarn is wrapped 180° around the pulley surface prior to clamping. This approach is suggested by ASTM7269 and reduces the load observed at the grip interface.

The testing machine used was a constant rate of extension tensile frame (MTS Synergie 400, MTS, Eden Prairie, MN, USA.), and the manufacturer provided software was used for machine control and data acquisition (TestWorks 4, MTS). Load data was captured via the 500 N uniaxial load cell (MTS) while extension data was captured via the tensile frame positioning. Data was then processed in Matlab (Matlab 2017a, MathWorks).

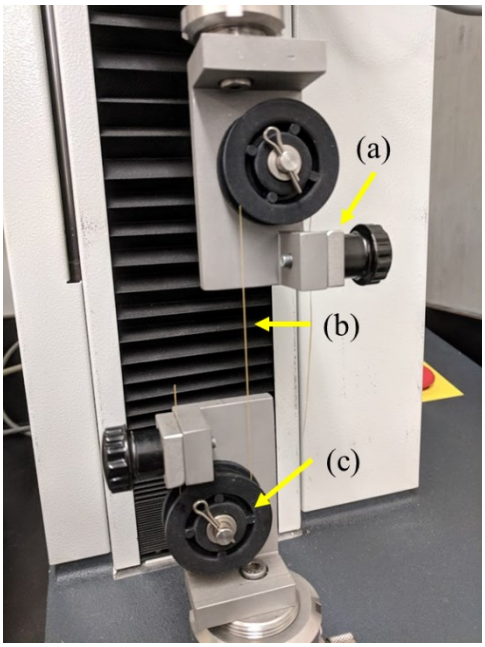

Figure 4-2. Image of testing setup with (a) test grips, (b) loaded sample, and (c) pulleys.

Samples were handled with gloves to avoid contamination and individually loaded into the tensile frame with care taken to preserve filament count and desired twist. Twist was manually inserted by inserting turns over the 500 mm sample length, and always in the Z-twist direction. Small amounts of rosin (Hidersine Violin Rosin) were used on the grips to improve grip strength without overly compressing the yarn ends. As per the referenced standards, samples that broke within 10 mm of the grips were discarded to ensure failure was not initiated by stress concentrations at the grip faces.

4.3.3 Data processing and analysis

For each sample, chord modulus, breaking tenacity and elongation at break were determined. Chord modulus for each sample was determined by (4-3) [103] where $F_{x\%}$ and $\varepsilon_{x\%}$ represent the force and extension at $x\%$ of the maximum breaking force, respectively.

$$CM = \frac{F_{20\%} - F_{15\%}}{\varepsilon_{20\%} - \varepsilon_{15\%}} \quad \textbf{(4-3)}$$

The breaking tenacity was determined from the maximum achieved load during testing, and the elongation at break was the corresponding strain at the point of maximum load.

Each value was then averaged over the ten samples, with the mean and standard deviation reported for each. The significance of each factor was determined by using a one-way ANOVA between the three twist levels as well as a follow-up Tukey HSD in order to determine the significance at $\alpha = 0.05$ between twist levels.

It was noted that the BioMid yarns tended to have a bilinear elastic curve, as shown in Figure 4-3. To provide a metric for this, each curve was separated into two distinct linear regions. The transition point, the strain that best separated the two linear regions, was determined by finding the best linear fit for both regions. The intersection of the two best fit lines was then reported as the transition point.

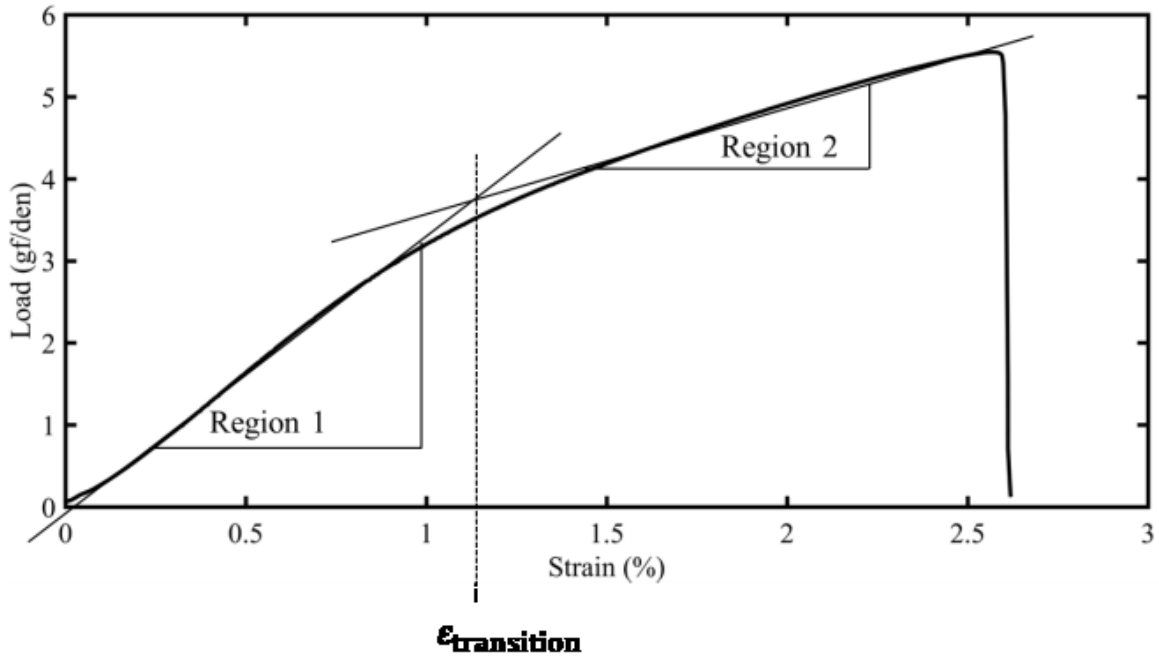

Figure 4-3: Plot showing transition point based on bilinear response (BioMid samples only). The transition point ($\varepsilon_{transition}$) corresponds to the intersection of the linear approximation of each section of the load-deformation curve.

4.3.4 Model comparison

The Rao and Farris model requires a curve fitting be performed in order to determine the anisotropic ratio d. This was done through the minimization of the standard error of the regression as determined by the model and data. By evaluating the models in this manner, the

error could be determined and used to evaluate the quality of the model fit. A standard linear regression was also performed on the mean stiffness values at each twist level to determine the coefficients of a linear model.

4.3.5 Curve fitting

The anisotropic ratio for Kevlar 49 is reported as $d = 17.8$ by Rao and Farris [44]. This anisotropic ratio is found through curve fitting and there is no equivalent directly measurable value found in the literature for this particular preparation of cellulose yarns. Gindl et al. [108] investigate the anisotropic behaviour of other regenerated cellulose fiber types, but not specifically the non-viscose method of preparing BioMid fibers. As well, it has yet to be determined how well the value obtained from this curve fitting method reflects the actual anisotropic performance of the yarns.

A custom curve fitting algorithm was used to determine the anisotropic ratio d. Rao and Farris' model (Equation (4-2) was used to calculate a predicted response based on an assumed value of d, then evaluated against experimental data using the standard error of the estimate. A simple region search optimization was performed over a set of viable d values to minimize the error output.

4.4 Results

4.4.1 Static testing

The chord modulus, breaking tenacity, elongation at break, and transition strain were each determined for each individual specimen. The results were then averaged for each specimen type. For each sample set, a one-way ANOVA was done between each level of twist within each fiber type (Kevlar or BioMid) to ensure the differences between groupings seen were significant, tested at a level of $\alpha = 0.05$. All of the chord moduli discussed here are taken from the 15% to 20% failure strain region of each sample. For the BioMid samples, this is the first elastic region prior to the transition point. Figure 4-4 provides representative load-extension curves for both yarn types. Note the difference in elastic behaviour between the two materials used, specifically the presence of the transition point for the BioMid yarns. This behaviour was consistent at all levels of twist tested.

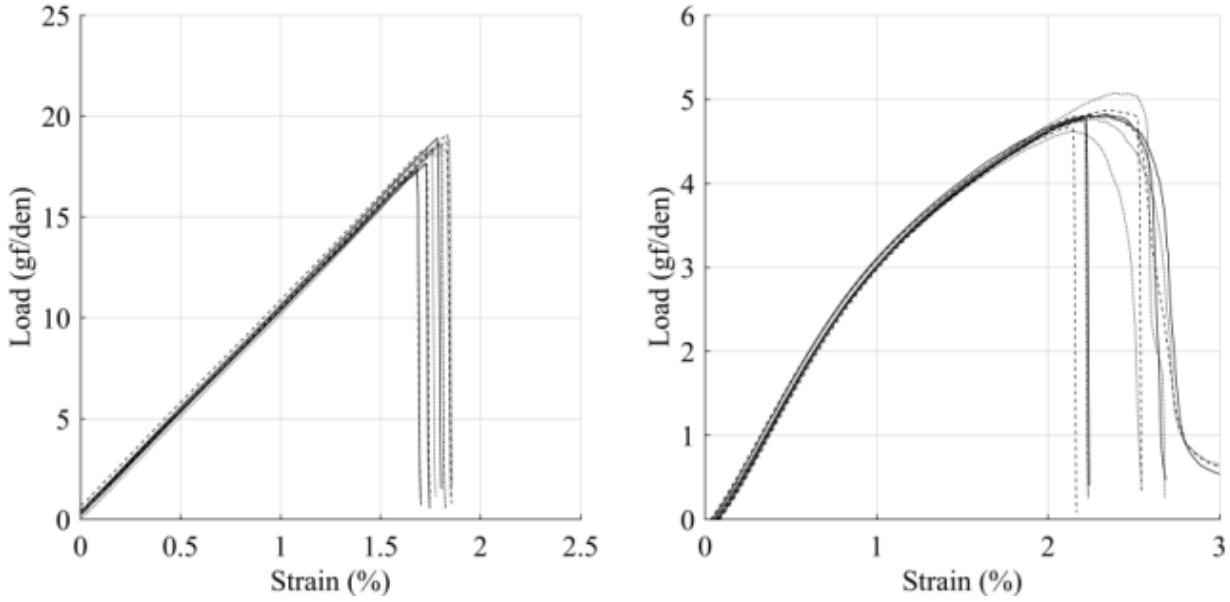

(a) (b)

Figure 4-4: Representative load-extension curves for (a) Kevlar 49 and (b) BioMid yarn specimens

The Kevlar 49 yarns exhibited a linear response up to failure, as can be seen in Figure 4-4a. Breaking tenacity and elongation at break increased with additional twist as summarized in Table 4-3.

Table 4-3. Summary of properties from tested Kevlar 49 yarns. Statistical significance between groupings (α<0.05) is denoted as follows: * between 0 and 80 tpm, † between 80 and 160 tpm, and ‡ between 0 and 160 tpm.

	380den Kevlar 49		
Twist [tpm]	0	80	160
Chord modulus [gf/den]*†‡	1041 ± 6	1017 ± 24	1001 ± 14
Breaking tenacity [gf/den]*†‡	18.3 ± 0.6	21.3 ± 0.6	21.2 ± 0.8
Elongation at break [%]‡	1.77 ± 0.06	2.05 ± 0.04	2.15 ± 0.08

The BioMid yarns did not exhibit a linear response as the Kevlar yarns did, as can be seen in Figure 4b. For these specimens, the effect of twist is not significant between the medium and high levels of twist on the breaking tenacity of the yarn, nor was it significant in the elongation at break or transition point between the low and medium twist levels, as shown in Table 4-4. The overall effect of twist is significant.

Table 4-4. Summary of properties from tested BioMid yarns. Statistical significance between groupings (α<0.05) is denoted as follows: * between 0 and 40 tpm, † between 0 and 80 tpm, and ‡ between 40 and 80 tpm.

	1650 den BioMid		
Twist [tpm]	0	40	80
Chord modulus [gf/den]*†‡	367 ± 10	348 ± 6	332 ± 6
Breaking tenacity [gf/den]*†	4.8 ± 0.1	5.2 ± 0.3	5.4 ± 0.1
Elongation at break [%]†‡	2.3 ± 0.1	2.3 ± 0.2	2.6 ± 0.1
Strain transition point [%]†‡	1.11 ± 0.07	1.11 ± 0.03	1.24 ± 0.05

The significance of twist was determined between the three different groupings. Note that between the untwisted (0 tpm) and twisted (80 tpm and 160 tpm) samples there is a significant difference in all categories, but not between the 80 tpm and 160 tpm groupings.

4.4.2 Testing of curve fit algorithm

The curve fitting was tested with two different inputs to test the sensitivity of the algorithm to the data provided. First, the entire range of available data was used, typically seven unique data points, to obtain the curve fit over the whole range of data, denoted here by d'. Next, the same curve fitting algorithm was performed for only the first three data points, which were the three data points within the 5° region of interest for this study. This fit parameter was denoted by d'_{low}. This provides an insight to whether or not the additional curve fitting points are necessary in order to achieve a reasonable value for the so-called anisotropic ratio as reported by Rao and Farris and shown in Table 4-5.

Table 4-5: Comparison of anisotropic ratio.

Material	d **(reported by Rao and Farris** [44]**)**	d' **(curve fit over entire data set)**	d'_{low} **(curve fit over first three points)**
Kevlar 29	9.9	9.5	10.8
Kevlar 49	17.8	17.6	16.2
Kevlar 149	16	14.0	15.1

Note that the curve fitting algorithm developed agrees relatively well with those as reported by Rao and Farris, and can be used with confidence in determining the anisotropic ratio from new data. The difference between the anisotropic ratios calculated using the entire data set versus

those only within the range of interest is negligible, and thus only three data points can be used to determine the anisotropic ratio. Figure 4-5 shows the sensitivity of the model to the deviation in the anisotropic ratio. It is important to notice that all values are within reasonable agreement of the behaviour of the yarn, and increasing values of the anisotropic ratio result in greater twist impact on chord modulus.

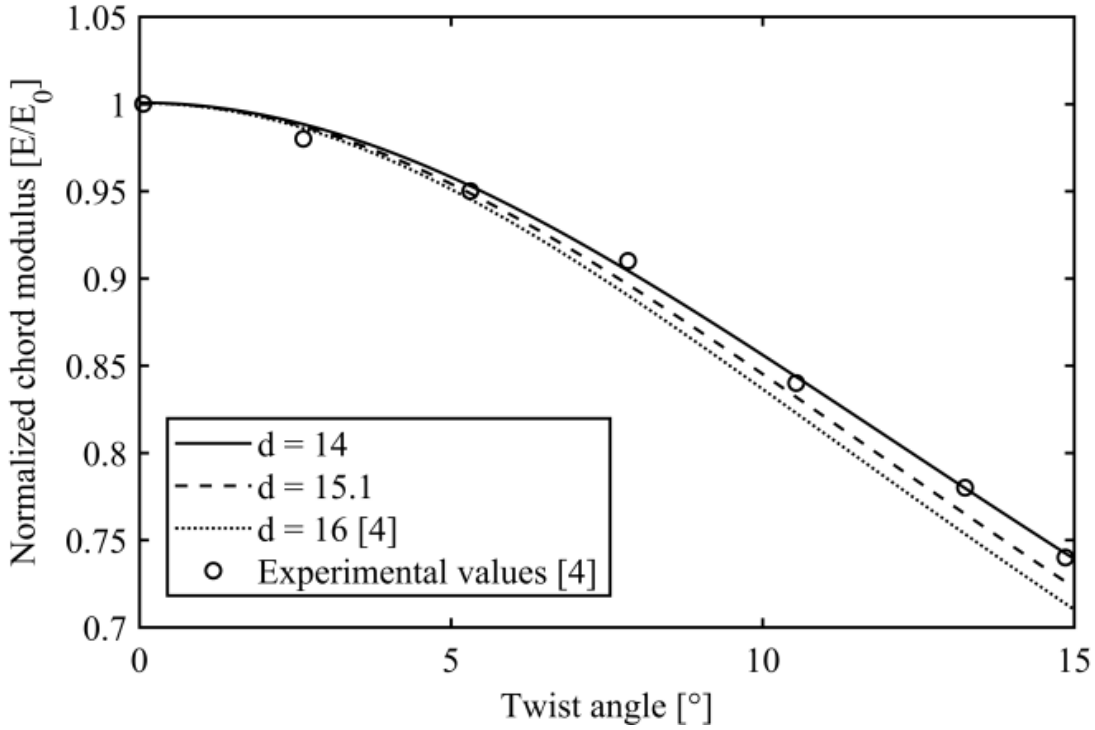

Figure 4-5: Plot of curve fitting for Kevlar 149 compared against reported values by Rao and Farris [44]**.**

Both Gegauff's $\cos^2\theta$ model (Equation (4-1) and Rao and Farris' stiffness model (Equation (4-2) were used in an attempt to model the effects of twist on the stiffness of the yarns. In general, it appears that Gegauff's model overestimates the longitudinal modulus of the twisted yarns at low angles of twist; that is, this model underestimates the impact yarn twist has on predicting longitudinal modulus. Rao and Farris' model, which accounts for the entire rotation of the stiffness matrix, performs slightly better, though does not seem to accurately capture the trend in this range. However, as discussed previously, this low twist range is actually the most relevant as only small amounts of twist are required for processing and higher ranges are increasingly detrimental to strength and stiffness of the yarns.

4.4.3 Twist models

The predicted response for each set of samples tested is calculated based on both the $\cos^2\theta$ model (Equation (4-1) and the Rao and Farris model (Equation (4-2). As well, each set of data was also subject to a linear regression in addition to the aforementioned twist models. This regression was modeled as shown in (4-4), where β_0 is the y-intercept and β_1 is the slope.

$$E_f = \beta_0 + \beta_1\theta \quad \textbf{(4-4)}$$

Note that these regressions were performed without normalization to the zero twist results. Here, the p-value is used to indicate the significance of each coefficient. For the Kevlar 29 380 denier samples $\beta_0 = 1039 \pm 3$ MPa and the stiffness decreased by $\beta_1 = -7.3 \pm 0.7$ MPa for each degree of twist. A summary of the regression results is shown in Table 4-6.

Table 4-6: Regression results for Kevlar 49 samples

	Coefficient	Standard Error	p-value
Intercept β_0	1039.38	2.60	0.002
Angle of twist β_1	-7.25	0.73	0.064

For the BioMid samples, $\beta_0 = 367 \pm 1$ MPa and the stiffness decreased by $\beta_1 = -7.0 \pm 0.4$ MPa for each degree of twist. The results of the regression for these samples are shown in Table 4-7.

Table 4-7: Regression results for BioMid samples

	Coefficient	Standard Error	p-value
Intercept β_0	366.59	1.37	0.002
Angle of twist β_1	-7.03	0.42	0.038

Both sets of samples had an $R^2 > 0.99$, which shows a good adherence to the linear model for this range of twist.

4.4.4 Modeled versus experimental results

The experimental results for each of the three tested twist levels are plotted against each of the three models ($\cos^2\theta$, Rao and Farris model, and the linear regression). Two of the Rao and Farris model are provided for the Kevlar 49 samples, using both the anisotropic ratio provided by Rao and Farris as well as the one determined in this study. An anisotropic ratio of $d = 11.6$ was

found to minimize the error of the regression for Kevlar 49, and the plot of the models and experimental results are provided in Figure 4-6.

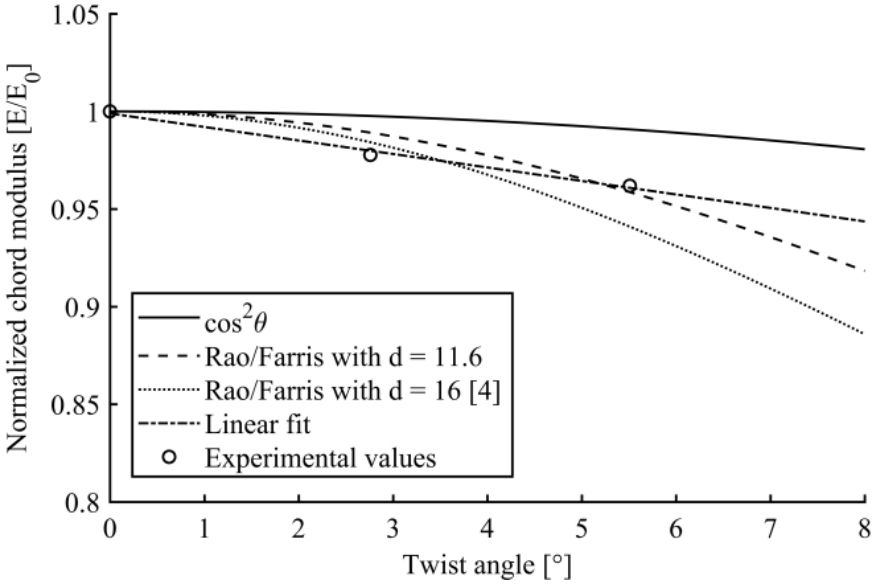

Figure 4-6: Plot of Kevlar 49 experimental chord moduli vs. twist models, normalized with respect to the untwisted modulus.

Similarly, an anisotropic ratio of $d = 33.2$ was determined to minimize the standard error of the regression for the BioMid samples. The resulting fit is shown in Figure 4-7.

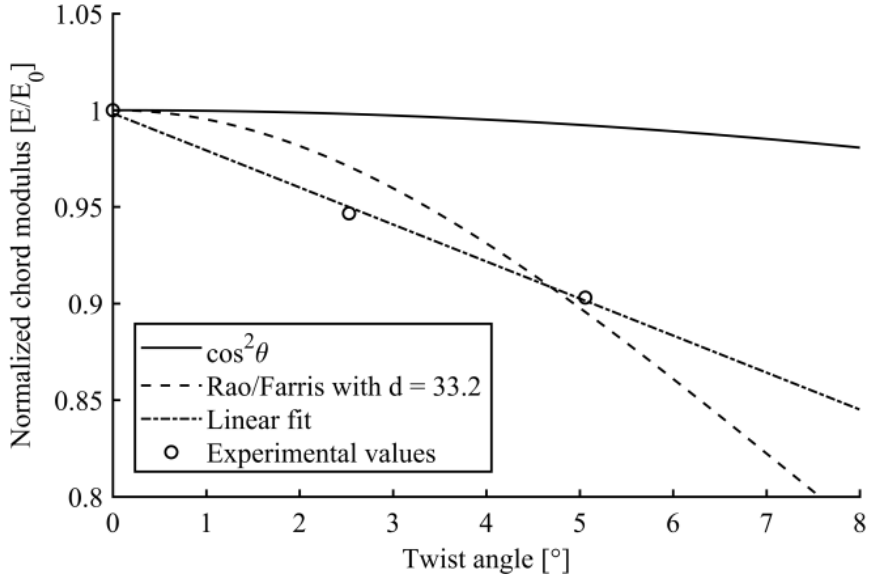

Figure 4-7: Plot of BioMid experimental chord moduli vs. twist models, normalized with respect to the untwisted modulus

The decrease in stiffness due to twist at this range for the BioMid samples is significant. Again, the $\cos^2\theta$ model is insensitive to twist, and the Rao and Farris model requires quite a high

anisotropic ratio in order to capture the behaviour in this range. However, whether or not this accurately reflects the characteristics of BioMid is to be determined.

4.5 Discussion

The goals of this paper were to first compare the mechanical performance of BioMid yarns to Kevlar 49 yarns, as well as to determine the effect of twist on the stiffness and strength of each sample and compare their behaviour to existing twisted yarn stiffness prediction models.

4.5.1 Impact of twist

The addition of yarn twist affects dry yarns in a number of ways. As seen in other studies [44], [72],[71], the inclusion of low amounts of surface twist (below 6 degrees as tested here) may reduce the longitudinal yarn modulus, but can also increase yarn strength and elongation at failure. This was true for both the Kevlar and BioMid yarns. For the regenerated cellulose BioMid yarns, the transition point of the bilinear curve is also shifted higher with a greater angle of twist.

4.5.2 Modeling

The $\cos^2\theta$ model does a poor job of predicting elastic performance in yarns with low levels of twist. The Rao and Farris model predicts the elastic response more accurately at higher twist levels, but does not capture the behaviour at lower twist levels. As well, the "anisotropic ratio" parameter is only determined through curve-fitting and is limited to use with high-performance fibers with a ratio greater than 10 [44]. The linear regression performed for each set of samples yields the highest quality fit for the low twist region of interest.

4.5.3 Comparison of yarn material

The regenerated cellulose BioMid yarns and the para-aramid Kevlar 49 yarns are quite different in terms of their mechanical performance. First, the normalized response stiffness and strength of BioMid decreases much faster with response to twist than that of Kevlar 49. However, the failure strain of BioMid is higher than that of Kevlar. Additionally, while Kevlar 49 has a very linear elastic response right up to failure, the BioMid yarns exhibit a bilinear response where the stiffness decreases upwards of 1% strain. According to Graupner et al., cellulosic fibres can exhibit varying levels of ductility based on the resource of origin (such as wood or plant fiber)

and consequently the manufactured yarn properties reflect that of the original chemical composition and cell wall structure [109].

For potential use of BioMid as a composite material, the 'knee' point is one that requires particular attention. At the outset, it may seem as a negative component to its performance, as compared to the completely linear response to failure of Kevlar 49. However, there are some benefits to such behaviour. Though not as strong as Kevlar 49, the extension to failure is greater. This gives BioMid a semi-ductile response, albeit without a necking region. This increased ductility could be utilized in applications where visual indications are relied on for inspection purposes, such as in composite rebar. Once again, the linear regression is appropriate here for predicting the stiffness response within the low twist region, and performs much better than the Rao and Farris model, especially given that the value determined for the so-called anisotropic ratio cannot be rationalized in this instance nor is it backed by any available literature, as the original study was limited to certain continuous synthetic yarns.

4.6 Conclusions

Dry textile yarns made from a para-aramid (Kevlar 49) and from regenerated cellulose (BioMid) were tested in tension under varying levels of yarn twist. Chord modulus, breaking tenacity, and elongation at failure were determined for each sample. Low levels of twist have a significant impact on mechanical performance of textile yarns. Existing models, including the $\cos^2\theta$ model and the Rao and Farris model, are poor predictors of stiffness response to twist in low twist applications, and a linear model is better suited to the response and should be further explored for application. Further work is required to generalize this equation for all yarn types and to develop a physical justification for its use.

Chapter 5 Tensile testing of twisted composite strands

5.1 Introduction

In Chapter 2, the effect of low levels of twist on the mechanical performance of two continuous multifilament yarns were compared. In general, the elastic modulus decreased while both yield strength and yield stress increased in response to added twist. Building on these findings, the objective of this study is to investigate the effect of low twist on composite yarn strands and compare the response to twist to that of dry textile yarns as determined in previous work.

A previous work by Weinberg and Schwartz investigated the effect of twist on Kevlar 29 yarns and composite strands. Here, a similar approach is taken but the effect will be explored as in Chapter 2 with Kevlar 49 and BioMid textile. Composite strands are manufactured out of these yarns at three distinct twist levels, and tensile tests performed on these samples to determine the elastic modulus, breaking strength, and breaking strain over the low twist region. It is determined that the addition of twist in composite strands plays a different role than twist in a dry textile yarn. Whereas in a dry textile yarns the twist acts as a binder for the individual yarn filaments, this role is redundant in the presence of a composite matrix, and the impact of twist is not as prevalent.

5.2 Background

Twist is often added to textile yarns as a means of improving handling and strength [3]. For a continuous multifilament yarn, handling is improved by improving the cohesion between yarn filaments, by creating binding interfilament pressure. Individual filaments do not stray from the yarn path since the twist acts to bring the filaments together. In terms of strength, filament load sharing is increased and twisted yarns tend to fail with a sudden localized failure, rather than progressive individual failure of single filaments [110]. This effect is realized up to an optimal twist angle, typically around or below 10 degrees. Beyond this point the loss of longitudinal reinforcement due to the increase in fiber obliquity overshadows any gains from the interfilament friction effects [49]. The increase in fiber obliquity also has a negative effect on the stiffness of these yarns. Over large angles of twist the decrease in stiffness roughly follows a monotonically decreasing response of $\cos^2\theta$, but for low levels of twist such an approximation is not appropriate as was demonstrated in Chapter 3.

5.2.1 Stiffness prediction of twisted composites

Unidirectional composites are often the building block for developing more complex composite models. For a unidirectional composite strand, the basic isostrain micromechanical model is sufficient for predicting longitudinal modulus [6]. Here, the untwisted composite strand can be treated as a unidirectional composite lamina as shown in Figure 5-1.

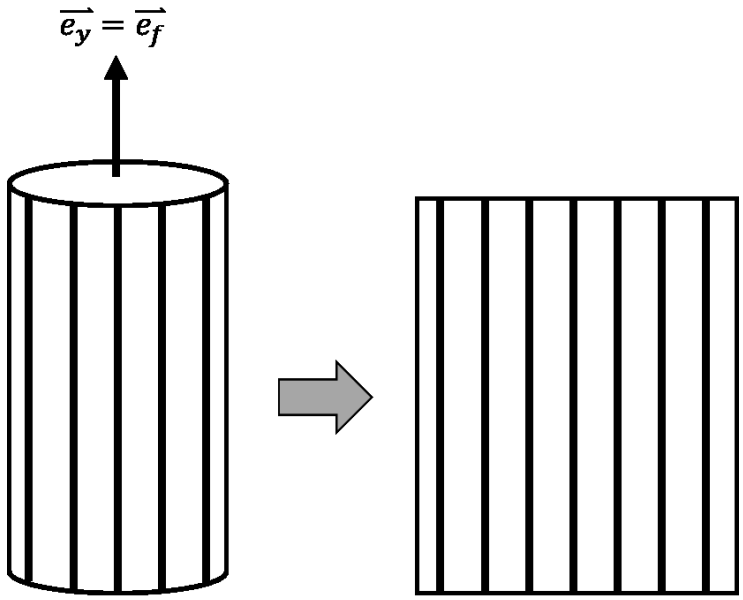

Figure 5-1: Schematic of an untwisted unidirectional composite strand. The unwrapped filament layer can be treated as a unidirectional composite lamina.

When the reinforcing components are aligned with the direction of load, the composite is assumed to be in a case of isostrain; that is, the deformation experienced across the composite is the same, as discussed in section 2.2 of Chapter 2. For a straight, untwisted composite strand, the stiffness can reasonably be predicted by (5-1), where E_y is the elastic modulus of the yarn and $E_f, E_m, V_f,$ and V_m are the modulus and volume fraction of the fiber and matrix constituents, respectively.

$$E_y = E_f V_f + E_m V_m \tag{5-1}$$

This isostrain model represents the upper limit of the stiffness model for the mechanics of materials approach. The lower limit of the mechanics of materials approach is the isostress model, shown in (5-2), which is commonly used to represent the transverse modulus of a unidirectional laminate.

$$\frac{1}{E_y} = \frac{V_f}{E_f} + \frac{V_m}{E_m} \tag{5-2}$$

The twisted composite strand is between the limiting isostress and isostrain cases, as shown in Figure 5-2.

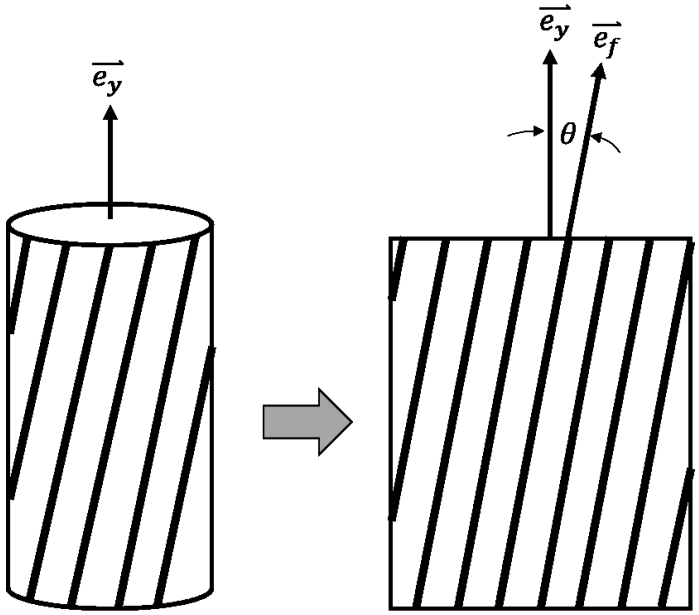

Figure 5-2: Schematic of an twisted unidirectional composite strand. The unwrapped filament layer can be treated as a off-axis composite lamina.

Between these two limiting cases, the compliance matrix must be used to account for obliquity with respect to the longitudinal direction. Only the tensile response and thus the $\bar{S}_{11}$ term is required provided in (5-3).

$$\bar{S}_{11} = S_{11}\cos^4\theta + (2S_{12} + S_{66})\sin^2\theta\cos^2\theta + S_{22}\sin^4\theta \quad \textbf{(5-3)}$$

In the case of a twisted composite strand (5-3) is representative of a single filament layer at an angle θ and does not account for the change in twist with respect to the radial position of the filaments. However, what should be noted here is that for a composite material, (5-3) is maximum at $\theta = 0$ and the equation is monotonically decreasing for increasing twist angle.

5.2.2 Strength prediction of twisted composites

According to Naik the addition of twist is expected to increase the strength of the composite strand through an increase in lateral pressure within the yarn [53]. It is suggested that twisted strands will improve the strength of the overall composite as the twist increases the lateral pressure within the yarn and thereby also increases the interfacial shear strength of the filaments, improving overall strength of the composite strand. This is assumed to be the case for all fiber composites, not just unidirectional composite strands. The increased interfacial shear strength decreases the cumulative effects of broken filament strands throughout the composite structure. Naik and Madhavan [47] have developed a model to predict the elastic behaviour of twisted impregnated yarns, including filament microbuckling and filament migration. These both consider potential deviations from the idealized helix geometry, and migration, specifically, with the reduction in strain in outer layers of a twisted yarn. Rather than assuming each filament is uniquely constrained to a radial distance from the centre of the yarn, the filament 'migrates' towards the centre of the yarn, reducing the strain on that filament. This is averaged over a portion of the yarn in their model.

The upper limit of this effect is due to the fiber obliquity of the outermost filaments and prestraining that may occur due to the helical structure of the braid. Even though the lateral pressure of the internal filaments is still increased by the addition of twist, the outermost filaments are inclined at such an angle that it is the interface and not the reinforcing strands themselves that governs failure.

5.3 Methods

The methodology in this study is similar to that described in Chapter 3 with the exception of testing composite strands rather than dry textile yarns.

5.3.1 Material properties

Two different types of composite yarn strands were manufactured for these experiments. The first was a aramid fiber (380 denier Kevlar 49, DuPont) and a two-part thermoset epoxy (Epon 826 / Lindau LS-81K) previously used in textile composites manufacture [62]. Additionally, strands were also manufactured from a regenerated cellulose fiber (1650 denier BioMid) and a bio-based two-part thermoset epoxy (Ecopoxy). Critical manufacturer properties for the purpose of predicting elastic modulus are provided in the table below.

Table 5-1: Properties of yarn composite constituents.

Yarn material	Kevlar 49	BioMid
Denier (den)	380	1650
Tensile modulus (g/d)	885	315
Tensile modulus (GPa)	112.4	42
Breaking tenacity (g/d)	23.6	8.5
Elongation at break (%)	2.4	4.5

Table 5-2: Properties of matrix constituents.

Resin	Hardener	Mix ratio	Tensile modulus [GPa]	Cure profile [hrs/°C]
Epon 826	Lindau LS-81k	1:1	2.7 GPa	1.5/66, 1/85, 3/150
Ecopoxy Part A	Ecopoxy Part B	3:1	2.7 GPa	48/21

5.3.2 Specimen preparation

All specimens were prepared in-house from dry textile yarns off supplier creels. Figure 5-3 provides a schematic of the steps involved in preparation.

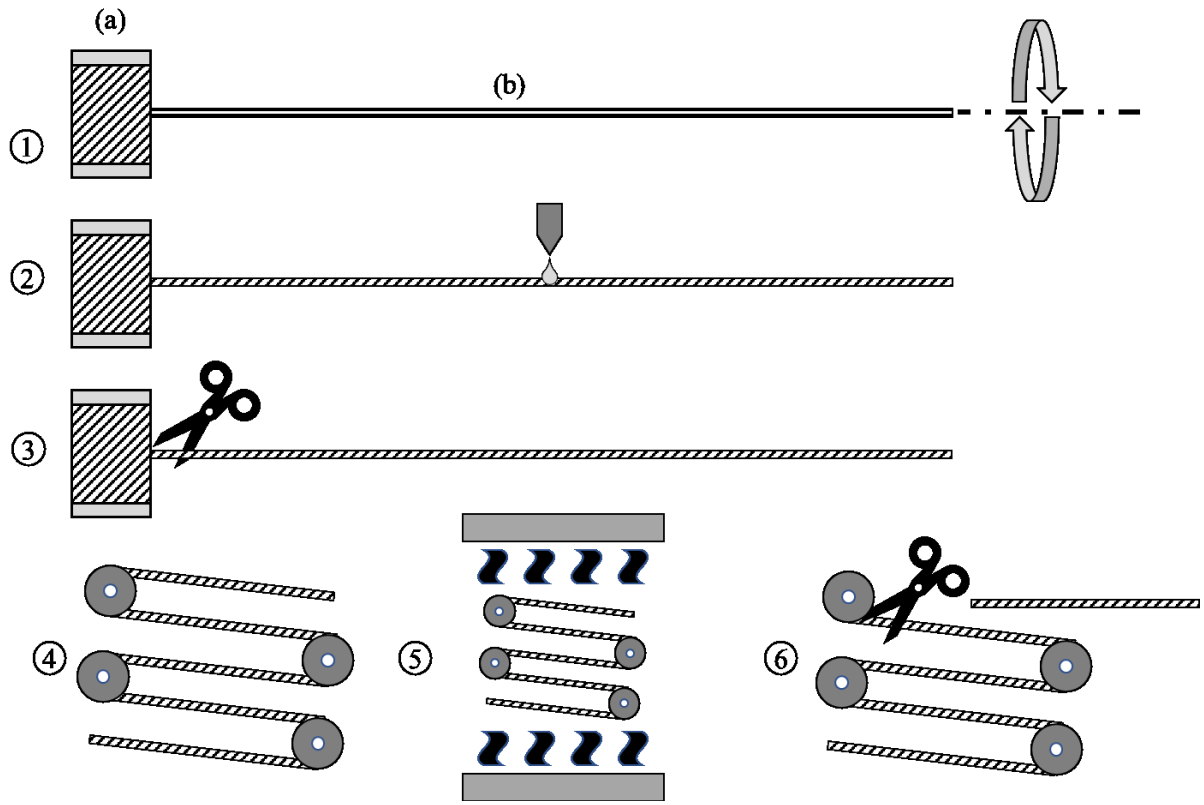

Figure 5-3: Schematic of specimen preparation for unidirectional composite strands, where (a) is the creel of untwisted yarn and (b) is the length of yarn extracted for preparation.

Lengths of yarn approximately 2.5 – 3 m in length were measured off the supplier creel. Next, the yarns were fixed at one end, while twist was applied by rotating the opposing end of the yarn up to the desired level of twist for each sample. Six different types of samples were prepared, including the two different yarn materials and three levels of twist for each, as summarized in Table 5-3.

Table 5-3: Summary of twist combinations tested for composite strands.

	Denier	No twist	Low twist (~2.5°)	High twist (~5°)
Kevlar 49	380	0 tpm	80 tpm	160 tpm
BioMid	1650	0 tpm	40 tpm	80 tpm

Note that even though the number of turns per meter were different for each level of high or low twist, the surface twist was approximately the same. This is due to the difference in filament count and yarn size for each type of yarn.

5.3.3 Resin application and curing

Samples were held in the twisted configuration with constant tension for epoxy resin application. The epoxy resin was then manually applied to the dry yarns, and care was taken to remove as much excess resin as possible during this step. Next, the impregnated yarns were wound onto a custom curing rig that would allow for samples to be cured in straight sections under constant tension as shown in Figure 5-4.

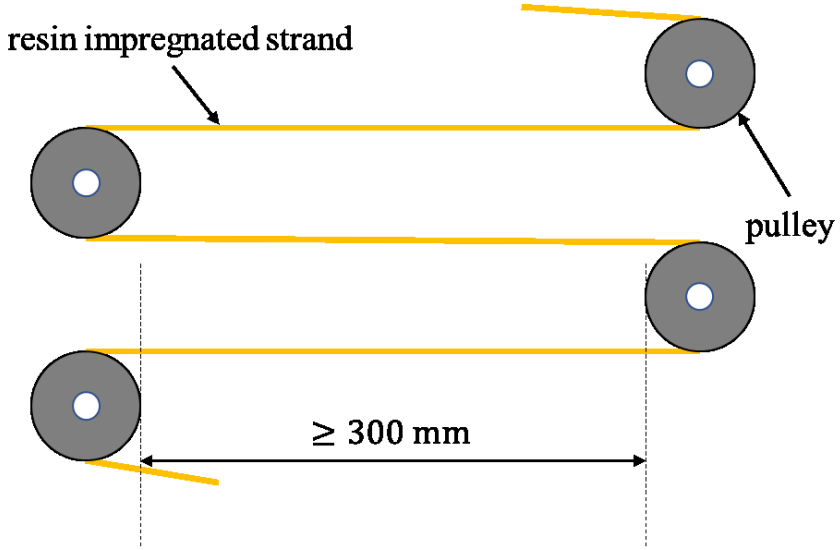

Figure 5-4: Schematic of setup used to cure unidirectional composite strands

A minimum strand length of 300 mm was targeted during preparation. The curing rig ensured tension was maintained to cure straight composite strands. Curing was done according to manufacturer specifications. For the Epon 826/Lindau LS-81K epoxy resins, the 5-hour curing cycle was performed in an oven with a PID controller (Omega) to perform the ramp and hold functions of the temperature cycling. For the Ecopoxy resin, no oven was used as only ambient temperatures were required for curing.

Once cured, individual specimens were cut from the straight sections of the cured yarns and loaded into the same custom textile testing grips as described in Chapter 2.

5.3.4 Tensile testing

As before, tensile testing was done using a constant rate of extension tensile frame (MTS Synergie 400, MTS, Eden Prairie, MN, USA.), and the manufacturer provided software was used for machine control and data acquisition (TestWorks 4, MTS). Data was then processed in Matlab (Matlab 2017a, MathWorks). Ten specimens of each yarn and twist combination were

tested, for a total of 60 specimens across the six different groups, as described previously in Table 5-3. Each specimen was tested to failure under a constant rate of extension of approximately 2 mm/min.

5.3.5 Mechanical properties

Elastic modulus of each individual sample was determined by a linear regression over the data in the 0.25% - 0.3% strain range. Sample data was strain-corrected according to the initial linear modulus such that it passed through the load-strain origin, in order to correct for start-up slack when determining the failure strain. Finally, the tensile strength was determined from the maximum of the load-strain graph.

The yarn cross section was estimated as a function of the linear and material densities as recommended in ASTM D2343 [42]. The results are tabulated in Table 5-4 with the properties taken from the manufacturer specifications.

Table 5-4: Summary of yarn densities and estimated yarn cross-section

Yarn	Denier	Yarn density [g/cm^3]	Area from density estimate [mm^2]
Kevlar 49	380	1.44	0.029
BioMid	1650	1.52	0.120

This yarn cross section was used to determine the elastic modulus and strength for each sample, as recommended in ASTM D2343 [42].

5.4 Results

The elastic modulus, breaking strength, and breaking strain were determined for each sample, and the groupings of each yarn type were then subject to a one-way ANOVA, with a Tukey HSD follow-up test if the differences between each were significant at $\alpha = 0.05$. The results for the Kevlar 49/epoxy samples are tabulated below in Table 5-5.

Table 5-5: Summary of tensile results for Kevlar/epoxy unidirectional composite samples. Statistical significance between groupings (α<0.05) is denoted as follows: * between 0 and 80 tpm, † between 0 and 160 tpm, and ‡ between 80 and 160 tpm.

		Kevlar 49/Epon 826		
Twist	[tpm]	0	80	160
Elastic modulus, †	[GPa]	114 ± 6	116 ± 5	122 ± 4
Tensile strength, *	[GPa]	1.9 ± 0.2	2.2 ± 0.2	2.0 ± 0.3
Breaking Strain, *	[%]	1.6 ± 0.2	1.9 ± 0.2	1.7 ± 0.3

Note that the elastic modulus increased with respect to added twist, and overall there was a significant increase in breaking tenacity between the samples at even the lowest levels.

A summary of results from the BioMid samples is provided in Table 5-6.

Table 5-6: Summary of tensile results for BioMid/epoxy unidirectional composite samples. Statistical significance between groupings (α<0.05) is denoted as follows: * between 0 and 40 tpm, † between 0 and 80 tpm, and ‡ between 40 and 80 tpm.

		BioMid/Ecopoxy		
	Twist [tpm]	0	40	80
Elastic modulus, †‡	[GPa]	34 ± 1	35 ± 1	33 ± 1
Tensile strength, †‡	[GPa]	0.67 ± 0.05	0.68 ± 0.05	0.60 ± 0.04
Breaking strain	[%]	3.1 ± 0.4	3.1 ± 0.4	2.8 ± 0.4

Here as well there is a significant change in elastic modulus across all samples, but note that at the highest twist level the stiffness decreased. Additionally, the tensile strength decreased at the highest level of twist.

5.5 Discussion

From the results above and considering previous studies where dry yarns are tested is that the twist has a much different effect on unidirectional composite strands than it does on dry yarns. With dry yarns, the addition of twist results in a monotonic decrease of stiffness, as shown in

Chapter 2. This is confirmed as well by other studies, such as that by Rao and Farris [44], across multiple different materials and levels of twist. However, with unidirectional composites, the effect can vary and is dependent on the yarn and matrix properties.

5.5.1 Tensile modulus

For Kevlar 49/epoxy composites, there is an increase in stiffness across the range tested, as shown in Figure 5-5. While there was a consistent decrease in stiffness for the dry yarns, there is an increase in stiffness for the composite strands.

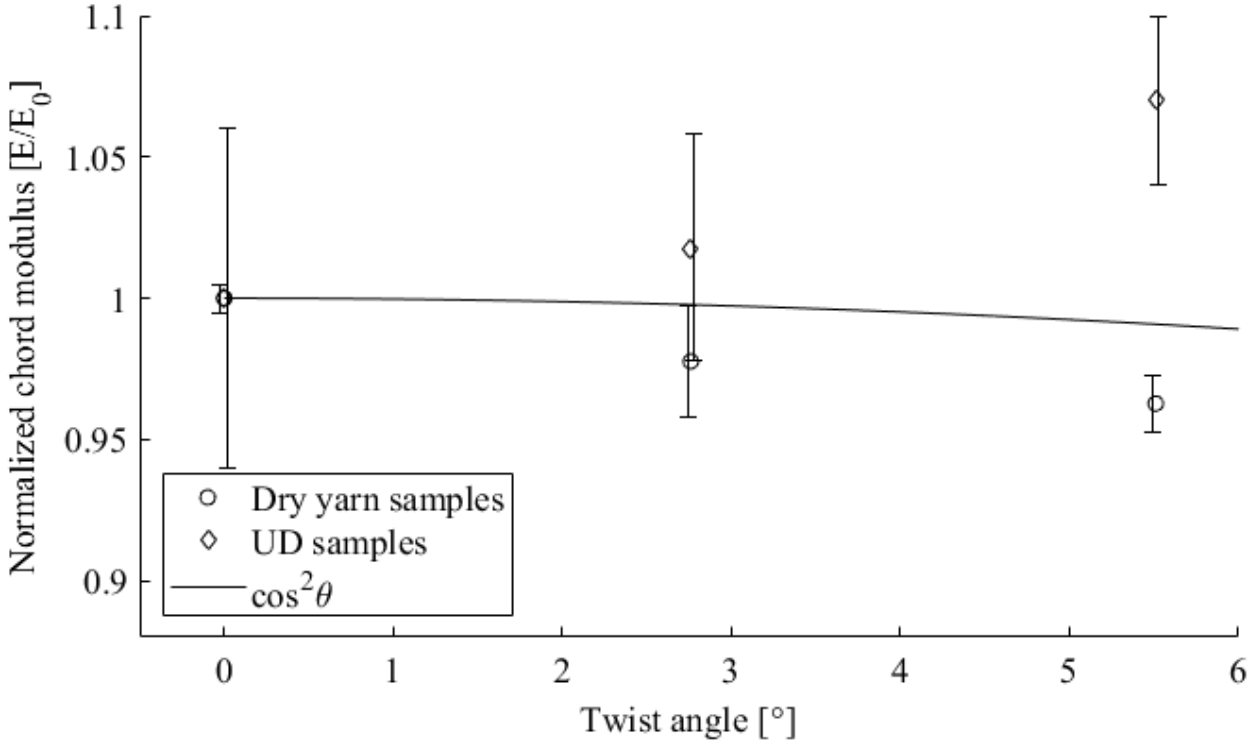

Figure 5-5: Plot of normalized chord modulus versus twist angle for Kevlar 49 dry yarns and composite strands. Samples are normalized with respect to the untwisted modulus for each of the dry yarns or composite strands.

This is also confirmed by the work of Weinberg and Schwartz, who tested the relative performance of Kevlar 29 yarns and Kevlar 29/epoxy composite strands [3]. When comparing the variation of modulus across twist, in the low twist region they have also recorded a slight increase in the strand modulus. The traditional twisted yarn model is not a suitable model for composite strands, especially at these levels of twist.

For the Biomid/ecopoxy samples, the impact of twist on stiffness is minimal across the range tested, as shown in Figure 5-6. Note there is still a slight increase in stiffness for the composite strands over the lowest level of twist, followed by a decrease in stiffness as the twist increases.

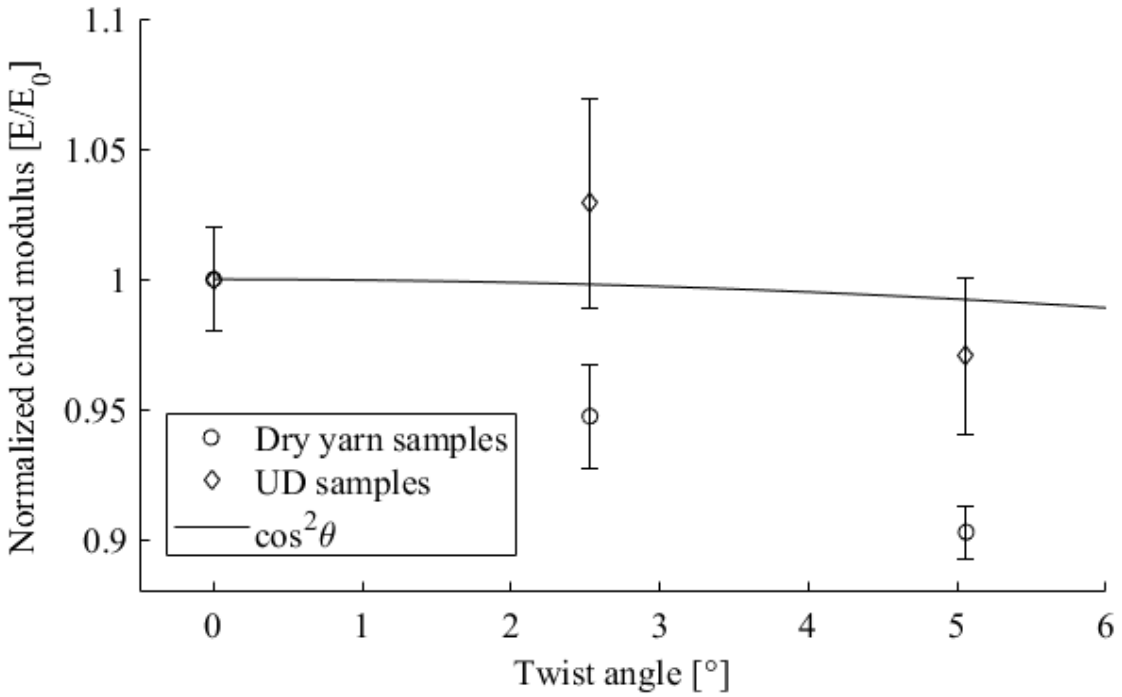

Figure 5-6: Plot of normalized chord modulus versus twist angle for BioMid dry yarns and composite strands. Samples are normalized with respect to the untwisted modulus for each of the dry yarns or composite strands.

It is likely that should these yarns be tested at higher levels of twist, the decrease in stiffness would continue. These higher levels of twist are beyond the scope of this study.

It is not immediately apparent how or why twisted composite strands do not exhibit the same decrease in stiffness as the dry yarns. As shown in section 5.2.1, the expected behaviour for any misalignment with respect to the loading direction is a monotonic decrease in stiffness. However, this is not the case seen with either set of samples. None of the existing models, developed through micromechanics or other approaches, accounts for an increase in stiffness.

One proposition is that in practice an untwisted yarn is not truly straight. Though the filaments in untwisted yarns and composite strands are assumed to be well aligned with each other [2], in practice it has been noted that any handling of the yarns results in some filament misalignment unless the straightness of the yarns is specifically attended to, with a process such as acetone straightening [3]. When testing a dry textile yarn, these filament misalignments in the yarn are overcome as the individual filaments are permitted to slide along each other and straighten along with the application of tension. However, in a composite strand, any filament misalignments

prior to matrix curing will be preserved in the composite structure through due to the polymer matrix.

5.5.2 Tensile strength

In this study, the tensile strength of the composite strands increased with the lowest level of twist tested, but decreased at the upper level of twist. When compared to dry yarn samples, the increase in strength was more noticeable. Again, it is proposed that this is due to the role of twist in either case. In a dry yarn, the twist acts as the binding matrix, holding together the individual filaments and increasing interfilament friction. In a composite strand, this is not the case, as the epoxy instead plays the primary role of the binding matrix. It is reasonable to assume that the interfilament friction due to low amounts of twist in a dry yarn cannot compare to the shear strength of a composite matrix.

5.6 Conclusions

Composite strands composed of Kevlar 49 and BioMid textile yarns were tested for tensile modulus, strength, and failure strain. In Chapter 2 it was shown that yarn twist has a significant effect on the mechanical properties, specifically decreasing the stiffness and increasing the strength. However, here it is shown that when twist is present in a composite strand the impact on stiffness and strength is different or not as pronounced as it is for dry yarns.

It is proposed that this is due to the role that twist plays in a composite strand. In the presence of a true composite matrix, the role of twist as a filament binding agent is reduced. As well, it is proposed that the alignment of filaments within the yarn is actually increased with small amounts of twist, resulting in a small increase in stiffness for low twisted composite strands.

Chapter 6 Manufacture and testing twisted tubular braided composites

6.1 Introduction

Tubular braided composites (TBCs) combine manufacturing technologies from textiles and composites industries. The design of the reinforcing textile structure plays a significant role in the mechanical characteristics of the final composite [87], [92], [96]. Twisted yarns have been shown to exhibit improved strength over untwisted ones, even for continuous multifilament yarns where twist is not necessary for the manufacturing process [3]. In this chapter, a manufacturing process to implement twisted yarns is piloted and the effects on the stiffness and strength properties of TBCs is tested.

6.2 Background

6.2.1 Twist modeling in composites

Twist is used to produce many natural fiber yarns as it acts to bundle together the individual short fibers together into a usable final yarn. However, with advances in materials science, virtually continuous fibers and yarns can now be produced, as is the case with many of the fiber constituents used for textile composite materials, such as polyaramids (DuPont Kevlar ®), E-glass, UHMWPE, and regenerated cellulose fibers. Twist can even be added to these textile yarns to improve handling and strength during textile processing [3].

The effect of twist on yarns, textiles, and composites has been documented on a few different levels. In the case of textile yarns, some of the earliest work on the subject was done by Gegauff, who showed analytically that the relationship between twist angle and longitudinal stiffness of a twisted yarn follows a $\cos^2\theta$ relationship [48]. Fundamentally, increased twist increases the obliquity of the fibers to the loading direction, decreasing the stiffness. This model has been further improved upon to account for other factors such yarn migration and microbuckling but the fundamental monotonic relationship still holds true [47]. Small amounts of twist have been predicted to improve the strength of unidirectional composite yarns within a small range of low twist [53].

For more complex textile composite structures, such as weaves or braids, little work has been done to investigate the effect of twist on the stiffness and strength properties of composite structures. Ma et al. investigated the effect of twisted sisal fiber yarns in composites, but there

are a few key differences that are worth pointing out [66]. First, the yarns used by Ma et al. are composed of raw natural fibers, rather than manufactured in a well-controlled continuous process as the Kevlar and Biomid fibers. Second, the levels of twist are far beyond that (greater than 10°) where any improvement in strength is predicted, due to both the size of the yarns as well as the level of twist. As well, the yarns were formed into a single unidirectional sheet and not a textile structure. Naik and Kuchibhotla analytically predict that low levels of twist can be used to improve the handling of a woven composite without significantly altering the strength of the composite [67]. Xu and Qian have developed a model to predict the stiffnesses of a four-directional braided composite (4DBC) by including the effects of yarn distortion, including yarn twist, but does not account for change in strength and is only compared to three experimental samples [21]. No studies on the impact of twist in TBCs has been documented thus far.

6.2.2 Stiffness modeling of TBCs

Analytical stiffness modeling of TBCs has been primarily based on a multiscale approach, where the stiffness of a subcomponent of the TBC is calculated and then used to determine the overall stiffness of the TBC [11], [96], [111]. These models are limited to the linear elastic region of the TBCs. From these models, the primary predictor of TBC longitudinal stiffness (other than constituent properties) has been found to be the braiding angle. Experimental work has validated these findings [11], [54]. In these studies, the constituents used are continuous multifilament yarns and polymer thermoset resins, while the braids are all manufactured on maypole braiders with relatively low carrier counts (36 or less). These are important distinctions as these findings may not apply to other TBCs manufactured from high carrier counts or singles or plied yarns. If addressed, the effects of twist are assumed negligible in these models.

The purpose of this study is to directly address the gap in the literature between twisted yarns and TBCs. TBCs will be manufactured with many of the same or similar properties as before, but specifically designed to compare the effects of twisted yarns in the structure.

6.3 Method

Manufacture of TBCs was done in-house using the process outlined in Figure 6-1.

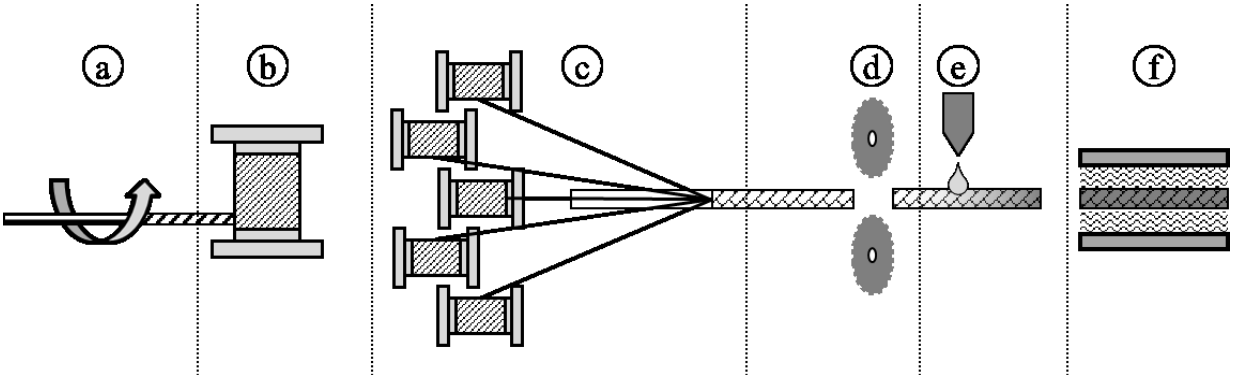

Figure 6-1: Schematic of tested and proposed twisted braided composite process. Continuous multifilament yarns are twisted (a) to 80 tpm and then wound (b) onto braiding bobbins. The spooled yarns are then used to braid (c) preforms and are subsequently cut (d) to length. Resin is impregnated (e) into the braids and finally cured (f) at elevated temperatures.

A detailed description of the manufacturing process for TBCs is provided in section 3.3.4.3.

6.3.1 Constituent materials

Two different textile yarns were used throughout testing. Kevlar 49, a synthetic polyaramid yarn, has been used extensively for various textiles composites applications, including braiding [62]. Kevlar has excellent stiffness and strength properties and is easily handled as well.

BioMid, a regenerated cellulose yarn, is a relatively new material. Similar to other regenerated cellulose fibers, it is manufactured under a proprietary process that claims to use a physical rather than chemical process when compared to other commercial cellulose fibers. It is selected for testing here due to its regional availability (distributed out of British Columbia, Canada) and potential for use as a 'green' textile [54]. Both Kevlar 49 and BioMid yarns are supplied as continuous multifilament yarns.

The matrix provides the interfilament and interyarn support for the composites. A thermosetting epoxy matrix, Epon 826, was used. [2] Epon 826 is an industry standard bisphenol-A thermoset

[2] Initially two different epoxies were to be used during testing, Epon 826 for the Kevlar samples and Ecopoxy for the BioMid samples, as was done in the previous study evaluating the performance of the composite strands. However, during TBC manufacture it was noted that the Ecopoxy did not debond well from the curing mandrels and the added time for curing (approximately 40 hours) significantly slowed production. Samples had to be aggressively handled in order to remove them from the mandrels and compromised the integrity of the samples. Thus, Ecopoxy

epoxy for textile composites and has a well-documented literature base. It is mixed with an appropriate hardener, in this case Lindau LS-81K, at a 1:1 weight ratio. Working life is about 1 hour, which is excellent for handling and preparation purposes. Curing is performed according to a predetermined heating schedule.

6.3.2 Yarn twisting and spooling

Yarns were twisted and loaded onto braider bobbins for the braiding process. Figure 6-2 shows an image of the custom winder/counter used in this process.

Figure 6-2: Images of custom twist winder. The handle (a) is rotated to turn the braider bobbin (b) and twist the yarn (c) about its axis. The analog counter (d) records the number of turns of the braider bobbin.

The operation of the device shown in Figure 6-2 is outlined in Figure 6-3.

A single continuous yarn is drawn from the manufacturer supplied creel and fixed directly to the braider carrier bobbin. The counter is reset to zero. The yarn is then rotated about its primary axis to induce true twist into the yarn but not wind the yarn onto the bobbin (Figure 6-3-1). Once the desired number of revolutions is met, the end of the yarn closest to the supplier creel is cut (Figure 6-3-2) and without allowing the yarn to untwist, wound about the bobbin by rotating it around its primary axis (Figure 6-3-3). Ends were secured with masking tape and spools were marked to indicate the presence and/or direction of twist.

---

was only used for the composite strand study. The effects of this change should be minimal, as both epoxies share similar mechanical characteristics.

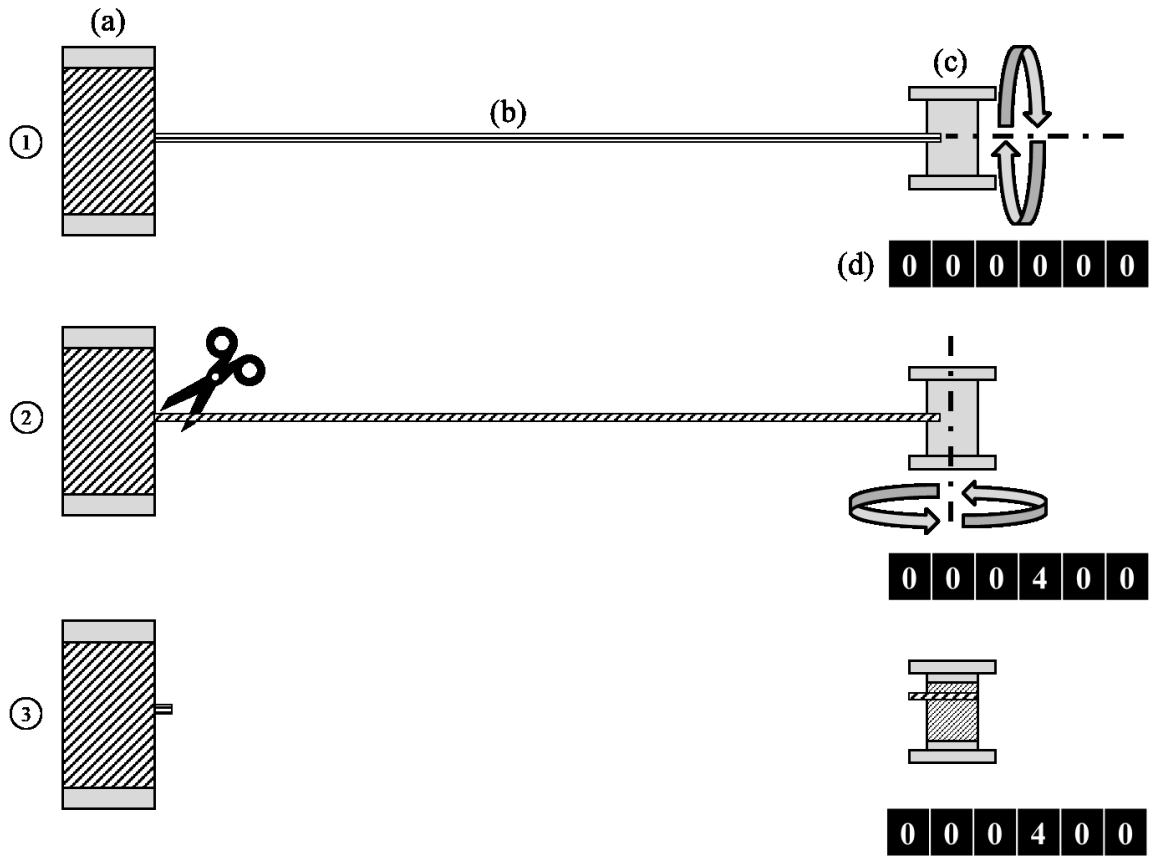

Figure 6-3: Schematic of twisting and winding operation, with (a) supplier yarn creel, (b) single continuous braiding yarn, (c) braider carrier bobbin, and (d) analog counter display.

The following formula was used to calculate the required number of revolutions:

$$rev = 10 \text{ m} \times TPM$$

For a 5 m length of yarn at 80 TPM, 400 revolutions were required, hence the analog counter attached to the twister/winder. Care was taken to allow sufficient slack in the yarn during this process as the twisting process resulted in some yarn contraction. Exact measurement of the yarn tension was not critical as the yarn carriers are self-tensioning.

6.3.3 Braiding

Braid preforms were manufactured with a horizontal maypole braider, as shown in Figure 6-1-3 (Steeger HS140/36-91, Steeger GmbH and Co., Wuppertal, West Germany). Settings were not altered for any of the samples, and since similar denier yarns were used for all samples (1580 denier Kevlar 29 and 1650 denier BioMid) samples were consistent with respect to the manufactured geometry. Melenka demonstrated the impact of both braid angle and braid pattern

with respect to elastic behaviour [11], which directed this decision to isolate twist behaviour from the other manufacturing factors. A Regular braiding pattern (two over, two under) was used for all samples.

The control inputs for the braider are linear pick density (picks per inch, or PPI) and table speeds (RPM). The correct settings were determined in a trial and error process, and then left unchanged for the preparation of all samples. The table speed did not alter braid geometry but only changed the speed at which braid was manufactured. Lower speeds were used for safety and consistency during production.

6.3.4 Twist configurations

Three different configurations were used for each braiding yarn. The default configuration is no additional twist; that is, yarns were not altered prior to braiding. Some twist may be induced throughout the winding or braiding processes, but is negligible compared to the twisted yarns. Twist could be applied to yarns in either the same direction as their helical path (co-twisted) or in the opposite direction to their helical path (counter-twisted). To be able to correctly identify and classify the types of TBCs manufactured, a twisted braid nomenclature is suggested here, like that used for ply notation. Yarns will be denoted by helical braid direction first (i.e. Z or S) followed by the twist direction (Z, S, or 0). Refer to Figure 6-4 for the directions associated with braiding yarns and yarn twist.

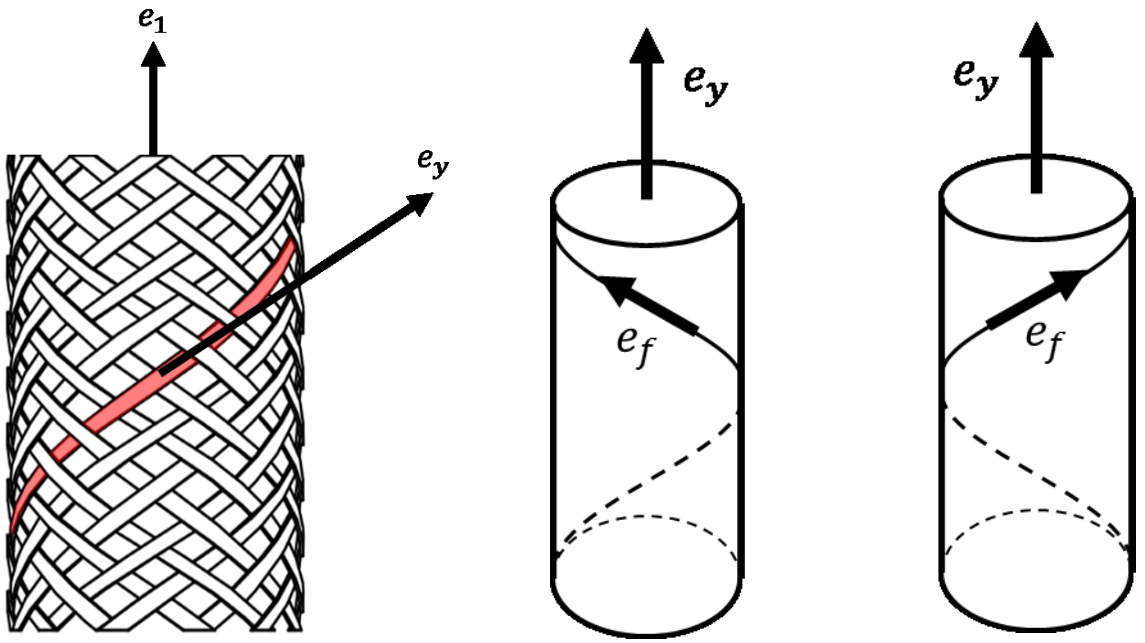

Figure 6-4: Sketches denoting the directions of yarns in a braided structure (a) and twist in twisted yarns (b) and (c). The sketch in (a) shows the braid structure with the longitudinal axis direction e_1 and the direction of the Z-yarn, e_y. This yarn may be twisted in either a Z-twist (b) or S-twist (c) configuration.

For example, a Z-S/S-0 braid will have Z helix yarns twisted in the S direction, and S helix yarns with no twist applied. See Table 6-1 for the possible configurations for a twisted TBC.

Table 6-1: Possible configurations for twisted TBC. Shaded cells represent those prepared in this experiment

		Z-carrier braider yarns		
		No twist (0)	Z-twist	S-twist
S-carrier braider yarns	No twist	Z-0/S-0 (‘Zero twist’)	Z-Z/S-0 (‘Half twist’, co-twisted)	Z-S/S-0 (‘Half twist’, counter-twisted)
	S-twist	Z-0/S-S (‘Half twist’, co-twisted)	Z-Z/S-S (‘Full twist’, co-twisted)	Z-S/S-S (‘Full twist’, co- and counter-twisted)
	Z-twist	Z-0/S-Z (‘Half twist’, counter-twisted)	Z-Z/S-Z (‘Full twist’, co- and counter-twisted)	Z-S/S-Z (‘Full twist’, counter-twisted)

These represent all the possible configurations for twisted TBCs. Three primary configurations were identified, that being zero twist, half twist, and full twist. The highlighted cells are those

that were manufactured for these studies, and the remaining configurations are effectively variations of those that were selected, the exception being the relative orientation of twist with respect to the braiding yarn. Two of the configurations selected are considered similar, the Z-Z/S-S and Z-S/S-Z and will be tested for significance. Note that here the angle of twist for all yarns is constant, that is, all twist is done to the exact same twist angle or not at all. In future work, additional configurations could be considered, and the notation altered to contain the final angle or twist level (such as Z-Z-80 for a Z-yarn Z-twisted at 80 tpm). Triaxial yarns could similarly be represented, for example "Z-Z/S-S/A-0" for a Z-twisted Z yarn, S-twisted S-yarn, and an axial yarn with no twist.

Three configurations of braids were prepared and tested for each material. First, a length of control preform was prepared without any twisted yarns (Z-0/S-0). All braids were manufactured as continuous textile braid preforms of approximately 2-3 meters in length.

Once these samples were manufactured, half of the carrier bobbins (all of the yarns from one helical direction) were removed from the braider. These bobbins were re-spooled with twisted yarns, as mentioned previously. In this case, the Z-helix carrier bobbins were removed first and yarn twisted in the S-direction was spooled onto the bobbins. These next samples, with the S-yarns untwisted and the Z-yarns S-twisted, were denoted as Z-S/S-0. Another 2-3 m of braid preform was manufactured with this configuration.

Finally, the remaining carriers (S-helix yarn carriers) were removed and Z-twisted, again to 80 tpm. A braided preform was manufactured in this Z-S/S-Z configuration. Once braid preforms were manufactured, they were cut to lengths of approximately 10 inches for curing.

6.3.5 Resin application and curing

Next, dry braid preforms were mounted on steel core PTFE rods (Figure 6-5a) for resin impregnation. Samples were impregnated manually and cured in an oven following manufacturer recommendations (Figure 6-5b). Finally, samples were cut to length to ensure braid properties, such as braid angle, were consistent throughout the sample (Figure 6-5c).

(a)

(b)

(c)

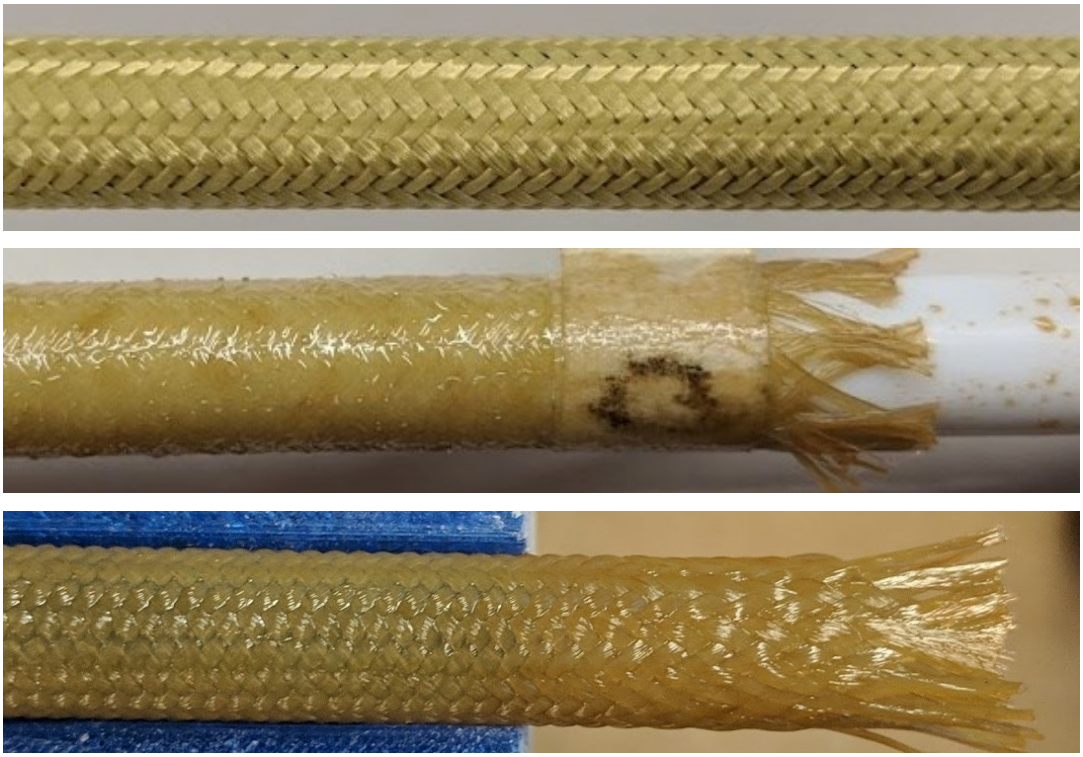

Figure 6-5: Specimen preparation process, including (a) dry preform, (b) impregnated preform on curing mandrel, (c) final cured sample ready for trimming and tab mounting.

Once the epoxy had been mixed, the braided preforms were manually impregnated with the resin. Ends of the braids were taped to prevent the braid from unravelling. Epoxy resin was applied first in excess, and then squeezed and worked to remove excess. Samples were then mounted vertically in an oven for curing. Vertical mounting was chosen over horizontal mounting since vertical mounting to account for the potential of resin flow. If mounted horizontally, the cross section may cure asymmetrically, and tensile loading of the samples could introduce a bending moment. By mounting vertically, the lower section of the sample may have greater resin content than the upper section, but the sample is likely to be under uniform tensile loading.

Once samples had been subject to the full curing schedule, they were slowly allowed to return to room temperature. TBCs were debonded from PTFE mandrels with minimal effort; a small amount of torque was applied by hand which then allowed the samples to be removed from the mandrels. Each sample was measured for length, internal diameter, and external diameter using a telescoping bore gauge (TESA USA, North Kingstown, RI) and a precision micrometer set

(Mitutoyo 103-907-40, Kawasaki, Japan) to a precision of 0.0001" at three points along the sample.

6.3.6 Preparation for testing

Samples were mounted onto custom end tabs using a 24 hour ambient cure high strength epoxy (Loctite E-60HP, Loctite) to ensure adequate bond strength during testing. Once the samples were mounted, they were painted using a flat black acrylic enamel spray paint. This coat reduces reflection from lighting during image capture an provides a quality background against which a white speckle pattern was applied using an airbrush. This white-on-black patterning was critical to DIC processing. Care was taken to not over-apply spray paint, which would result in an excessively thick coat of paint or worse, beads of paint on the surface. Testing was performed on an electro hydraulic tensile frame (MTS, Eden Prairie, MN, USA) with a load range of ±4.5 kN. All samples were tested with a constant rate of extension such that the yield point of the samples was met within one to two minutes of testing. For the Kevlar TBCs this was approximately 2 mm/min, while the BioMid samples were tested at slower rate of 1 mm/min to account for their decreased strength compared to the Kevlar samples. Image and load data were captured with custom Matlab software (Matlab R2017a, MathWorks Inc.) running simultaneously with the tensile frame.

6.3.7 Data processing

Load data was captured at a rate of 100 Hz and saved directly to the computer hard drive for future processing. Calculation and evaluation of each of the sample measures was done in Matlab (Matlab R2017a, MathWorks Inc.), while the ANOVA and post-hoc analyses were done in Excel (Excel, Windows).

6.3.7.1 Sample cross-sectional area (A_c)

The area was estimated as a circular annulus with a cross section defined by the two diametral measurements:

$$A_c = \frac{\pi\left(D_{avg}^2 - d_{avg}^2\right)}{4}$$

where D_{avg} is the mean external diameter and d_{avg} is the mean internal diameter. Diametral measurements were first averaged over three points on each sample, and then used to calculate the representative estimated area.

6.3.7.2 Linear modulus (E_1)

According to ASTM D3039, the linear modulus of a material can be determined through linear regression when digital data is available, as is the case in the current study. The limits of the regression were determined by the sample response during testing, and consistency between samples (specifically within material types) was attempted. The region for fitting had to be selected such that start-up slack (lower bound) and plastic deformation (upper bound) were avoided.

After this regression had been performed, samples were shifted such that the origin of the regression equation matched the origin of the stress-strain plot, in order to improve the accuracy of the reported strain values.

6.3.7.3 Yield stress and strain (σ_y and ε_y)

The calculated linear modulus for each sample was used to determine the offset yield point for each sample. This was done for 0.2%, 0.5%, and 0.8% yield offsets, due to the plastic behaviour in the upper portion of the stress-strain curve. Both the yield stress and strain are reported and compared across the twist groupings.

6.3.8 Digital image correlation

6.3.8.1 Digital image correlation hardware

Two AVT Prosilica GT3400 cameras were used in a stereo-digital image correlation (DIC) configuration, each with a resolution of 3384 x 2704 pixels. Lenses were 38 mm fixed focal length lenses at an approximate aperture of f8. The field of view was approximately 40 mm by 60 mm for each camera, while the combined ROI after image crop was approximately 10 mm by 60 mm. The stand-off distance (SOD) was approximately 40 mm. Monochromatic images were acquired every 2 seconds. Low temporal resolution was required as the samples were being tested quasi-statically.

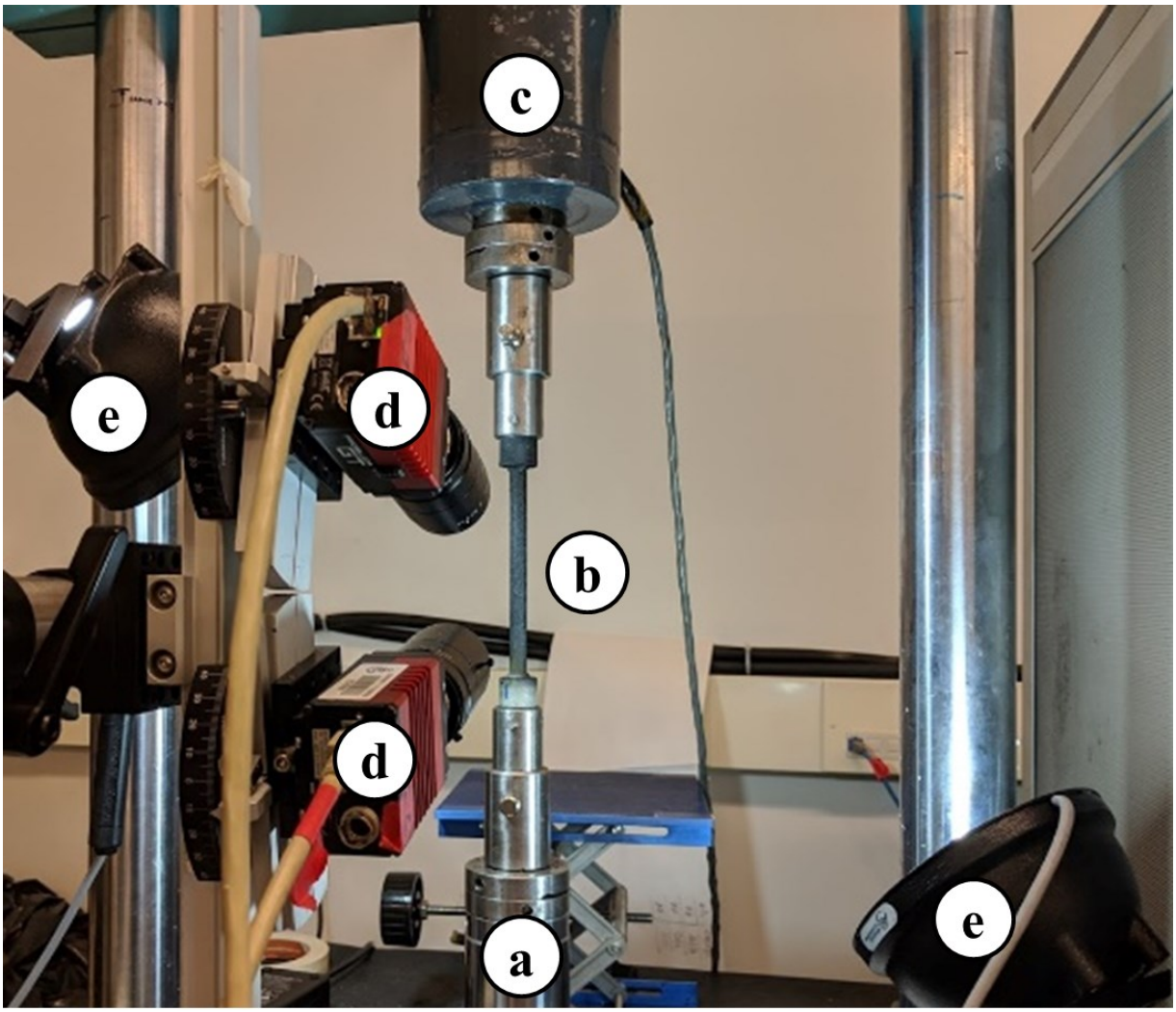

Figure 6-6: Image of testing and imaging setup. Load is applied via the hydraulic actuator (a) to the sample (b), while the load cell (c) is used to report applied load. Cameras (d) capture images of the sample, lit by the diffuse lights (e).

Samples were manually patterned a flat black base and white features. First, a flat black coat of acrylic paint was slowly applied using aerosol spray can. Once a satisfactory coat of paint had been applied, then the speckling was applied using manual airbrush (Paasche H Single Action Siphon Feed, Paasche, WI, USA). White features were manually assessed for quality, and an average size of 3-7 pixels was achieved.

6.3.8.2 DIC analysis

A commercial PIV/DIC package (LaVision DaVis 8.2.0, LaVision, Michigan, USA) was used for the DIC analysis. A custom stereo calibration target was used with a feature diameter of 1.25 mm, a feature-to-feature distance of 5 mm, and a height separation of 1 mm. Images were subject to preprocessing to optimize the contrast and intensity of images. A localized histogram

equalization was used to even out brightness across the image and improve contrast, as shown in Figure 6-7.

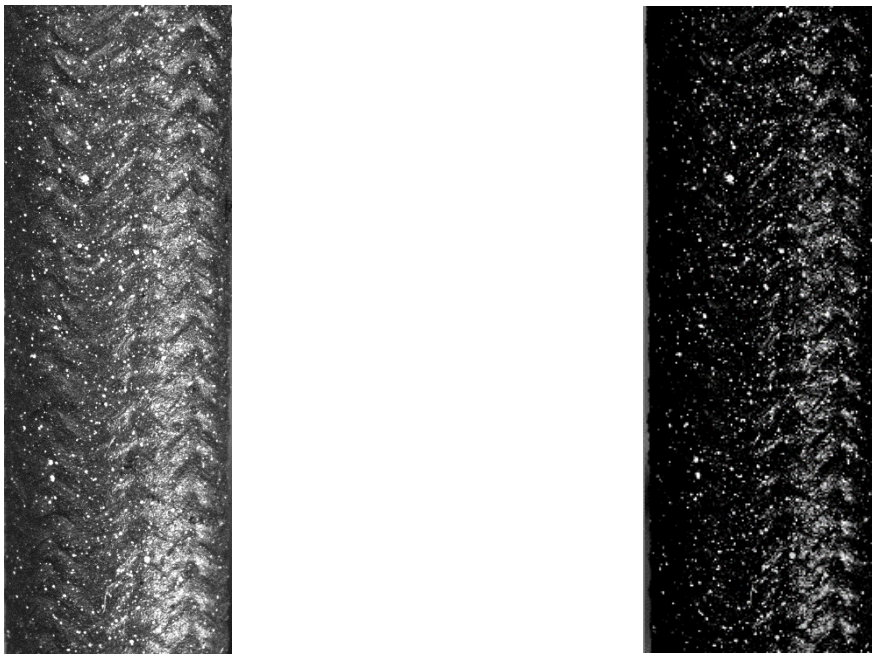

(a) (b)

Figure 6-7: Images from DIC process, including (a) raw cropped image prior to preprocessing, (b) image subject to filtering and contrast equalization

Image pre-processing is critical to remove patterns that may be influenced by the natural repeating pattern of the braid surface. If the repeating pattern of the braid is apparent in the speckling, then there will likely be some aliasing of the braid pattern in the deformation correlation which will bias and obscure the true strain results.

A square 31 x 31 pixel subset with a step size of 17 pixels was used for the image correlation process, as it was found to be a good balance between speed of calculation and spatial resolution of strain data. The quantity of interest was strain. Strain maps were produced for qualitative analysis of the failure mechanisms of the braid, while a virtual strain gauge 20 mm in length was used in the longitudinal direction in order to determine the tensile strain.

6.4 Results

For each sample, the results from Matlab were tabulated in Excel. Samples were grouped by twist treatment (zero twist, half twist, and full twist) and analyzed using a single factor ANOVA with post-hoc Tukey HSD where appropriate. That is, if the single factor ANOVA indicated a

significant difference between groupings, then and only then was the post-hoc analysis performed, to avoid any misleading conclusions.

6.4.1 Tensile properties

Four different measures for each sample were compared across the groupings: cross-sectional area (A_c), linear modulus (E_1), yield strain (ε_y), and yield stress (σ_y).

Table 6-2: Summary of results for Kevlar 49 twisted tubular braided composites. Statistical significance between twist groupings (α<0.05) is denoted as follows: * between Zero and Half, † between Zero and Full, and ‡ between Half and Full

Material	Kevlar 49		
Twist	Zero	Half	Full
Area [mm^2] †‡	16 ± 1	15 ± 1	18 ± 2
Elastic modulus [GPa]	4.4 ± 0.5	4.9 ± 0.5	4.3 ± 0.5
0.5% yield stress [MPa] *†	55 ± 4	62 ± 2	60 ± 2
0.5% yield strain [%]	1.8 ± 0.2	1.8 ± 0.1	1.9 ± 0.3

Table 6-3: Summary of results for Biomid twisted tubular braided composites. Statistical significance between twist groupings (α<0.05) is denoted as follows: * between Zero and Half, † between Zero and Full, and ‡ between Half and Full

Material	Biomid		
Twist	Zero	Half	Full
Area [mm^2] †	15.3 ± 0.8	16.0 ± 0.4	16.6 ± 0.8
Elastic modulus [GPa]	4.4 ± 0.1	4.8 ± 0.2	4.6 ± 0.3
0.5% yield stress [MPa] *†	44 ± 3	56 ± 1	58 ± 2
0.5% yield strain [%] †	1.5 ± 0.1	1.7 ± 0.1	1.8 ± 0.1

The stress-strain results for each sample were analyzed up to the point where the braid necking occurred. The longitudinal elastic modulus was determined through linear regression in the elastic region and was used to determine the strain offsets for yield calculation. Strain offsets were investigated at 0.2%, 0.5%, and 0.8% to show extended yield behaviour. Results were grouped by twist and compared to determine the significance of the twist treatment. A single factor ANOVA was carried out with the three groupings of each sample, tested at a significance of $\alpha = 0.05$. If treatments were significant to the tested parameter, a Tukey HSD post-hoc test was performed to determine the significance between groups. The results are summarized in the bar plots of Figure 6-8.

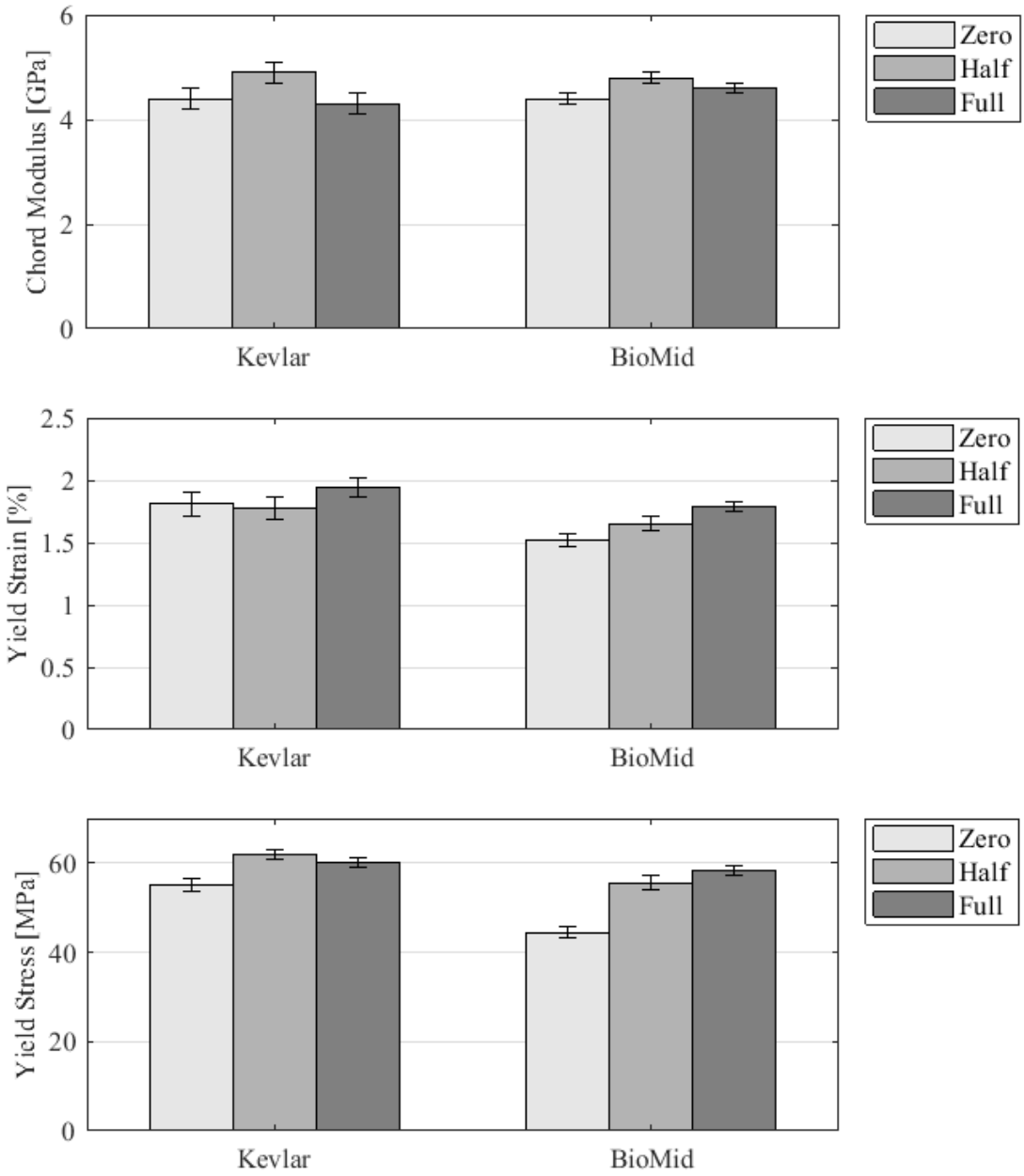

Figure 6-8: Bar plots of calculated parameters for all samples. Error plots scaled to the standard error for grouping and yield taken at 0.5% offset.

There was insufficient evidence to show twist altered elastic modulus for any of the samples. The highest elastic modulus for each grouping was with the half twisted samples. For yield strain, the Kevlar samples did not exhibit any conclusive behaviour as to the effect of twist at any of the offset yield measurements. However, for the BioMid samples, there was a significant effect at the 0.2% offset ($p = 0.007$), 0.5% offset ($p = 0.002$), and 0.8% offset strains ($p = 0.0003$). The Tukey HSD post-hoc test indicated the most significant difference in these

treatments between the zero- and full-twisted samples. The most significant results were that of yield stress at each offset level, for Kevlar ($p<0.03$) and BioMid ($p<7E-5$) samples. There was insufficient evidence as to any significant difference between the half- and full-twisted TBCs, but what the results do show is that there is an increase in yield strength for all twisted samples, regardless of the amount (half or full) added.

What is not reported here is the ultimate strength results. These followed the same behaviour as the yield stress but are not included as the focus was on the behaviour up to yield. As well, end tab debonding occurred for samples in the region between yield and ultimate stress.

6.4.2 DIC results

Since a constant rate of extension was used for all testing, the virtual strain gauge results were used primarily to confirm the strain rate of the tensile tests. A deeper analysis into the localized strain behaviour will be done at a later time given the high spatial resolution of the strain data, but for the purposes of the current study only the global strain from the virtual strain gauge was used. From a qualitative perspective, the DIC strain map provides insight into the possible failure mechanism. A sequence of strain overlays is provided in Figure 6-9 for sample K-FX-2.

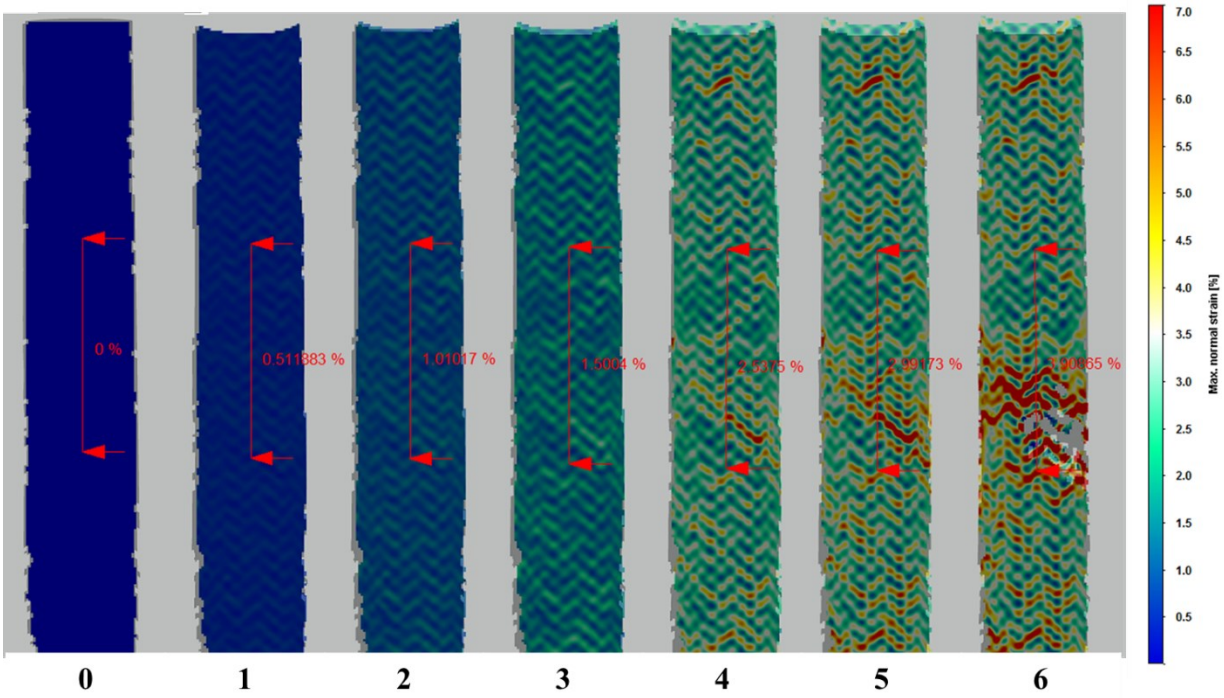

Figure 6-9: Strain map overlay of maximum normal strain for sample K-FX-2. Scale is from 0% (blue) to 7% (red) maximum normal strain. Numbers correspond to markers in Figure 6-10.

In the progression of strain overlays shown in Figure 6-9, it can be seen that there is a concentration of strain throughout the sample associated with the resin-rich regions of the sample. By image 3, the effect is quite pronounced throughout the braid structure. In image 4, at approximately 2.5% strain, a concentration of strain can be seen along the direction of the braiding yarns. This strain concentration quickly exceeds the scale used in the strain map, and is the origin of failure for the sample. When compared to the stress-strain curve for the sample as shown in Figure 6-10, it can be seen that there is relatively no change in stress between image 4 and 5, and the load capacity of the sample remains constant. This localized failure is analogous to the necking behaviour seen in ductile solids, such as steel.

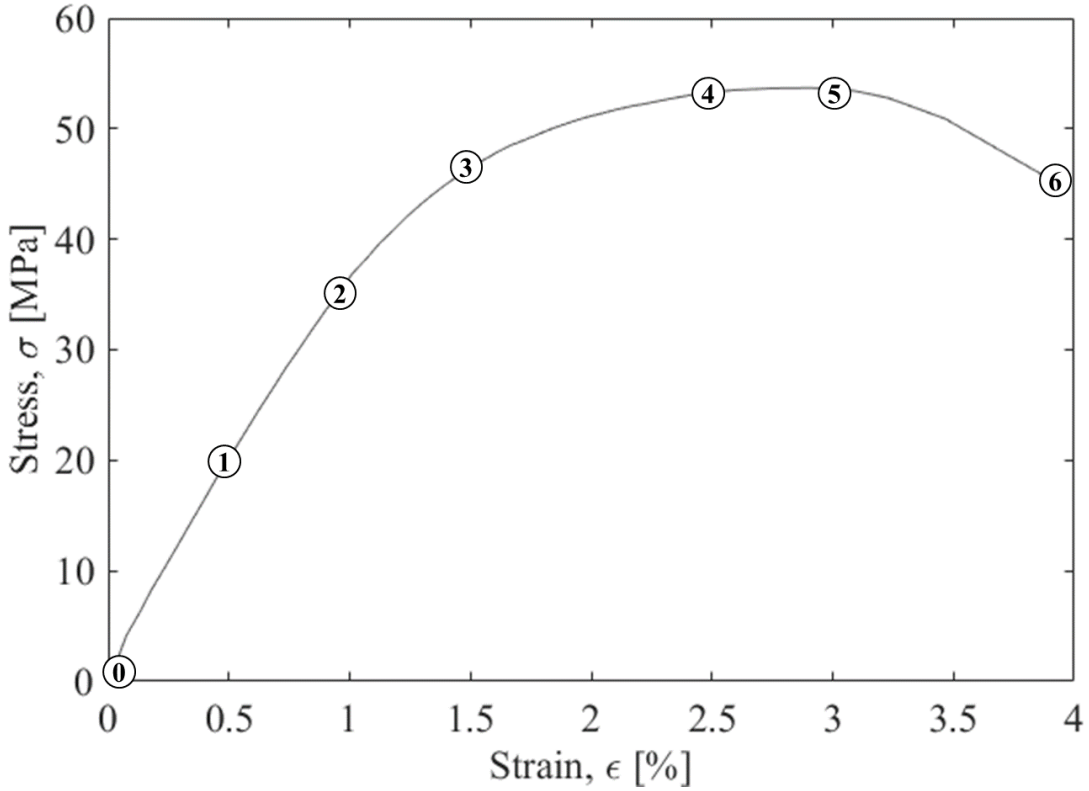

Figure 6-10: Plot of stress-strain curve for sample K-FX-2. Markers correspond to the strain map overlays shown previously in Figure 6-9.

Though Figure 6-9 and Figure 6-10 are for sample K-FX-2, this behaviour was seen throughout all of the samples tested, regardless of twist treatment or material. The only difference noted was that the half-twisted samples showed a tendency to exhibit strain concentration across a single diagonal direction, as shown in Figure 6-11.

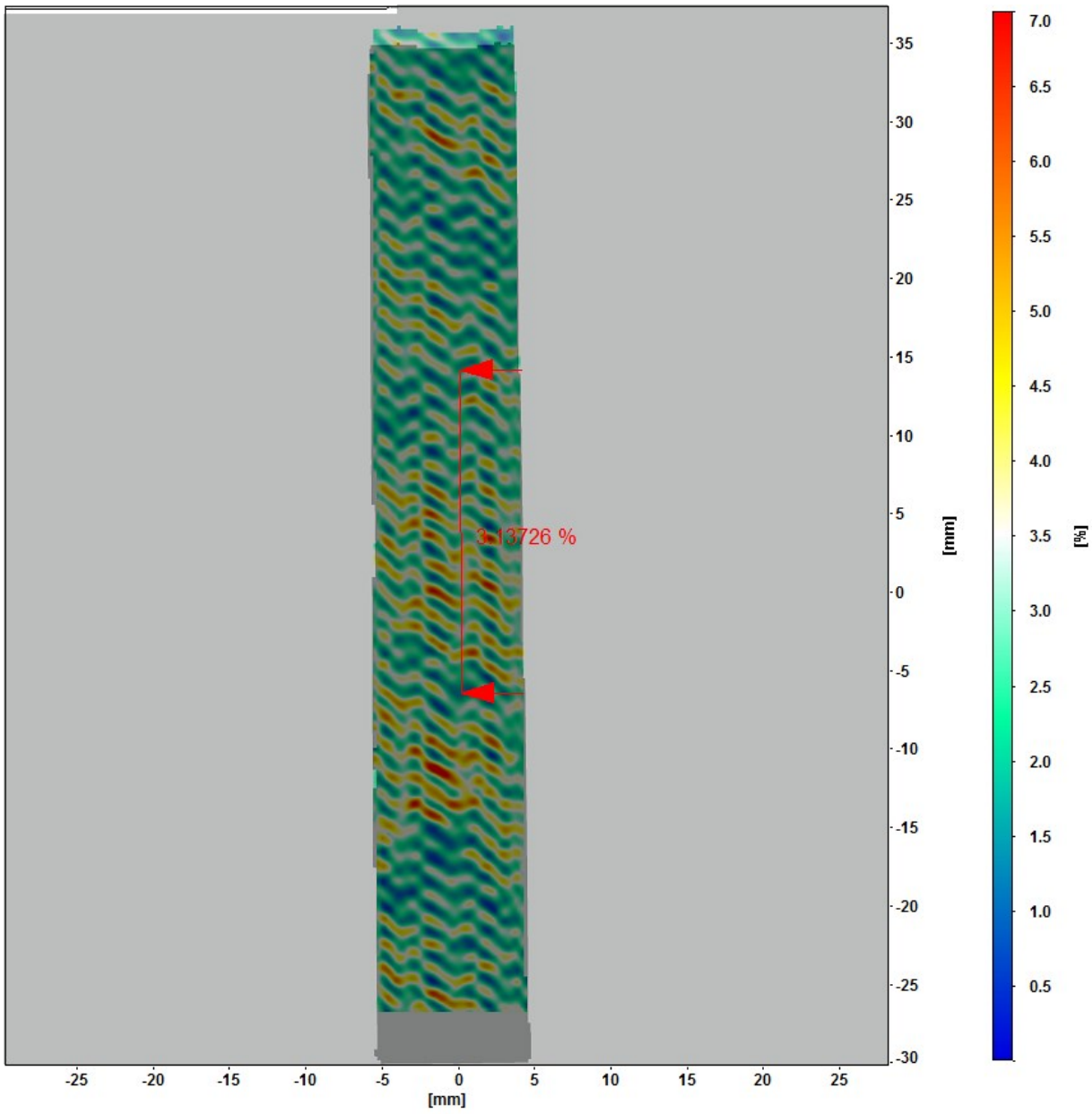

Figure 6-11: Strain map overlay for sample K-H-3. Note the concentration of strain occurs primarily in one diagonal direction. Colormap indicates longitudinal strain from 0% (blue) to 7% (red).

Unfortunately, it was not possible to determine which direction this is relative to the twisted yarns, as the orientation of which yarn within the TBC was twisted was not recorded. However, this does provide some insight as to the potential failure mechanism for TBCs and should be investigated further using the detailed strain data available from the DIC.

6.5 Discussion

6.5.1 Manufacturing observations

A few key differences were noted during the preparation of the twisted TBCs. During braid manufacture, the addition of twist reduced yarn hairiness of the yarn by increasing lateral cohesion of the individual filaments [112], as shown in Figure 6-12.

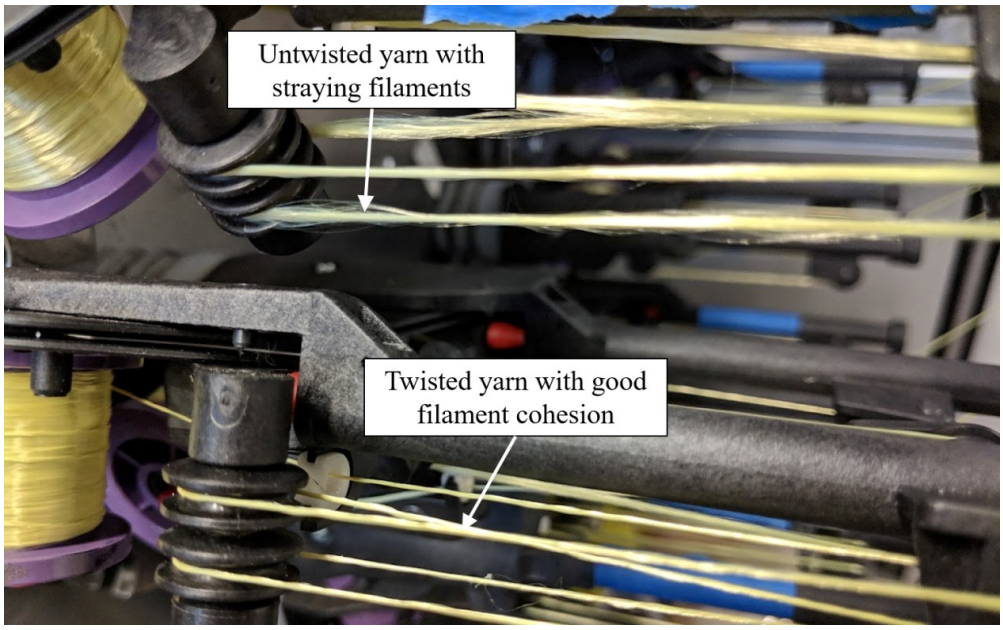

Figure 6-12: Image of untwisted and twisted yarns in braid yarn carriers highlighting change in filament cohesion

Without twist, individual straying filaments tended to get caught within the braiding machine, halting production. This may also be a safety precaution for future braiding operations with multifilament yarns. Next, it was noted that the shape of the yarns during the braiding process also changed. Rather than take the flat, ribbon-like shape of a typical multifilament yarn, again the increased lateral cohesion can be noted as the yarn seems to take a more elliptical cross section, as shown in Figure 6-13.

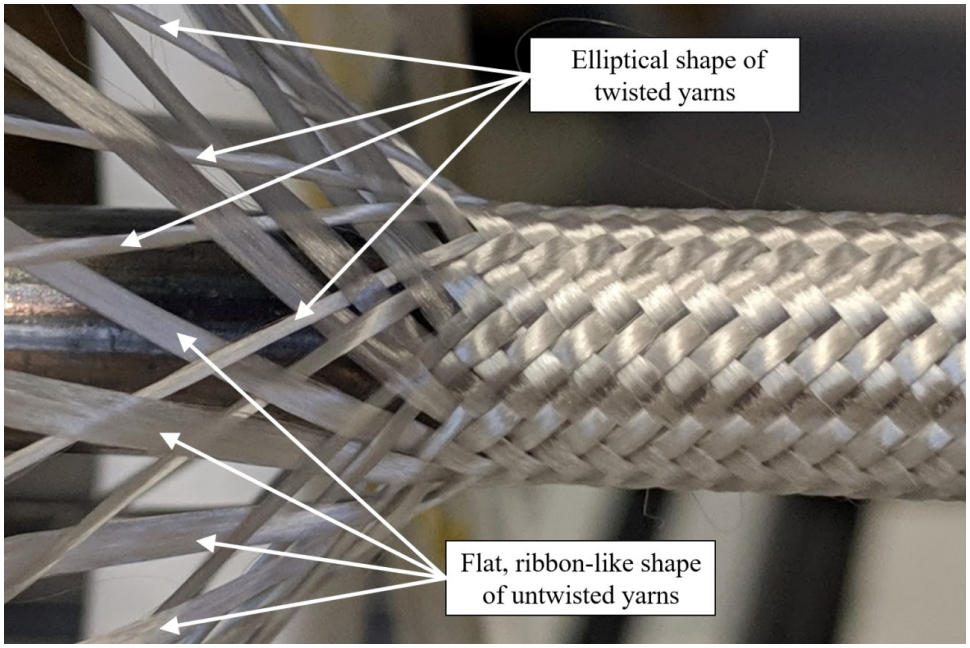

Figure 6-13: Image of braided yarns and interlacing region highlighting change in cross-section

Finally, it was also noted that overall appearance of the preform changed as well due to the change in yarn shape. An increase in the size of gap regions was present, as shown in Figure 6-14.

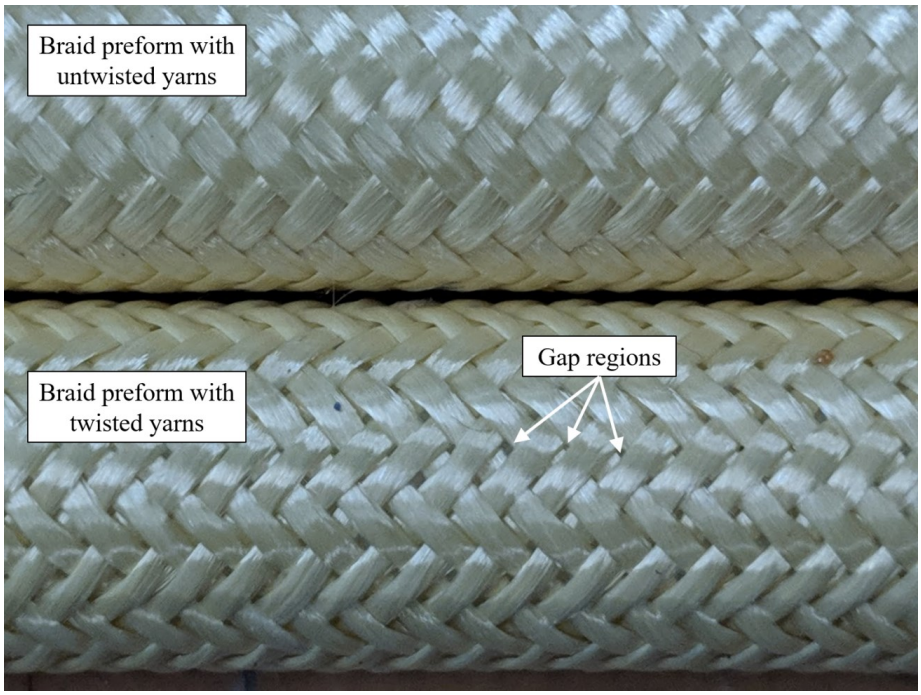

Figure 6-14: Image of twisted and untwisted braided preforms highlighting increase in gap regions

6.5.2 Area

As mentioned previously, the area was determined for each sample individually. However, it was noted that small deviations in the area measurement significantly impacted the evaluation of TBC properties, and that an average over the entire sample set was more appropriate. When samples were analyzed without any consideration for cross-sectional area (i.e. evaluated on a load-strain basis) the variance within sample groupings was lower than when the area was included in the calculation.

As well, it has been noted that there is no change in the quantity of fiber reinforcement used between samples and as well the volume fraction has been assumed constant, and thus the area should be assumed constant between samples. For the purposes of this study, specimen area was determined based on measurements due to guidelines in composite standards [42]. Future studies will investigate this further.

6.5.3 Stiffness

Multiple advantages to the use of the twisted yarns were noted throughout manufacture and testing. The addition of twist to textile process yarns is not a novel concept, as a small amount of twist, known as “producer’s twist”, is often added during manufacturing to assist with handling [3]. The typical level of twist added is typically on the order of 0 to 200 tpm. Thus, the 80 twists per meter used in this study are well within reasonable limits and implementation of this level of twist is would be minimally invasive to textile preform preparation.

6.5.4 Strength

In addition to manufacturing handling during manufacture, the addition of twist had a significant effect on the strength of the TBCs with minimal drawback. Prior to testing, it was predicted that a slight decrease in stiffness and increase in strength were feasible, since this has been shown to be the case in both twisted dry yarns and twisted composite yarns [3], [53]. The elastic modulus did not decrease, and in fact increased slightly with the addition of twist. The half-twisted samples had the highest stiffness, an effect that will need to be further investigated. The increase in yield strain is proposed to be related to the angled offset of the filaments. That is, due to the relative stiffnesses of the filament and matrix constituents. So long as the yield stress is not surpassed, it can be expected to see an increase in strain given the matrix constituent has a lower stiffness than the filaments.

The most surprising result was that of the increase of nearly 40% in yield strength with respect to the added twist. Previous analytical models of plain weave composites have predicted no significant change in strength when using twisted strands [67], but these results show otherwise. Both the half- and full-twisted samples had a significant ($p<0.03$) increase in yield strength over the untwisted samples. It should be noted that the full-twisted TBCs had the highest load capacity but this was offset somewhat by a significant difference ($p<0.03$) in cross-sectional area for these samples. This may be due to an increase in undulation height and the use of a flat-faced micrometer rather for measurement as it is approximating the true cross-sectional area.

Though twist improved the yield strength of tubular braided composite, the phenomenon is not solely related to an increase in strength of the individual braiding yarn. In Chapter 3, there is a noticeable increase in breaking strength of the dry yarn with respect to increased twist. However, in the presence of a composite matrix, as demonstrated in Chapter 5, the same strength increase is not seen. It is then proposed that the increase in strength observed for TBCs is related to the influence of twist on the textile structure rather than the composite behaviour.

With untwisted yarns, individual filaments can stray from the idealized cross section of a braiding. With twisted yarns, a more consistent braiding yarn cross section is achieved. From a textiles perspective this is the same as with any textile or apparel manufacture, however the effect has not been well documented for composite materials.

Further exploration is required in this manner. One such approach could include the microscopy of these twisted TBCs. Previous studies have shown that both conventional image microscopy as well as micro computed tomography both allow for the measurement and analysis of braided yarn cross-sections. It is predicted that the twist plays a role in maintaining a more consistent cross-section for each of the yarns, contributing to structure strength.

6.5.5 Failure progression

As shown in section 6.4.2, failure of TBCs is initiated and propagated along diagonal resin-rich regions of the braid. This has a few implications for analysis that should be investigated further. First, TBC failure is strongly governed by matrix properties. Though stiffness properties are associated primarily with both braid angle and the fiber reinforcement, the yield strength of a TBC may be more tied to matrix strength than it is to yarn strength.

One theory on the improved yield strength is related to the progressive failure behaviour of many textile composites [113]. Typically, the weakest part of the composite governs failure, and in the case of an untwisted yarn configuration, it is possible that the governing component is a single textile filament. Rupture or failure of this filament would accelerate failure for the rest of the composite. By applying even small amounts of twist, this progressive failure behaviour is mitigated since the entire yarn must fail rather than a single filament. Another theory is that the shear strength of the inter-yarn layers is improved by the twisted yarns. The mechanic by which this occurs is unclear at this stage but some of the differences from the untwisted state could be the relative filament angle between overlaid yarns or an increase in inter-yarn pressure.
Future studies should also focus on the ultimate stress in each sample so both the yield and post-yield behaviour can be captured.

6.6 Conclusions

TBCs were manufactured with low levels of twist added to individual braiding yarns. Small changes in longitudinal modulus and yield strain were observed, but most notably there was a significant increase in the yield strength ($p<0.03$) for all TBCs containing twist, and for the BioMid TBCs this was an increase of about 40% over the untwisted preparations. The twist also improved yarn handling and process safety during the multifilament braiding operation by preventing filament wandering. It is suggested that yarn twist be added to other multifilament textile composites in situations where improved yield strength is advantageous. Further work will include characterizing and attributing this increase in yield strength to specific components of the TBC.

Chapter 7 Modeling of plastic strain in twisted tubular braided composites

7.1 Introduction

Tubular braided composites (TBCs) are a textile composite that allow for tailoring of the mechanical properties through control of the manufacturing parameters [23]. They are seamless tubular structures with continuous helical yarn reinforcement throughout the structure. Previous studies have focused on modeling the linear elastic region as TBCs have been highlighted for their stiffness-critical applications [11], [114], [115]. TBCs have been noted to exhibit some plastic deformation and necking similar to ductile metals, but this behaviour has not yet been modeled, and as such these composites are often restricted to applications where the load is contained within the elastic zone. In particular, the development of a composite rebar has been attempted [6], and an improved understanding about this plastic behaviour could open up new possibilities for application and modeling. In this work the plastic behaviour beyond the elastic region and up to the yield point for TBCs is modeled using the Ramberg-Osgood equation. Additionally, the impact of using twisted yarns on the plastic behaviour of TBCs is characterized through the Ramberg-Osgood exponent.

7.2 Background

7.2.1 Stress-strain behaviour of TBCs

The stress-strain behaviour of TBCs can be broken down into three distinct sections, as shown in Figure 2-15.

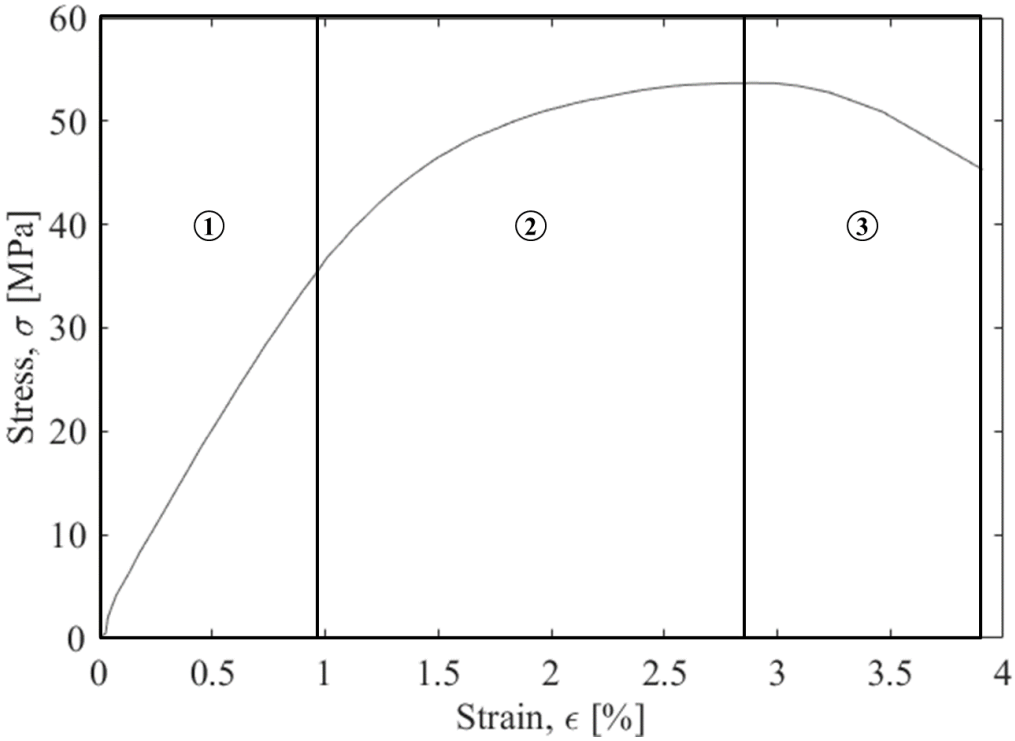

Figure 7-1: Plot of a representative stress-strain of longitudinal tensile behaviour of a TBC. Phase 1 is the elastic response, phase 2 is the plastic deformation up to the ultimate strength, and phase 3 is the yarn scissoring as the braid approaches the jamming point.

At the onset of tension, there is a region of linear extension within the linear elastic range of the material. Behaviour of TBC's in this region has been well documented [11], [58], [59]. Next, there is a plastic deformation phase, where the response is no longer linear. This region has previously been ignored for TBCs as the unidirectional composites of the same constituents do not express this behaviour. Following there is a necking phase, where the progressive degradation of the composite matrix allows for overlapping yarns to shear relative to each other in a scissoring fashion [62]. The effect resembles that of a necking metal sample, as the diameter of the TBC decreases during this phase, as shown in Figure 7-2.

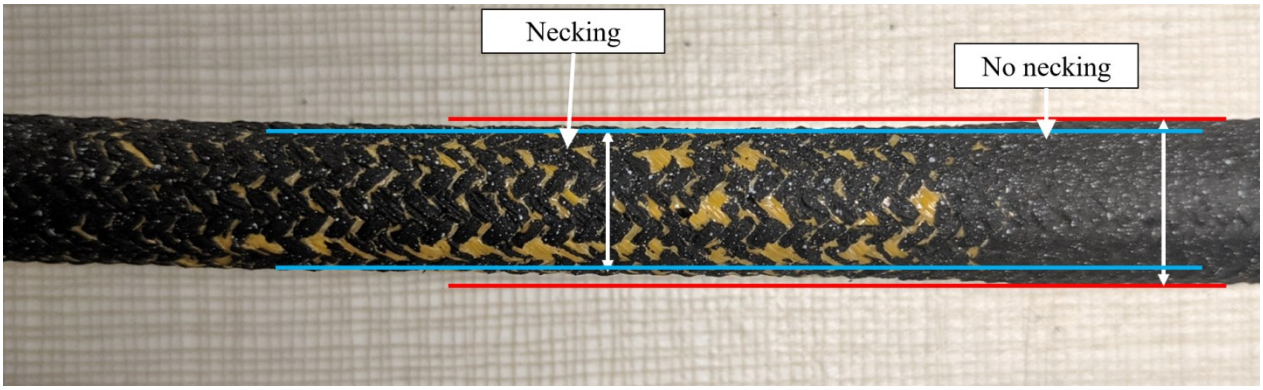

Figure 7-2: Image showing decrease in diameter of TBC due to necking

The yield point occurs right before this point and represents the transition between plastic deformation and necking. Stress can vary in this region, due to the complex nature of this phase. In this study, for example, the stress most often decreased with the constant extension rate. This step often involves very large deformations and is often not practical to test with typical tensile frame setups or traditional strain measurement systems. Finally the TBC will approach 'jamming' point, a point where the yarns can no longer physically move relative to one another [23],[33]. Here, the stress may rapidly increase again as this limit is met and the TBC soon fails. As mentioned, the linear elastic portion of these braids has been well documented, but there is little work to describe the behaviour beyond this region. Since there is a distinct linear elastic region and plastic region, the Ramberg-Osgood equation is a good candidate for the analytical modeling of TBCs up to the yield point.

7.2.2 Modeling nonlinear behaviour of composites

Traditionally this equation has been applied to metals, but some recent progress in composites modeling have shown its potential application to other materials. Bogetti et al. use the Ramberg-Osgood equation to model the nonlinear behaviour of a composite laminate [63], but this is restricted to the interlaminar shear direction and not applied to the longitudinal or in-plane shear. Cao et al. analyze the in-plane behaviour of a carbon-Dyneema® hybrid woven composite and use the Ramberg-Osgood equation to define the nonlinear behaviour of the Dyneema textile [64]. For these reasons and through observation of its yield behaviour the Ramberg-Osgood equation is a good candidate for application to TBCs. Beard and Chang attribute the nonlinear behaviour to the scissoring that occurs during the compressive longitudinal crushing of TBCs by continually updating the stiffness model as the braiding yarns rotate relative to each other [28].

However, if that same logic is applied to this study, that would imply the stiffness of TBCs increases during failure, which is contrary to the behaviour that has been observed.

7.2.2.1 Ramberg-Osgood equation

The Ramberg-Osgood equation is an analytical power law equation that can be used to describe the plastic deformation of the stress-strain curve of a material [65]. Technically, the Ramberg-Osgood equation can take multiple forms so long as both the elastic modulus and an exponent are involved, but in this work the form of the equation that uses the yield strength and offset will be used as shown in (7-1).

$$\varepsilon = \frac{\sigma}{E_0} + \alpha \left(\frac{\sigma}{\sigma_y}\right)^n \tag{7-1}$$

Where σ and ε are the stress and strain responses of the material, E_0 is the initial linear elastic modulus, α is the strain at the measured offset point and σ_y is the yield stress of the material as determined by the offset yield. The parameter n is the fit parameter that governs the stress-strain curve behaviour beyond the linear elastic region.

7.2.2.2 Shape variation of the Ramberg-Osgood equation

Three inputs define the stress-strain response of the Ramberg-Osgood equation and contribute to the its shape, as shown in Figure 7-3.

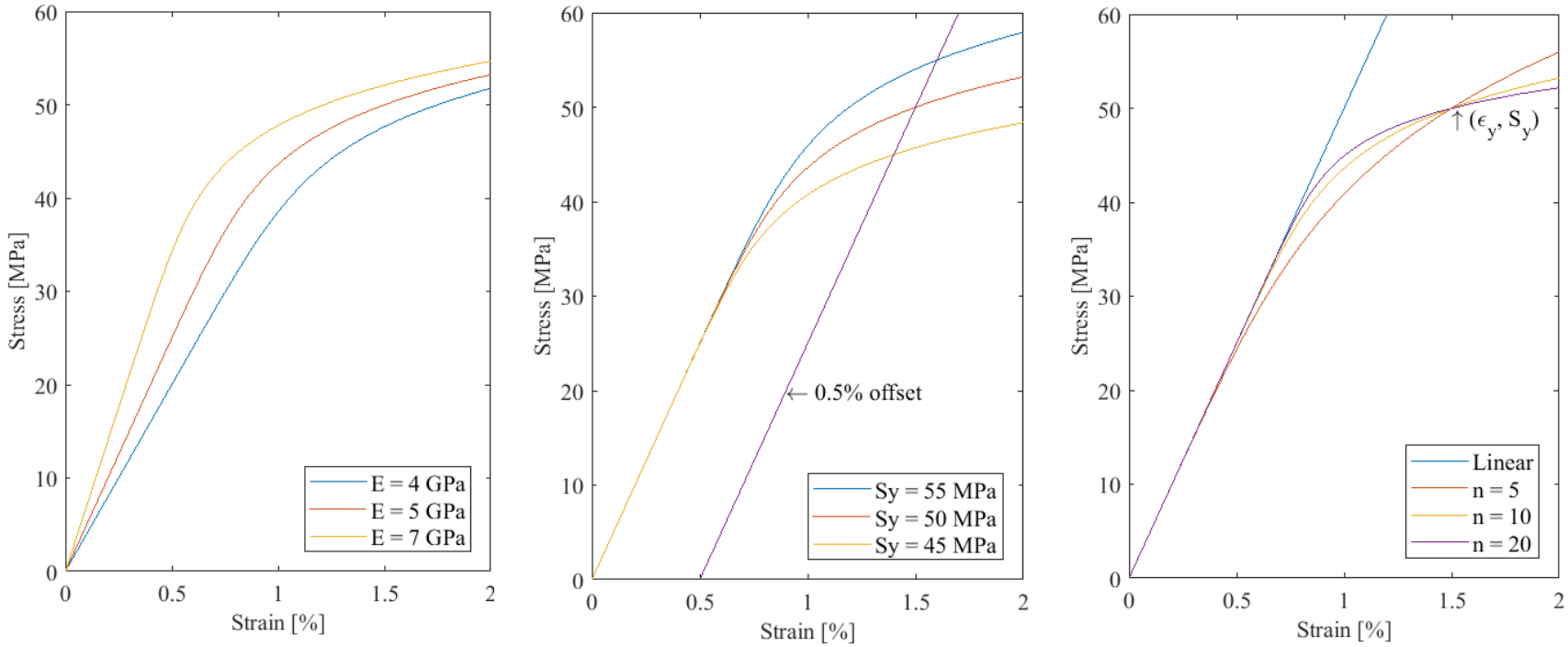

Figure 7-3: Plots showing simulated Ramberg-Osgood equation response to change in (a) elastic modulus, (b) yield strength, and (c) shape factor exponent n. All other inputs to the equation held constant in each case, which when not otherwise specified are $E = 5$ GPa, $S_y = 50$ MPa, and $n = 10$.

Change in the elastic modulus not only affect the linear region, but also affect the curvature response of the plastic zone since the offset yield point is also based on this value (Figure 7-3(a)). Change in yield strength does not affect the linear region, but still impacts the shape of the plastic zone prior to yield (Figure 7-3(b)). With the other two parameters held constant, changing the shape factor or Ramberg-Osgood exponent (Figure 7-3(c)) adjusts both the knee response between the elastic zone and the yield strength, as well as the 'flatness' of the plastic zone as it approaches the yield point. Note that the stress-strain curve still passes through the same yield point as determined by the offset method as the shape factor is changed.

7.3 Method

In a previous work, a pilot process was developed in which samples of TBCs were prepared with varying twist combinations. This process is outlined in Figure 6-1 and described in detail in section 5.3.

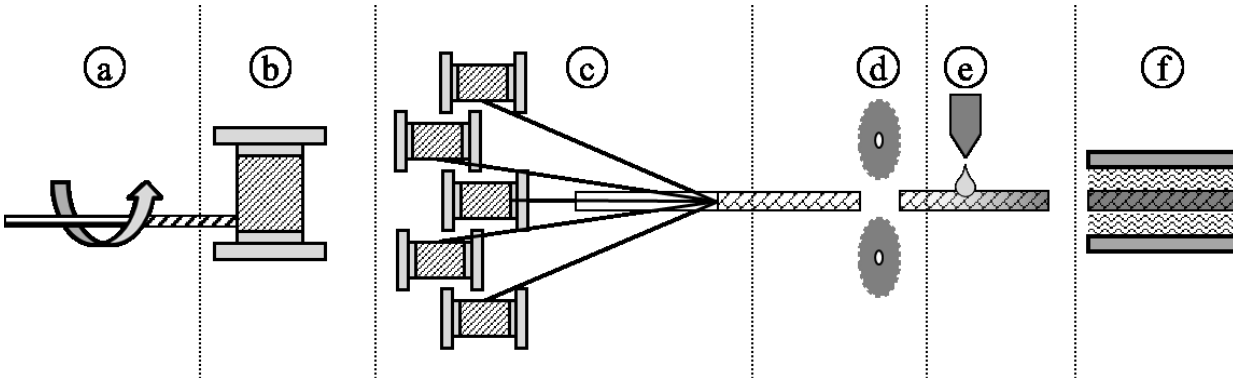

Figure 7-4: Schematic of the piloted twisted braided composite process. Continuous multifilament yarns are twisted (a) to 80 tpm and then wound (b) onto braiding bobbins. The spooled yarns are then used to braid (c) preforms and are subsequently cut (d) to length. Resin is impregnated (e) into the braids and finally cured (f) at elevated temperatures.

Braids were prepared with either no twisted yarns, with half of the braiding yarns twisted, or with all of the braiding yarns twisted. The addition of twisted yarns was found to most notably affect the yield strength of the samples. As well, the shape of the stress-strain curves was observed to be impacted by the addition of twist, and hence it was determined that an attempt to characterize this change in shape would be a logical next step in modeling the behaviour of TBCs with twisted yarns. Papirno [65] describes a process by which the Ramberg-Osgood equation is fit to a large set of data consisting of various metals and metallic alloys, and found excellent coherence to the model with over 90% of the samples

having an RMSE error of less than 1%. Here, the same general procedure is used to fit to the over 30 samples of TBCs. As mentioned previously, the tensile response of TBCs can be broken into three distinct regions: linear extension, plastic deformation, and necking. This study will focus on the linear extension and plastic deformation. In order to isolate the first two regions, only monotonically increasing data was included. Data past the point of maximum stress in the sample is removed for this study. After this point, the power-law equation cannot express the decrease in stress.

7.3.1 Linear elastic modulus

The elastic modulus of each samples was determined through a least-squares linear regression of the data over a range of pre-determined strain values. It was found that the range 0.3% - 0.6% strain was optimal for the samples, as it fell well below the proportional limit yet above any error from start-up slack in testing. After checking for goodness of fit for the elastic modulus regression, the samples were shifted to correct for strain offset such that the linear fit passed through the origin of the stress-strain curve, to ensure good fitting of the Ramberg-Osgood equation.

7.3.2 Yield stress and strain

The offset yield strain and stress are calculated by extending a line parallel to the calculated modulus originating at the point of yield offset. The point of intersect with the stress-strain curve is recorded as the yield stress (σ_y) and yield strain (ϵ_y) of the sample.

7.3.3 Plastic strain

It is assumed that the total strain of the sample can be broken down into a simple superposition of elastic and plastic strain. Thus, the plastic strain for each sample can be calculated assuming that $\varepsilon_p = \varepsilon - \frac{\sigma}{E_0}$, where ε is the sample strain and σ is the sample stress as determined experimentally. The stress is now plotted against the plastic strain only as in Figure 7-5. Note the first 30 MPa or so of applied stress appear as a straight vertical line, since there is no plastic strain occurring in the sample.

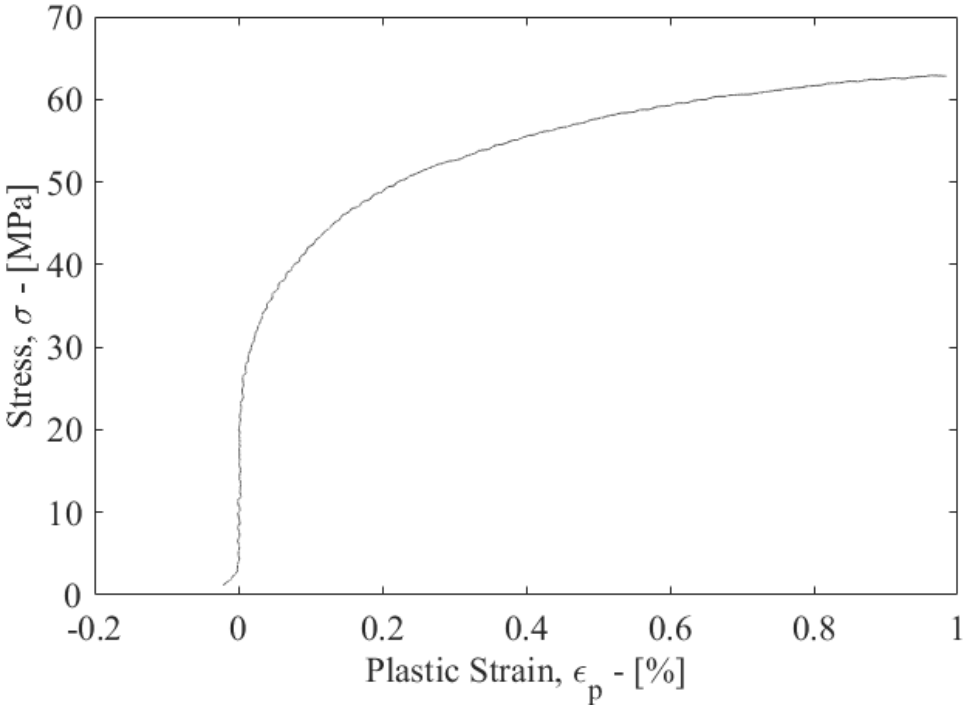

Figure 7-5: Representative plot of stress versus plastic strain

The elastic or proportionality limit of the sample is apparent in the stress versus plastic strain graph, since any non-zero positive strain shown is plastic strain. Equation (7-2) is generated by removing the elastic strain from (7-1).

$$\boldsymbol{\varepsilon_p = \alpha\left(\frac{\sigma}{\sigma_y}\right)^n} \tag{7-2}$$

As an example, (7-3) is (7-2) using the 0.2% offset yield.

$$\varepsilon_p = 0.002 \times \left(\frac{\sigma}{\sigma_y}\right)^n \tag{7-3}$$

The applied stress is then isolated in (7-4).

$$\sigma = A \cdot \left(\varepsilon_p\right)^{\frac{1}{n}} \tag{7-4}$$

The coefficient A is determined as in (7-5),

$$A = \frac{\sigma_y}{(0.002)^{\frac{1}{n}}} \tag{7-5}$$

Taking the natural logarithm of (7-4) yields (7-6), which can further be simplified as (7-7)

$$\ln(\sigma) = \left(\frac{1}{n}\right)\ln\left(\varepsilon_p\right) + \ln(A) \tag{7-6}$$

$$\ln(\sigma) = X_1 \ln(\varepsilon_p) + B \tag{7-7}$$

If the log of stress is plotted against the log of plastic strain, then the slope X_1 and the intersect B can be used to determine the value of n. The slope of the regression X_1 is equal to the inverse of the exponent as in (7-8).

$$n = \frac{1}{X_1} \tag{7-8}$$

The intercept B is used to find the yield stress through the relationship in (7-9).

$$\sigma_y = \exp(B) \cdot \alpha^{\frac{1}{n}} \tag{7-9}$$

The regression is limited to values above the proportional limit. For Figure 7-6, this is limited to stress values above 30 MPa, as can be seen in Figure 7-5. Note that some of the oscillatory behaviour seen in the plot is due to noise from the data collection. The effects are amplified for the small levels of strain.

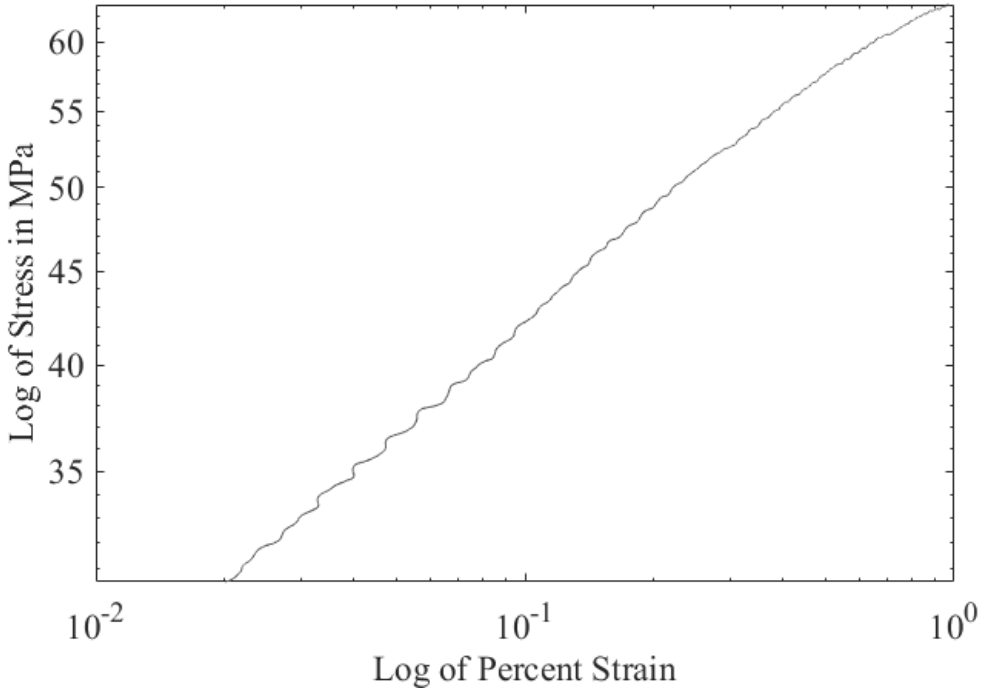

Figure 7-6: Representative log-log plot of stress and plastic strain

The linear regression is performed for log of stress versus the log of plastic strain using the built-in linear regression function in Matlab (Matlab R2017a, MathWorks Inc.). The regression is limited to strains above the linear fit region as determined by the prescribed upper bound, stresses above the proportional limit, and stresses below the offset predicted yield strength. To optimize the fit in this region, an initial guess of the proportional limit is

selected arbitrarily low with respect to the actual proportionality limit. A simple loop is then performed to optimize the fit by minimizing the root mean square error (RMSE) of the log-log regression. The loop is broken if the optimal proportional limit is found or if the proportional limit approaches the yield strength as predicted by the offset regression. The quality of fit is expressed by both the RMSE and the R2 of the log-log regression.

7.3.4 Statistical analysis

Once each sample had been appropriately fitted to the Ramberg-Osgood equation using the method discussed here, the results were compiled in Excel (Microsoft Office 365, Windows) and grouped according to twist for comparison. A single-factor ANOVA was used to compare the exponent of the Ramberg-Osgood equation across each twist grouping. A previous work compared the elastic modulus and offset yield strength and strain for these samples and the results were not significantly different enough to warrant a separate analysis. The ANOVA was performed at a significance level of $\alpha = 0.05$, and if a significant difference was noted then a Tukey-HSD follow-up test was performed to determine the which groupings were significantly different.

7.4 Results

For each sample, the elastic modulus, yield stress, yield strain, and Ramberg-Osgood model parameters were determined as described previously. The results of the process above are given here for the representative fully twisted Kevlar sample K-FX-4. Figure 7-7 shows the complete graphical results for the analysis.

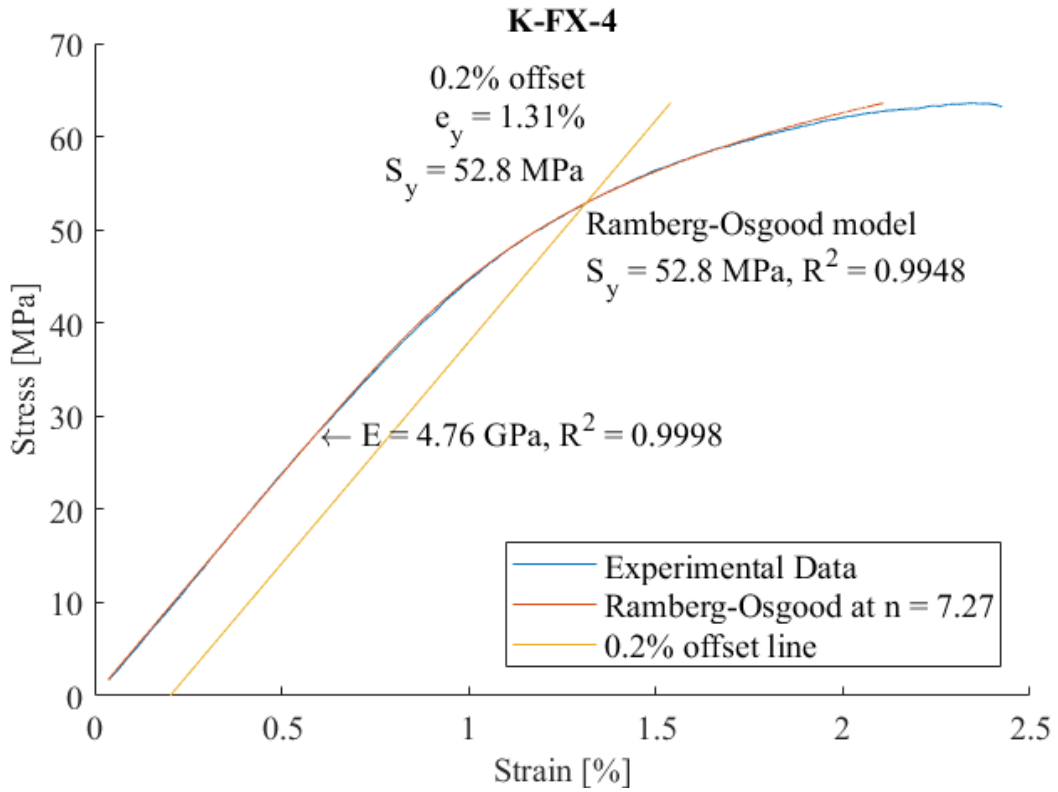

Figure 7-7: Plot of experimental data, 0.2% offset yield estimate, and R-O model determined through regression for sample K-FX-4

The results for sample K-FX-4 are compiled in the table below.

Table 7-1: Fitted parameters for sample K-FX-4

Region	Model	Parameters	R^2
Elastic	Linear	$E = 4.76$ GPa	0.9998
Plastic	Ramberg-Osgood	$n = 7.27,\ S_y = 52.8$ MPa	0.9948

Note that the fit for the linear and plastic regions is very good. As can be seen in Figure 7-7, however, the model begins to deviate further as the sample reaches the ultimate stress.

However, this model is developed only with results from below the yield point, so values exceeding this have no impact on the model.

Each of the samples were grouped according to their twist treatment and compared for significance at a level of $\alpha = 0.05$, as summarized in Table 7-2.

Table 7-2: Summary of means and standard deviations for fitted Ramberg-Osgood exponent across all sample groupings. Statistical significance between twist groupings (α<0.05) is denoted as follows: * between Zero and Half, † between Zero and Full, and ‡ between Half and Full.

	Kevlar		Biomid	
	0.2% offset *†	0.5% offset †	0.2% offset	0.5% offset †
Zero	12 ± 2	11 ± 3	5.7 ± 0.5	8 ± 2
Half	8 ± 1	9 ± 1	5.7 ± 0.4	7 ± 1
Full	7 ± 1	7 ± 1	5.5 ± 0.4	6 ± 1

Complete summaries of the elastic and plastic behaviour of TBCs under different twist treatments for both Kevlar 49 and Biomid samples are provided in Table 7-3 and Table 7-4, respectively.

Table 7-3: Summary of results for Kevlar 49 twisted tubular braided composites. Statistical significance between twist groupings (α<0.05) is denoted as follows: * between Zero and Half, † between Zero and Full, and ‡ between Half and Full

Material	Kevlar 49		
Twist	Zero	Half	Full
Area [mm^2] †‡	16 ± 1	15 ± 1	18 ± 2
Elastic modulus [GPa]	4.4 ± 0.5	4.9 ± 0.5	4.3 ± 0.5
0.5% yield stress [MPa] *†	55 ± 4	62 ± 2	60 ± 2
0.5% yield strain [%]	1.8 ± 0.2	1.8 ± 0.1	1.9 ± 0.3
Ramberg-Osgood exponent †	11 ± 3	9 ± 1	7 ± 1

Table 7-4: Summary of results for Biomid twisted tubular braided composites. Statistical significance between twist groupings (α<0.05) is denoted as follows: * between Zero and Half, † between Zero and Full, and ‡ between Half and Full

Material	Biomid		
Twist	Zero	Half	Full
Area [mm^2] †	15.3 ± 0.8	16.0 ± 0.4	16.6 ± 0.8
Elastic modulus [GPa]	4.4 ± 0.1	4.8 ± 0.2	4.6 ± 0.3
0.5% yield stress [MPa] *†	44 ± 3	56 ± 1	58 ± 2
0.5% yield strain [%] †	1.5 ± 0.1	1.7 ± 0.1	1.8 ± 0.1
Ramberg-Osgood exponent †	8 ± 2	7 ± 1	6 ± 1

7.5 Discussion

The results were used to develop bounded plots to summarize the results. First, the mean values are used to generate a representative curve, along with shading to represent a single standard deviation above and below each mean value.

7.5.1 Summary of responses

For the Kevlar TBCs, shown in Figure 7-8, the response in the linear region is quite consistent. However, in the plastic region, note that with increasing twist the plastic response changes. Note that both half and full twist increase the yield strength, but the full twisted samples change the shape factor the most.

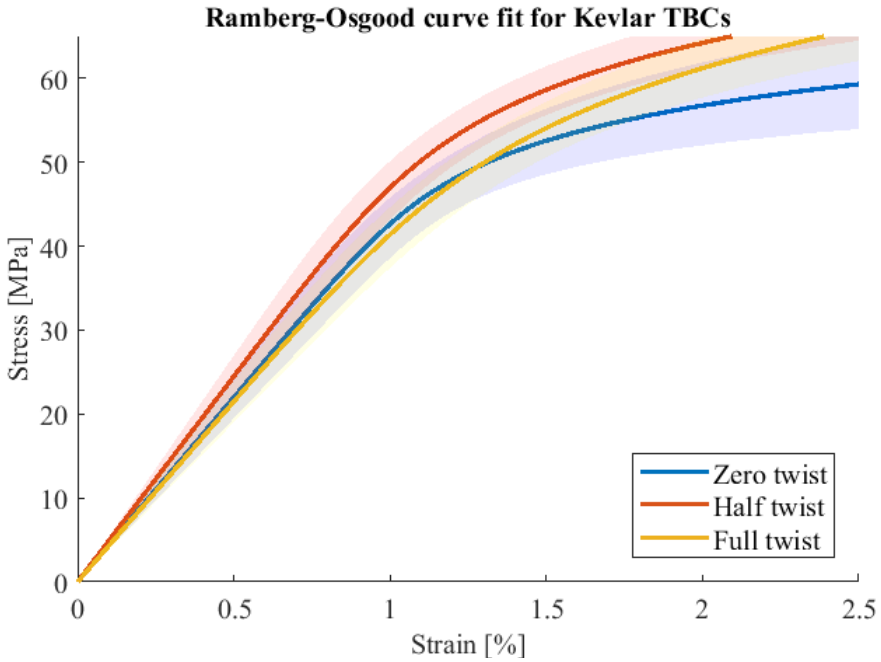

Figure 7-8: Plot of bounded stress-strain results for Kevlar TBCs. The solid line represents the modelling using mean values, while the shaded area represents ± one standard deviation for of the model in terms of elastic modulus, yield strength, and Ramberg-Osgood shape factor.

For the Biomid samples the effects of twist are even more pronounced, as can be seen in Figure 7-9. Again, the increase in yield strength is similar for both half and full twisted TBCs, and there is a slight change in the shape factor for the full twisted samples.

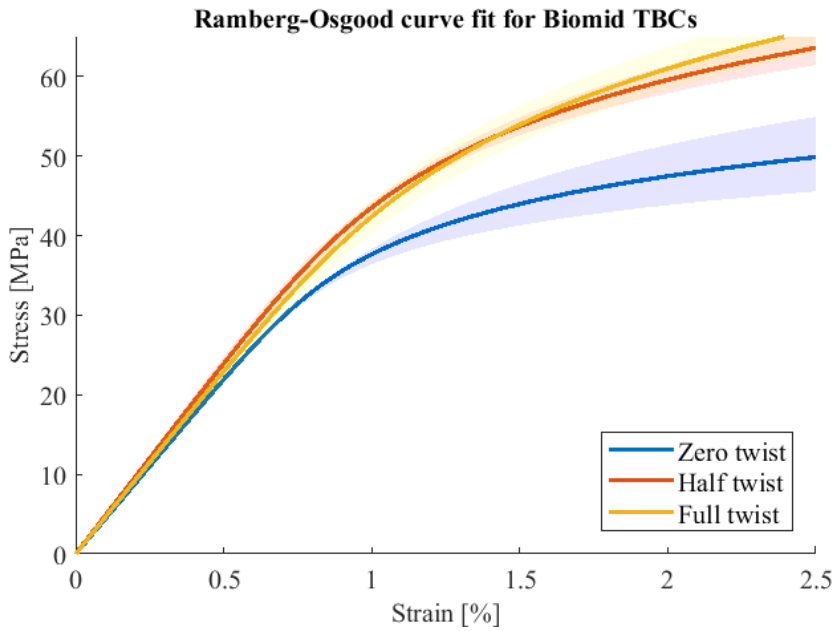

Figure 7-9: Plot of bounded stress-strain results for Biomid TBCs. The solid line represents the modelling using mean values, while the shaded area represents ± one standard deviation for of the model in terms of elastic modulus, yield strength, and Ramberg-Osgood shape factor.

Again, these are not predictive models, but rather descriptive ones, therefore these should be used with caution. However, they are a starting point for future work on developing predictive yield models for TBCs.

As well, the behaviour shown by adding twisted yarns to TBCs is very promising for use as a structural material. Even with little to no change in the elastic response, the plastic response shown would be preferred in several applications, such as concrete reinforcement where the additional load capacity would improve safety and prevent catastrophic failure.

7.5.2 Post-yield fit

All of the fitted models should good adherence to the experimental results in the pre-yield regions, but post-yield behaviour varied from sample to sample. Generally, there were three different behaviours in this region, which will be referred to as accurate estimation, underestimation, and overestimation of post-yield behaviour.

The following three figures demonstrate this post-yield behaviour with three untwisted Kevlar samples, all fitted at the 0.5% offset level. Figure 7-10 shows sample K-0-3 which demonstrates accurate post-yield behaviour that follows the trend of the data well into the post-yield region (to the right of the offset line intersection). Note that the fitted Ramberg-Osgood exponent here is $n = 10.6$, very close to the mean value determined previously.

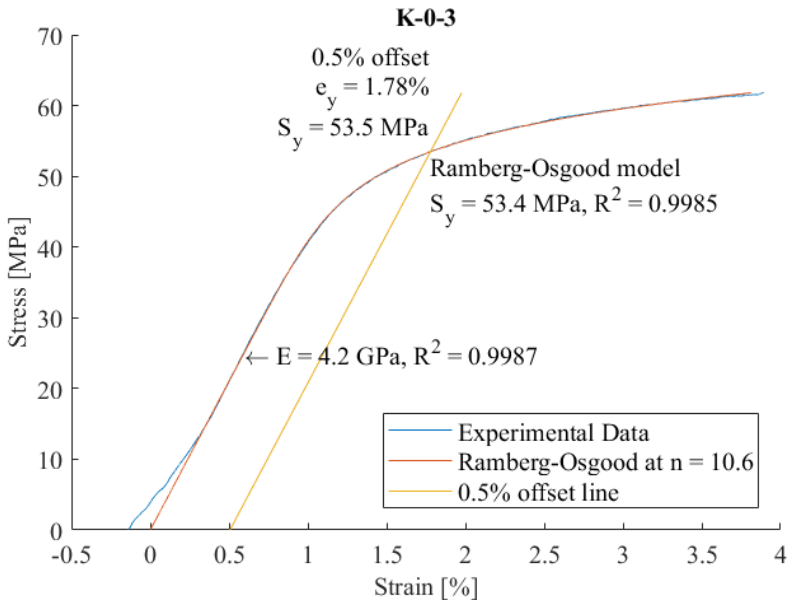

Figure 7-10: Plot of stress-strain results, offset yield, and fitter Ramberg-Osgood equation for sample K-0-3.

Figure 7-11 shows the results for sample K-0-9, which underestimates the stress in the post-yield region. Again, note the pre-yield region is well represented but the sample increasingly deviates from the results as the sample strain increases. The Ramberg-Osgood exponent in this case is $n = 14.5$, which just exceeds one standard deviation of the results. Again, note that increasing values of n result in a flatter stress response.

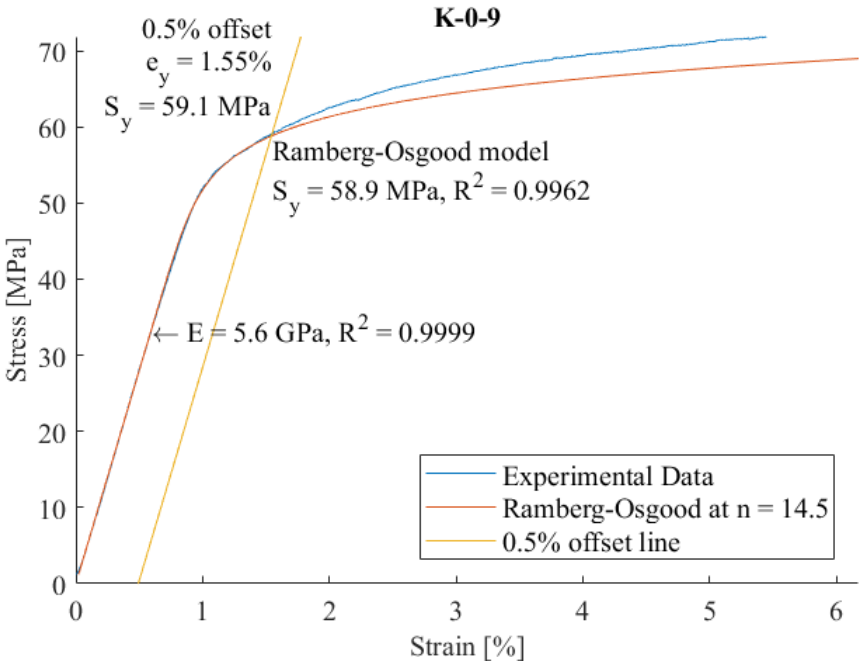

Figure 7-11: Plot of stress-strain results, offset yield, and fitter Ramberg-Osgood equation for sample K-0-9.

Figure 7-12 shows the results for sample K-0-4. Again, the pre-yield behaviour is well-represented but the post-yield behaviour of the model overestimates the stress response. Note that the Ramberg-Osgood exponent determined here was below but within a standard deviation of the mean value.

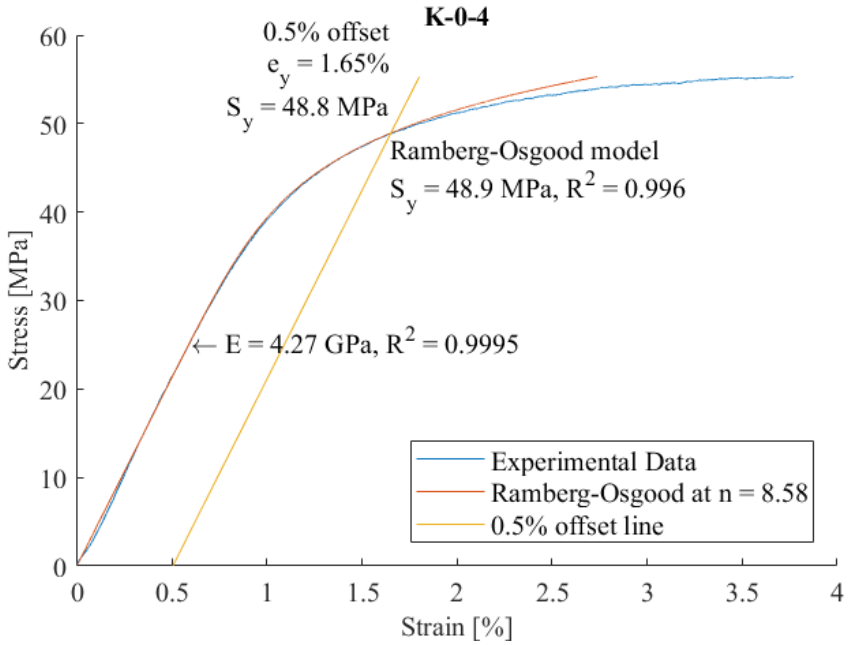

Figure 7-12: Plot of stress-strain results, offset yield, and fitter Ramberg-Osgood equation for sample K-0-4.

7.6 Conclusions

Tubular braided composites (TBCs) manufactured from both Kevlar 49 and Biomid yarns were tested under constant rate of extension past yield and up to failure. The elastic and plastic zones were isolated and then modeled using a linear fit for the elastic region and the Ramberg-Osgood equation for the plastic region. Provided that the only variables in the experiment were the material used and the level of twist, it was clear from the results that both have a notable impact on the yield behaviour of the TBC. Higher levels of twist resulted in a decrease in the Ramberg-Osgood exponent, improving the stress capacity in the low strain regions.

The Ramberg-Osgood equation is a good candidate for modeling the plastic behaviour of tubular braided composites. Three parameters are required for modeling: the linear elastic modulus, the yield strength and offset, and the shape parameter (or Ramberg-Osgood exponent). The shape parameter is dependent on the yarn material and the presence of twist in TBCs. Prediction of the elastic modulus of TBCs has been well documented, and future efforts should focus on predicting the yield strength and behaviour of these structures.

Chapter 8 Conclusions and future work

The manufacture of tubular braided composites (TBCs) combines both textiles and composites technologies, and the modeling of these materials should also reflect that. Yarn twist is often used in textile production but it is often neglected in traditional composite modeling approaches. In order to determine its impact on tubular braided composites, I performed tensile tests on yarns, unidirectional composites, and TBCs with and without twisted yarns. Overall, I have shown that the presence of low twist in these structures is not negligible, and in fact is often beneficial, especially in a textile composite structure such as a TBC.

8.1 Summary of conclusions

Throughout the results and discussions presented in this work, there are a few conclusions and recommendations which deserve specific mention when considering the original objectives of determining the impact of twisted yarns in tubular braided composites (TBCs).

1. Stiffness response is minimally impacted by low levels of yarn twist, especially in the presence of a composite matrix. In fact, for some TBCs the elastic modulus increased in the presence of twisted yarns.
2. The yield strength of TBCs is improved in the presence of low yarn twist. However, this was not due to an increase in tensile strength of the individual composite strand, and is suggested to rather be a result of the impact of twist on the shape of the individual yarn cross sections within the braid.
3. The plastic behaviour of TBCs is affected by twisted yarns. Notably, the presence of twisted yarns in TBCs improves the stress capacity and reduces plastic strain prior to yield. The Ramberg-Osgood equation is an excellent candidate for modeling the tensile behaviour of TBCs in the plastic zone.
4. Twisted yarns improve safety and handling throughout the braiding process. Without the presence of twist, individual filaments can stray from the yarn path and get caught within the rotating components of the braider. This is especially important when considering viability at a commercial scale.
5. BioMid is a viable material for TBCs, and when twisted yarns are used have a comparable tensile response to TBCs manufactured from Kevlar 49.

8.2 Future work

For future work in using twisted yarns in TBCs, the following objectives are proposed:

1. Further investigate the mechanism by which the yield strength is increased by using twisted yarns. It is suggested that this may be due to the twist affecting the braiding yarn cross section, but this would have to be investigated through either microscopy or nondestructively through computed tomography.
2. Predict the yield strength of TBCs. Though the Ramberg-Osgood can model the behaviour between the elastic region and the yield point, it cannot predict the yield strength. Further investigation as to both the governing factor in yield as well as the mode of failure progression is required.
3. Model the complete behaviour of TBCs up to ultimate failure. The necking phase and ultimate strength of TBCs has not been investigated, and the full potential of these structures will not be realized until such behaviour is well understood.

Bibliography

[1] M. Mollanoori and A. Alamdar-Yazdi, “Twist direction effect on the mechanical properties of woven fabric,” *Fibres Text. East. Eur.*, vol. 94, no. 5, pp. 48–55, 2012.

[2] B. C. Goswami, J. G. Martindale, and F. L. Scardino, “Yarn Structure,” in *Textile Yarns: Technology, Structure, and Applications*, New York: John Wile & Sons, Inc., 1977, pp. 76–87.

[3] A. Weinberg and P. Schwartz, “Twist effects on the mechanical behaviour of Kevlar 29/epoxy strands,” *J. Mater. Sci. Lett.*, vol. 6, no. 7, pp. 832–834, 1987.

[4] J. Carey, M. Munro, and A. Fahim, “Longitudinal Elastic Modulus Prediction of a 2-D Braided Fiber Composite,” *J. Reinf. Plast. Compos.*, 2003.

[5] A. Rawal, P. Potluri, and C. Steele, “Geometrical Modeling of the Yarn Paths in Three-dimensional Braided Structures,” 2005.

[6] J. P. Carey, *Handbook of Advances in Braided Composite Materials Theory, Production, Testing and Applications.* Elsevier Science, 2016.

[7] Q. Zhang, D. Beale, and R. M. Broughton, “Analysis of Circular Braiding Process, Part 1: Theoretical Investigation of Kinematics of the Circular Braiding Process,” *J. Manuf. Sci. Eng.*, vol. 121, no. 3, p. 345, 1999.

[8] F. K. Ko, “Braiding,” vol. 21, pp. 69–77, 2001.

[9] Q. Zhang, D. Beale, R. M. Broughton, and S. Adanur, “Analysis of Circular Braiding Process, Part 2: Mechanics Analysis of the Circular Braiding Process and Experiment,” *J. Manuf. Sci. Eng.*, vol. 121, no. 3, p. 351, 1999.

[10] W. J. Shanahan and J. W. S. Hearle, “12—an Energy Method for Calculations in Fabric Mechanics Part Ii: Examples of Application of the Method To Woven Fabrics,” *J. Text. Inst.*, vol. 69, no. 4, pp. 92–100, Apr. 1978.

[11] G. W. Melenka, “Analytical and Experimental Analysis of Tubular Braided Composites,” University of Alberta, 2016.

[12] K. Birkefeld, M. Röder, T. Von Reden, M. Bulat, and K. Drechsler, “Characterization of Biaxial and Triaxial Braids : Fiber Architecture and Mechanical Properties,” *Appl. Compos. Mater.*, vol. 19, pp. 259–273, 2012.

[13] V. Kling, S. Rana, and R. Fangueiro, “Fibre Reinforced Thermoplastic Composite Rods,” *Mater. Sci. Forum*, vol. 730–732, pp. 331–336, 2013.

[14] A. Rawal, H. Saraswat, and R. Kumar, “Tensile response of tubular braids with an elastic core,” *Compos. Part A Appl. Sci. Manuf.*, vol. 47, no. 1, pp. 150–155, Apr. 2013.

[15] T. Alpyildiz, “3D geometrical modelling of tubular braids,” *Text. Res. J.*, vol. 82, no. 5, pp. 443–453, Nov. 2011.

[16] D. Goyal, X. Tang, J. D. Whitcomb, and A. D. Kelkar, “Effect of Various Parameters on Effective Engineering Properties of 2 × 2 Braided Composites,” *Mech. Adv. Mater. Struct.*, vol. 12, no. 2, pp. 113–128, 2005.

[17] P. Qu, X. Guan, Y. Jia, S. Lou, and J. Nie, “Effective elastic properties and stress distribution of 2D biaxial nonorthogonally braided composites,” *J. Compos. Mater.*, vol. 46, no. 8, pp. 997–1008, Aug. 2011.

[18] J.-H. Byun, T. J. Whitney, G.-W. Du, and T.-W. Chou, “Analytical Characterization of Two-Step Braided Composites,” *J. Compos. Mater.*, vol. 25, no. December 1991, pp. 1599–1618, 1991.

[19] Y. Q. Wang, “Spatial Distribution of Yarns and Mechanical Properties in 3D Braided Tubular Composites,” *Appl. Compos. Mater.*, vol. 4, pp. 121–132, 1997.

[20] A. S. Wu, A. M. Coppola, M. J. Sinnott, T. W. Chou, E. T. Thostenson, J. H. Byun, and B. S. Kim, “Sensing of damage and healing in three-dimensional braided composites with vascular channels,” *Compos. Sci. Technol.*, vol. 72, no. 13, pp. 1618–1626, Aug. 2012.

[21] K. Xu and X. Qian, “Analytical prediction of the elastic properties of 3D braided composites based on a new multiunit cell model with consideration of yarn distortion,” *Mech. Mater.*, vol. 92, pp. 139–154, 2016.

[22] W. Ma, J. Zhu, and Y. Jiang, “Studies of fiber volume fraction and geometry of variable cross-section tubular 3D five-direction braided fabric,” *J. Compos. Mater.*, vol. 46, pp. 1697–1704, 2012.

[23] F. K. Ko, C. M. Pastore, and A. A. Head, *Handbook of Industrial Braiding*. Atkins & Pearce, 1989.

[24] A. Rawal, P. Potluri, and C. Steele, “Prediction of Yarn Paths in Braided Structures Formed on a Square Pyramid,” *J. Ind. Text.*, vol. 36, pp. 221–226, 2007.

[25] C. Ayranci and J. Carey, “2D braided composites: A review for stiffness critical

applications," *Compos. Struct.*, vol. 85, no. 1, pp. 43–58, Sep. 2008.

[26] J. Carey, D. Emery, and P. McCracken, "Buckling test as a new approach to testing flexural rigidities of angiographic catheters," *J. Biomed. Mater. Res. - Part B Appl. Biomater.*, vol. 76, no. 1, pp. 211–218, Jan. 2006.

[27] M. E. Yuksekkaya and S. Adanur, "Analysis of Polymeric Braided Tubular Structures Intended for Medical Applications," *Text. Res. J.*, vol. 79, no. 2, pp. 99–109, Feb. 2009.

[28] S. J. Beard and F.-K. Chang, "Energy absorption of braided composite tubes," *Int. J. Crashworthiness*, vol. 7, no. May 2013, pp. 191–206, 2002.

[29] M. A. Ivey, C. Ayranci, and J. P. Carey, "Modeling and mechanical characterization of braidtruded fiber reinforced polymer rebar," *Polym. Compos.*, vol. 39, no. 5, pp. 1582–1593, 2018.

[30] C. G. Pereira, R. Fangueiro, S. Jalali, M. Araújo, and P. P. Marques, "Tensile properties of braided composite rods," in *Fourth International Conference on FRP Composites in Civil Engineering*, 2008, pp. 22–24.

[31] B. C. Goswami, J. G. Martindale, and F. L. Scardino, "Geometry of Twisted Yarns," in *Textile Yarns: Technology, Structure, and Applications*, 1977, pp. 107–108.

[32] J. B. Hamilton, "40—a Direct Method for Measuring Yarn Diameters and Bulk Densities Under Conditions of Thread Flattening," *J. Text. Inst. Trans.*, vol. 50, no. 12, pp. T655–T672, Dec. 1959.

[33] J. Lyons and C. M. Pastore, "Effect of Braid Structure on Yarn Cross-Sectional Shape," *Fibers Polym.*, vol. 5, no. 3, pp. 182–186, 2004.

[34] B. Ozgen and H. Gong, "Modelling of yarn flattening in woven fabrics," 2011.

[35] F. T. Peirce, "5—the Geometry of Cloth Structure," *J. Text. Inst. Trans.*, vol. 28, no. 3, pp. T45–T96, Mar. 1937.

[36] Z. Du, "Theoretical Study on the Bending Rigidity of Filament Yarns with an Elliptical Cross-section Using Energy Method . I . Theoretical Modeling," vol. 11, no. 6, pp. 883–890, 2010.

[37] B. S. Jeon, "A Study on the Structural Properties of Plain Fabrics Using the Lenticular Model," *Fibers Polym.*, vol. 14, no. 11, pp. 1927–1932, 2013.

[38] A. Kemp, "An Extension of Peirce's Cloth Geometry to the Treatment of Non-circular

Threads," *J. Text. Inst. Trans.*, vol. 49, no. 1, pp. T44–T48, 1958.

[39] H. Gu and M. Miao, "Optimising fibre alignment in twisted yarns for natural fibre composites," *J. Compos. Mater.*, vol. 48, no. 24, pp. 2993–3002, 2013.

[40] ASTM, "ASTM D1423/D1423M-16: Standard Test Method for Twist in Yarns by Direct-Counting," 2016.

[41] D. Petrulis and S. Petrulyté, "Properties of close packing of filaments in yarn," *Fibres Text. East. Eur.*, vol. 11, no. 1, pp. 16–20, 2003.

[42] ASTM, "ASTM D2343-17: Standard Test Method for Tensile Properties of Glass Fiber Strands , Yarns , and Rovings Used in Reinforced Plastics 1," pp. 1–7, 2017.

[43] H. D. Wagner, S. L. Phoenix, and P. Schwartz, "A Study of Statistical Variability in the Strength of Single Aramid Filaments," *J. Compos. Mater.*, vol. 18, no. 4, pp. 312–338, 1984.

[44] Y. Rao and R. J. Farris, "Modeling and experimental study of the influence of twist on the mechanical properties of high-performance fiber yarns," *J. Appl. Polym. Sci.*, vol. 77, no. 9, pp. 1938–1949, 2000.

[45] J. W. S. Hearle, P. Grosberg, and S. Backer, "Extension of Continuous Filament Yarns," in *Structural Mechanics of Fibers, Yarns, and Fabrics*, New York: Wiley-Interscience, 1969, pp. 180–191.

[46] M. M. Platt, "Mechanics of Elastic Performance of Textile Materials: III. Some Aspects of Stress Analysis of Textile Structures - Continuous-Filament Yarns," *Text. Res. J.*, pp. 1–15, 1950.

[47] N. K. Naik and V. Madhavan, "Twisted impregnated yarns: elastic properties," *J. Strain Anal. Eng. Des.*, vol. 35, no. 2, pp. 83–91, 2000.

[48] J. W. S. Hearle, H. M. A. E. El-Behery, and V. M. Thakur, "23—The mechanics of twisted yarns: Further studies of the tensile properties of continuous-filament yarns," *J. Text. Inst. Trans.*, vol. 51, no. 8, pp. T299–T316, 1960.

[49] J. L. White, C. C. Cheng, and K. E. Duckett, "An Approach to Friction Effects in Twisted Yarns," *Text. Res. J.*, pp. 496–501, 1976.

[50] J. Baets, D. Plastria, J. Ivens, and I. Verpoest, "Determination of the optimal flax fibre preparation for use in unidirectional flax-epoxy composites," *J. Reinf. Plast. Compos.*, vol. 33, no. 5, pp. 493–502, 2014.

[51] D. U. Shah, P. J. Schubel, and M. J. Clifford, “Modelling the effect of yarn twist on the tensile strength of unidirectional plant fibre yarn composites,” *J. Compos. Mater.*, vol. 47, no. 4, pp. 425–436, 2013.

[52] S. Subramanian, K. L. Reifsnider, and W. W. Stinchcomb, “Tensile Strength of Unidirectional Composites: The Role of Efficiency and Strength of Fiber-Matrix Interface,” *ASTM*, 1995.

[53] N. K. Naik, I. Mudzingwa, and M. N. Singh, “Effect of twisting on tensile failure of impregnated yarns with broken filaments,” *J. Compos. Technol. Res.*, vol. 23, pp. 225–234, 2001.

[54] B. Bruni-bossio, C. Ayranci, J. P. Carey, T. Omonov, and J. Curtis, “Experimental testing of the tensile elastic properties of cellulose braided composites,” *Compos. Part B*, vol. 166, no. October 2018, pp. 542–548, 2019.

[55] E. Yamasaki, S. Sakurada, R. Nakamura, and K. Goda, “Identification of Migration Structure in a Natural Fiber Twisted Yarn and Its Effect on Tensile Strength,” *J. Soc. Mater. Sci. Japan*, vol. 64, no. 3, pp. 215–222, 2015.

[56] P. Uawongsuwan, Y. Yang, and H. Hamada, “Long jute fiber-reinforced polypropylene composite: Effects of jute fiber bundle and glass fiber hybridization,” *J. Appl. Polym. Sci.*, vol. 132, no. 15, pp. 1–13, 2015.

[57] a. Rawal, “Geometrical Modeling of the Yarn Paths in Three-dimensional Braided Structures,” *J. Ind. Text.*, vol. 35, pp. 115–135, 2005.

[58] J. Carey, “Predicting Elastic Constants of 2D-Braided Fiber Rigid and Elastomeric-Polymeric Matrix Composites,” *J. Reinf. Plast. Compos.*, vol. 23, no. 17, pp. 1845–1857, Nov. 2004.

[59] C. Ayranci and J. P. Carey, “Predicting the longitudinal elastic modulus of braided tubular composites using a curved unit-cell geometry,” *Compos. Part B Eng.*, vol. 41, no. 3, pp. 229–235, Apr. 2010.

[60] C. Ayranci, “Predicting the Elastic Properties of Two Dimensionally Braided Tubular Composite Structures Towards the Design of Braid-Reinforced Polymer Medical Catheters,” University of Alberta, 2010.

[61] A. K. Pickett, J. Sirtautas, and A. Erber, “Braiding Simulation and Prediction of Mechanical Properties,” *Appl. Compos. Mater.*, vol. 16, no. 6, pp. 345–364, Sep. 2009.

[62] G. W. Melenka, D. S. Nobes, and J. P. Carey, “3D DIC Measurement of Tubular Braided Composites,” in *The 19th International Conference on Composite Materials*, 2013, pp. 5781–5792.

[63] T. A. Bogetti, C. P. R. Hoppel, V. M. Harik, J. F. Newill, and B. P. Burns, “Predicting the Nonlinear Response and Progressive Failure of Composite Laminates,” *Compos. Sci. Technol.*, vol. 64, pp. 329–342, 2004.

[64] M. Cao, Y. Zhao, B. H. Gu, B. Z. Sun, and T. E. Tay, “Progressive failure of inter-woven carbon-Dyneema fabric reinforced hybrid composites,” *Compos. Struct.*, vol. 211, pp. 175–186, 2019.

[65] R. Papirno, “Goodness-of-Fit of the Ramberg-Osgood Analytic Stress-Strain Curve to Tensile Test Data,” *J. Test. Eval.*, vol. 10, no. 6, pp. 263–268, 1982.

[66] H. Ma, Y. Li, and Y. Luo, “The Effect of Fiber Twist on the Mechanical Properties of Natural Fiber Reinforced Composites,” in *18th International Conference on Composite Materials*, 2011.

[67] N. K. Naik and R. Kuchibhotla, “Analytical study of strength and failure behaviour of plain weave fabric composites made of twisted yarns,” *Compos. - Part A Appl. Sci. Manuf.*, vol. 33, no. 5, pp. 697–708, 2002.

[68] K. Sakoda, Y. Kadoma, and A. Nakai, “IV-7B Effects of Hard Twisted Yarn on Mechanical Property in Fiber Structural Hybrid Composite Materials,” *J. Soc. Mater. Sci. Japan*, vol. 60, no. 5, pp. 105–107, 2011.

[69] A. R. Torun, G. Hoffmann, A. Mountasir, and C. Cherif, “Effect of Twisting on Mechanical Properties of GF/PPCommingled Hybrid Yarns and UD-Composites,” *J. Appl. Polym. Sci.*, vol. 123, pp. 246–256, 2012.

[70] C. M. Leech, *The modelling and analysis of the mechanics of ropes*, vol. 209. 2014.

[71] S. S. Recchia, M. Tenorio, S. Horner, J. Q. Zheng, and A. A. Pelegri, “Analytical model of nonlinear twist dependency for Kevlar yarn based on local filament strain,” *Acta Mech.*, vol. 228, no. 2, pp. 561–574, 2017.

[72] M. Shioya, T. Itoh, T. Kunugi, and a. Takaku, “Variation of Longitudinal Modulus with Twist for Yarns Composed of High Modulus Fibers,” *Text. Res. J.*, vol. 71, no. 10, pp. 928–936, 2001.

[73] J.-H. Lin, I.-S. Tsai, W.-H. Hsing, and Z.-Z. Yang, “The Influence of the Twist

Direction on the Physical Properties of a Plied Yarn in a Rotor Twister," *J. Text. Inst.*, vol. 89, no. 3, pp. 480–484, 1998.

[74] J. Ma, B. Fan, Y. Gao, D. Gu, X. Qi, Y. Dong, Z. Hu, Y. Yang, Q. Zhang, and Y. Zhao, "Effects of Kevlar® 29 yarn twist on tensile and tribological properties of self-lubricating fabric liner," *J. Ind. Text.*, vol. 46, no. 8, pp. 1698–1714, 2017.

[75] C. Materials, "Introduction— Composite Materials and Optical Microscopy."

[76] R. H. Bossi and G. E. Georgeson, "The Application of X-Ray Computed Tomography to Materials Development," vol. 01, 1991.

[77] L. P. Djukic, I. Herszberg, W. R. Walsh, G. a. Schoeppner, B. Gangadhara Prusty, and D. W. Kelly, "Contrast enhancement in visualisation of woven composite tow architecture using a MicroCT Scanner. Part 1: Fabric coating and resin additives," *Compos. Part A Appl. Sci. Manuf.*, vol. 40, no. 5, pp. 553–565, May 2009.

[78] Y. Nishikawa, S. Baba, and M. Takahashi, "Optimization of X-Ray Computerized Tomography for Polymer Materials," *Int. J. Polym. Mater.*, vol. 62, no. 5, pp. 295–300, Mar. 2013.

[79] P. Schilling, B. Karedla, a Tatiparthi, M. Verges, and P. Herrington, "X-ray computed microtomography of internal damage in fiber reinforced polymer matrix composites," *Compos. Sci. Technol.*, vol. 65, no. 14, pp. 2071–2078, Nov. 2005.

[80] F. Stig and S. Hallström, "Spatial modelling of 3D-woven textiles," *Compos. Struct.*, vol. 94, no. 5, pp. 1495–1502, Apr. 2012.

[81] T. Shinohara, J. Y. Takayama, S. Ohyama, and a. Kobayashi, "Extraction of Yarn Positional Information from a Three-dimensional CT Image of Textile Fabric using Yarn Tracing with a Filament Model for Structure Analysis," *Text. Res. J.*, vol. 80, no. 7, pp. 623–630, Sep. 2010.

[82] F. Desplentere, S. V. Lomov, D. L. Woerdeman, I. Verpoest, M. Wevers, and a. Bogdanovich, "Micro-CT characterization of variability in 3D textile architecture," *Compos. Sci. Technol.*, vol. 65, no. 13, pp. 1920–1930, Oct. 2005.

[83] V. Revol, B. Plank, R. Kaufmann, J. Kastner, C. Kottler, and A. Neels, "Laminate fibre structure characterisation of carbon fibre-reinforced polymers by X-ray scatter dark field imaging with a grating interferometer," *NDT E Int.*, vol. 58, pp. 64–71, Sep. 2013.

[84] Y. Nikishkov, L. Airoldi, and A. Makeev, “Measurement of voids in composites by X-ray Computed Tomography,” *Compos. Sci. Technol.*, vol. 89, pp. 89–97, Dec. 2013.

[85] J. S. U. Schell, M. Renggli, G. H. van Lenthe, R. Müller, and P. Ermanni, “Micro-computed tomography determination of glass fibre reinforced polymer meso-structure,” *Compos. Sci. Technol.*, vol. 66, no. 13, pp. 2016–2022, Oct. 2006.

[86] F. J. Guild and J. Summerscales, “Microstructural image analysis applied to fibre composite materials: a review,” vol. 24, no. 5, pp. 383–393, 1993.

[87] G. W. Melenka, E. Lepp, B. K. Cheung, and J. P. Carey, “Micro-computed tomography analysis of tubular braided composites,” *Compos. Struct.*, vol. 131, pp. 384–396, May 2015.

[88] M. Ivey, J. Carey, and C. Ayranci, “Pseudoductile Composite Rebar Production and Characterization,” in *CANCOM2015 - Canadian International Conference on Composite Materials*, 2015, pp. 1–8.

[89] A. J. Kinloch, A. C. Taylor, M. Techapaitoon, W. S. Teo, and S. Sprenger, “Tough, natural-fibre composites based upon epoxy matrices,” *J. Mater. Sci.*, vol. 50, no. 21, pp. 6947–6960, 2015.

[90] G. W. Melenka, B. K. O. Cheung, A. Herve, and J. P. Carey, “Geometric and experimental analysis of tubular braided composites,” in *International SAMPE Technical Conference*, 2014.

[91] DuPont, “KEVLAR Aramid Fiber: Technical Guide.” 2011.

[92] J. H. Byun, “The analytical characterization of 2-D braided textile composites,” *Compos. Sci. Technol.*, vol. 60, no. 5, pp. 705–716, Apr. 2000.

[93] K. P. Baidya, S. Ramakrishna, M. Rahman, and A. Ritchie, “Quantitative radiographic analysis of fiber reinforced polymer composites.,” *J. Biomater. Appl.*, vol. 15, no. 3, pp. 279–289, Jan. 2001.

[94] B. Fiber, “How is BioMid Fiber Made?,” 2018. [Online]. Available: https://biomidfiber.com/how-is-biomid-fiber-made%3F. [Accessed: 24-May-2019].

[95] I. Qamhia, “Characterization of Regenerated Cellulose for Bio-based Epoxy Fibrous Composites,” University of Wisconsin-Milwaukee, 2013.

[96] C. Ayranci, D. Romanyk, and J. P. Carey, “Elastic Properties of Large-Open-Mesh 2D Braided Composites : Model Predictions and Initial Experimental Findings,” *Polym.*

Compos., 2010.

[97] Hexion, "SF 8017 Epoxy Resin System 826 862 LS-81K," 2019. [Online]. Available: https://www.hexion.com/en-AU/product/sf-8017-epoxy-resin-system-826-862-ls-81k. [Accessed: 24-May-2019].

[98] A. J. Hunt and J. P. Carey, "A machine vision system for the braid angle measurement of tubular braided structures," *Text. Res. J.*, vol. 0, no. 00, pp. 1–19, 2018.

[99] EcoPoxy, "EcoPoxy Clear Kit: Product Info," 2019. [Online]. Available: https://www.ecopoxy.com/wp-content/uploads/2018/08/EP_ClearKit_Handout_v2_proof.pdf. [Accessed: 24-May-2019].

[100] EcoPoxy, "EcoPoxy Clear Kit: Application & Uses," 2019. [Online]. Available: https://www.ecopoxy.com/wp-content/uploads/2019/01/EP_ClearKit_ApplicationSheet_v2.pdf. [Accessed: 24-May-2019].

[101] N. M. Barkoula, B. Alcock, N. O. Cabrera, and T. Peijs, "Fatigue properties of highly oriented polypropylene tapes and all-polypropylene composites," *Polym. Polym. Compos.*, vol. 16, no. 2, pp. 101–113, 2008.

[102] ASTM, "Standard Test Methods for Tire Cords , Tire Cord Fabrics , and Industrial Filament Yarns Made from Manufactured Organic-Base Fibers 1," *Astm*, no. June, pp. 1–39, 2015.

[103] S. T. Methods, "Standard Test Methods for Tensile Testing of Aramid Yarns," *Astm*, pp. 1–27, 2014.

[104] International Digital Image Correlation Society, *A Good Practices Guide for Digital Image Correlation*. 2018.

[105] LaVision GmbH, *DaVis 8.2 StrainMaster Product Manual*. Gottingen, 2014.

[106] B. Madsen, P. Hoffmeyer, A. B. Thomsen, and H. Lilholt, "Hemp yarn reinforced composites - I. Yarn characteristics," *Compos. Part A Appl. Sci. Manuf.*, vol. 38, no. 10, pp. 2194–2203, 2007.

[107] D. Ray, *Biocomposites for High-Performance Applications: Current Barriers and Future Needs Towards Industrial Development*. Woodhead Publishing, 2017.

[108] W. Gindl, M. Reifferscheid, R. B. Adusumalli, H. Weber, T. Röder, H. Sixta, and T.

Schöberl, “Anisotropy of the modulus of elasticity in regenerated cellulose fibres related to molecular orientation,” *Polymer (Guildf).*, vol. 49, no. 3, pp. 792–799, 2008.

[109] N. Graupner, S. Basel, and J. Müssig, “Size effects of viscose fibres and their unidirectional epoxy composites: application of least squares Weibull statistics,” *Cellulose*, vol. 25, no. 6, pp. 3407–3421, 2018.

[110] R. Chudoba, M. Vorechovsky, V. Eckers, and T. Gries, “Effect of Twist, Fineness, Loading Rate and Length on Tensile Behavior of Multifilament Yarns (A Multivariate Study),” *Text. Res. J.*, vol. 77, no. 11, pp. 880–891, 2007.

[111] J. Carey, A. Fahim, and M. Munro, “Design of braided composite cardiovascular catheters based on required axial, flexural, and torsional rigidities.,” *J. Biomed. Mater. Res. B. Appl. Biomater.*, vol. 70, no. 1, pp. 73–81, Jul. 2004.

[112] Y. Guo, X. M. Tao, B. G. Xu, K. F. Choi, T. Hua, and S. Y. Wang, “A continuous measurement system for yarn structures by an optical method - art. no. 115706,” *Meas Sci Technol*, vol. 21, no. 11, p. 15706, 2010.

[113] A. Shahbazi and B. Vaziri, “Progressive Damage Modelling of Notched Composite Materials under Tensile Loading.”

[114] C. Ayranci and J. P. Carey, “Effect of Diameter in Predicting the Elastic Properties of 2D Braided Tubular Composites,” *J. Compos. Mater.*, vol. 44, no. 16, pp. 2031–2044, May 2010.

[115] J. Carey, M. Munro, and A. Fahim, “Regression-based model for elastic constants of 2D braided/woven open mesh angle-ply composites,” *Polym. Compos.*, vol. 26, no. 2, pp. 152–164, Apr. 2005.

Appendix A: Material properties

Table A-1: Properties of yarn composite constituents.

Yarn material	Kevlar 49	BioMid
Denier (den)	380	1600
Tensile modulus (g/d)	885	315
Tensile modulus (GPa)	112.4	42
Breaking tenacity (g/d)	23.6	8.5
Elongation at break (%)	2.4	4.5

Table A-2: Uncured resin and hardener properties

Commercial name	**Chemical composition**			**Specific gravity**	**Viscosity [cP at 25°C]**	**Appearance**
	Identification, CAS number:	**Name**	**% by weigh t**			
Epon 826	25068-38-6	4,4'-Isopropylidenediphenol-Epichlorohydrin Copolymer	100	1.16	6500-9500	Clear viscous liquid
Lindau LS-81K	34090-76-1	Methyltetrahydrophthalic anhydride	>50	1.19	170-250	Green liquid
	85-43-8	Tetrahydrophthalic anhydride	10-20			
	56-37-1	Benzyltriethylammonium chloride	1-10			
	85-44-9	Phthalic anhydride	1-5			
EcoPoxy Part A	25085-99-8	2,2'-[(1-Methylethylidene)bis(4,1-phenyleneoxymethylene)]bisoxirane homopolymer	70-90	1.1	650	Clear viscous liquid
	68609-97-2	Alkyl C12-C14 Glycidyl Ether	8-25			
EcoPoxy Part B	25265-17-2	Formaldehyde, oligomeric reaction products with 3-aminomethyl-3,5,5-trimethylcyclohexylamine and phenol	100	1.03	370	Yellow tinted liquid

Table A-3: Mix and cure properties of curing system combinations

Resin	**Hardener**	**Mix ratio**	**Mixed viscosity [cP]**	**Tensile modulus [GPa]**	**Cure profile [hrs/°C]**
Epon 826	Lindau LS-81k	1:1	1230	2.7 GPa	1.5/66, 1/85, 3/150
Ecopoxy Part A	Ecopoxy Part B	3:1	N/A	2.7 GPa	48/21

Appendix B: Yarn area estimate calculations

The following pages were used in the calculation of the yarn area estimates described in section 2.3.6.

Summary of Properties and Area Estimations

Kevlar 49, 1140 denier

$n_f := 768$	Number of filaments in yarn
$D_f := 12\ \text{micron}$	Filament diameter
$den_y := 1140\ \text{den}$	Yarn denier (g/9000 m)
$\rho := 1.44\ \frac{\text{g}}{\text{cm}^3}$	Material density
$E_{metric} := 112.4\ \text{GPa}$	Modulus in metric units
$E_{textile} := \frac{885}{101.97}\ \frac{\text{N}}{\text{den}}$	Modulus in textile units

$n_f \cdot \frac{D_f^{\,2} \cdot \pi}{4} = 0.08686\ \text{mm}^2$	Filament area estimation
$\frac{den_y}{\rho} = 0.08788\ \text{mm}^2$	Density estimation
$\frac{E_{textile} \cdot den_y}{E_{metric}} = 0.08803\ \text{mm}^2$	Back calculated estimation

Summary of Properties and Area Estimations

Kevlar 29, 1500 denier

$n_f := 1000$	Number of filaments in yarn
$D_f := 12\ \text{micron}$	Filament diameter
$den_y := 1500\ \text{den}$	Yarn denier (g/9000 m)
$\rho := 1.44\ \frac{\text{g}}{\text{cm}^3}$	Material density
$E_{metric} := 70.5\ \text{GPa}$	Modulus in metric units
$E_{textile} := \frac{555}{101.97}\ \frac{\text{N}}{\text{den}}$	Modulus in textile units

$n_f \cdot \frac{D_f^{\,2} \cdot \pi}{4} = 0.1131\ \text{mm}^2$	Filament area estimation
$\frac{den_y}{\rho} = 0.1156\ \text{mm}^2$	Density estimation
$\frac{E_{textile} \cdot den_y}{E_{metric}} = 0.1158\ \text{mm}^2$	Back calculated estimation

Summary of Properties and Area Estimations

BioMid, 1650 denier

$n_f := 900$	Number of filaments in yarn
$D_f := 11\ \text{micron}$	Filament diameter
$den_y := 1650\ \text{den}$	Yarn denier (g/9000 m)
$\rho := 1.53\ \frac{\text{g}}{\text{cm}^3}$	Material density
$E_{metric} := 42\ \text{GPa}$	Modulus in metric units
$E_{textile} := \frac{315}{101.97}\ \frac{\text{N}}{\text{den}}$	Modulus in textile units

$n_f \cdot \frac{D_f^{\,2} \cdot \pi}{4} = 0.08553\ \text{mm}^2$	Filament area estimation
$\frac{den_y}{\rho} = 0.1197\ \text{mm}^2$	Density estimation
$\frac{E_{textile} \cdot den_y}{E_{metric}} = 0.1214\ \text{mm}^2$	Back calculated estimation

Appendix C: Uncertainty analysis

Table C-1 provides a list of the potential sources of experimental error throughout this work.

Table C-1: List of sources of error throughout experiments

Source	Error
500 N load cell	±0.5% of reading
5 kN load cell	±10 N
Crosshead position	±0.001 mm
BioMid™ denier	±5%
TBC dimension measurements	±0.0001 inch
DIC strain	±0.02% strain
Time	±0.001 s

The largest potential for error propagation in each set of experiments was determined to be the tensile strength. Here the measurement error propagation and uncertainty in each of these measurements will be discussed.

C.1 Breaking tenacity of dry yarns

For the dry yarn tests, the breaking tenacity was determined by converting the maximum load to units of grams-force per denier. Let P represent the load on the specimen, den the denier of the sample, and T the breaking tenacity of the yarn.

$$T = \frac{P \times conv}{den}$$

Thus, the error propagation in determining the breaking tenacity in units of grams-force per denier is given as:

$$\delta T = \left|\frac{P}{den}\right| \sqrt{\left(\left(\frac{\delta P}{P}\right)^2 + \left(\frac{\delta den}{den}\right)^2\right)}$$

The maximum load during testing was in the order of magnitude of 80 N and the denier of the BioMid™ yarns was reported as 1650 denier. The measurement uncertainty in breaking tenacity was thus determined to be approximately ±0.2 grams-force per denier for each

individual sample. Since a total of ten repetitions were performed for each specimen type and the mean used for analysis, this error reduces to:

$$\delta T_{mean} = \frac{\delta T}{\sqrt{N}}$$

Thus the uncertainty in the calculated mean breaking tenacity is ±0.08 grams-force per denier.

C.2 Tensile strength of composite strands

For the composite strand testing, the tensile strength was determined by the density area estimate and the maximum load. Again, let P represent the applied load, A the estimated cross-sectional area, and σ the calculated stress. Here, the area was calculated as a function of the yarn denier den and material density ρ. For the area estimate, the uncertainty is then:

$$\delta A = \left|\frac{den}{\rho}\right| \sqrt{\left(\left(\frac{\delta den}{den}\right)^2 + \left(\frac{\delta \rho}{\rho}\right)^2\right)}$$

The uncertainty in the stress calculation is a function of the area and load uncertainties:

$$\delta \sigma = \left|\frac{P}{A}\right| \sqrt{\left(\left(\frac{\delta P}{P}\right)^2 + \left(\frac{\delta A}{A}\right)^2\right)}$$

The greatest measurement uncertainty in the calculation of individual tensile strength values was approximately ±0.03 GPa. Again, using a total of $N = 10$ repetitions,

$$\delta \sigma_{mean} = \frac{\delta \sigma}{\sqrt{N}}$$

Thus the uncertainty in the calculated mean tensile strength is ±0.01 GPa.

C.3 Tensile strength of TBCs

The tensile strength of TBCs was determined by the maximum load and the measured cross sectional area. For the area measurement, three repetitions of each of the internal and external diameters were performed. Then, the area was determined individually for each specimen. Finally, the average area for each sample set (as determined by material and twist treatment) was used to calculate the stress.

The smallest internal diameter measurement was 0.3935” and the largest external diameter was 0.445”, while the precision of the micrometer was ±0.0001”. Three repetitions were made per measurement. As mentioned previously, the area calculation was as follows:

$$A_c = \frac{\pi\left(D_{avg}^2 - d_{avg}^2\right)}{4}$$

The uncertainty in an individual area measurement can be determined to be

$$\delta A_c = \sqrt{\left(\frac{\pi}{4} \cdot 2 \cdot D_{avg} \cdot \frac{\delta d}{\sqrt{3}}\right)^2 + \left(\frac{\pi}{4} \cdot 2 \cdot d_{avg} \cdot \frac{\delta d}{\sqrt{3}}\right)^2}$$

This propagation yields an area uncertainty of approximately ±0.00005 in^2, or ±0.3%. An average of a minimum of three specimens was used to determine the area, which was then in turn used to calculate sample stress. The greatest source of measurement error in the 5 kN load cell was noise from the data acquisition setup, on the order of approximately ±10 N. The highest peak load was recorded at about 1100 N. Thus, the individual specimen uncertainty in tensile strength can be found as

$$\delta\sigma_{ult} = \left|\frac{P}{A_c}\right| \sqrt{\left(\frac{\delta P}{P}\right)^2 + \left(\frac{\delta A_c}{A_c\sqrt{3}}\right)^2}$$

The individual specimen measurement uncertainty is thus approximately ±0.8 MPa.

Appendix D: Manufacturing drawings

D.1 Bollard-style test grips

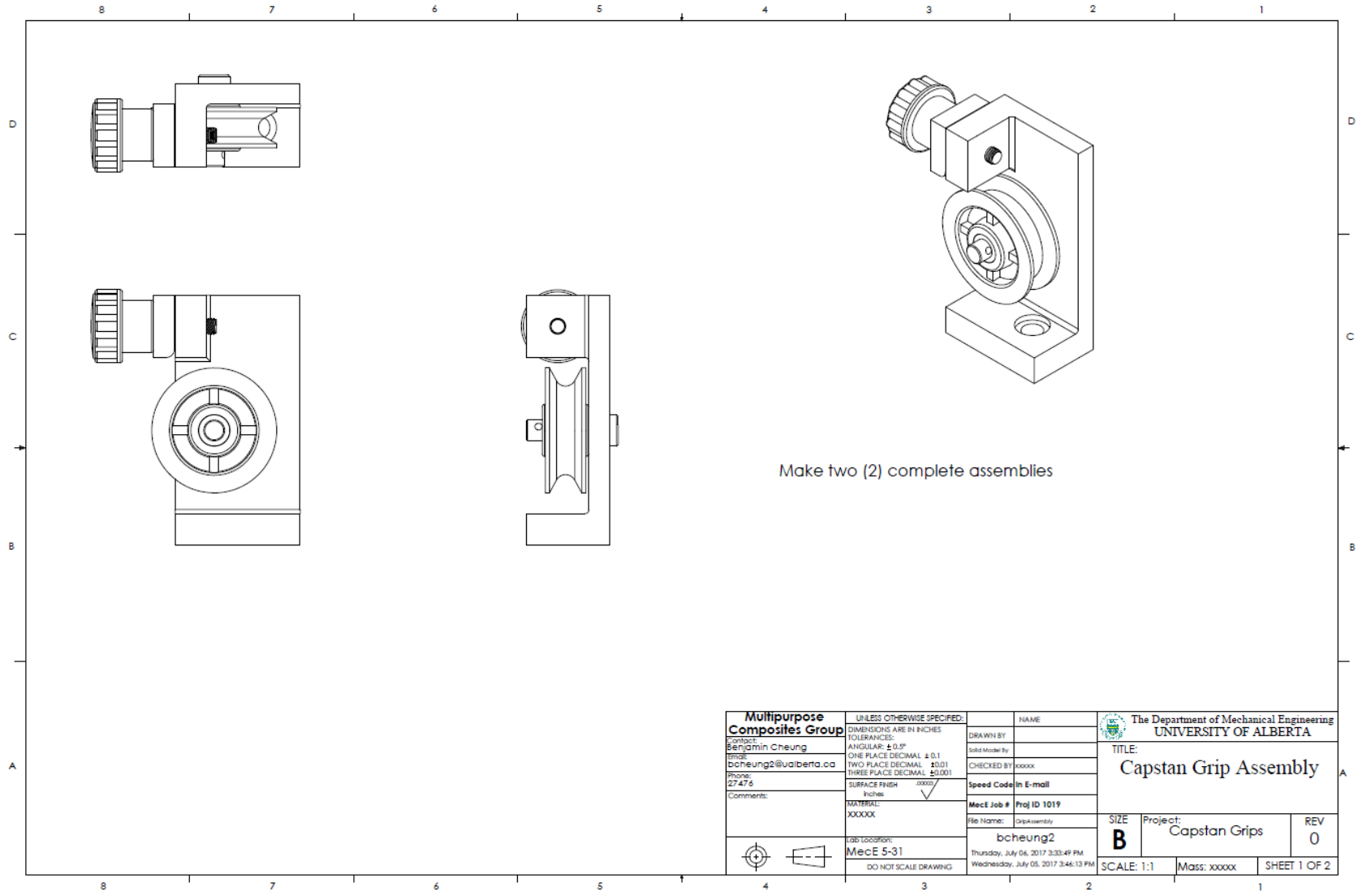

D.2 Calibration target

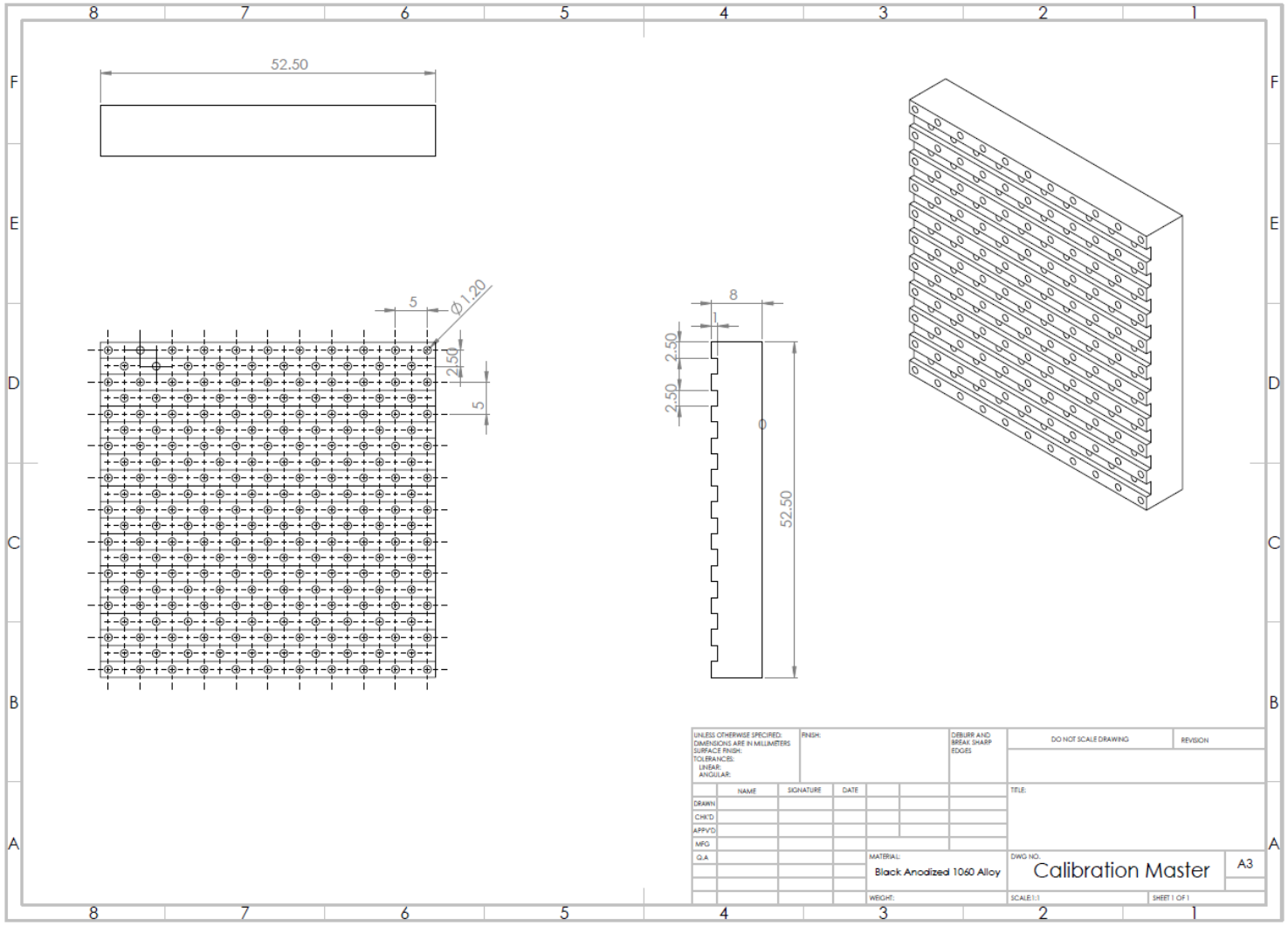

Appendix E: Matlab functions

As described previously, all of the raw data processing and calculation was performed in Matlab. In particular, three custom functions require particular attention

E.1 searchPiecewiseFunction

This function was used to determine the transition point of the BioMid™ yarns discussed in section 4.4.1.

```
function [leftModel, rightModel, ...
    xTransition, yTransition] = searchPiecewiseFunction(data)
%% FUNCTION NAME:
%   searchPiecewiseFunction
%
% DESCRIPTION:
%     searchPiecewiseFunction searches a set of x-y data for the point at
%     which a piecewise linear fit on either side of that point will
result
%     in the best regression fit for both sides of the function.
%
% INPUT:
%     data - (double) matrix of x-y data
%
% OUTPUT:
%     leftModel - (double) linear model prior to transition point
%     rightModel - (double) linear model after transition point
%     xTransition - (double) x value of transition point
%     yTransition - (double) y value of transition point
%
% ASSUMPTIONS AND LIMITATIONS:
%     - function can be well represented by a bilinear model
%     - values are monotonically increasing
%
% REVISION HISTORY:
%     09/01/2018 - bcheung2
%         * Initial implementation
%     05/24/2019 - bcheung2
%         * Formatting and header updated
%% Function

% Locate max peak to avoid regression calculating post failure
[maxLoad, maxSample] = findpeaks(data(:,2));

[~, absPeak] = max(maxLoad);

nSamples = maxSample(absPeak);

nBreak = round(nSamples/2);

breakMove = round(nSamples/4);

while breakMove ~= 1
```

```
43      nCounter = nBreak;
44      leftModel = fitlm(data(1:nBreak,1), data(1:nBreak,2));
45      rightModel = fitlm(data(nBreak:nSamples, 1),
data(nBreak:nSamples,2));
46      if leftModel.Rsquared.Ordinary < rightModel.Rsquared.Ordinary
47          nBreak = nBreak - breakMove;
48      else
49          nBreak = nBreak + breakMove;
50      end
51      breakMove = round(breakMove/2);
52  end
53
54  b1 = leftModel.Coefficients{1,1};
55  b2 = rightModel.Coefficients{1,1};
56  m1 = leftModel.Coefficients{2,1};
57  m2= rightModel.Coefficients{2,1};
58  xTransition    (bl-b2)/(m2-ml);
59  yTransition = (b2*ml-bl*m2)/(ml-m2);
60  end
```

E.2 naiveSearchRao

This function is an optimization that was used to determine the best fit of the anisotropic ratio for the Rao and Farris twist model, as mentioned in section 4.4.2.

```
function [df,s] = naiveSearchRao(d0, diff, x, y, conv)
%% FUNCTION NAME:
%   naiveSearchRao
%
% DESCRIPTION:
%     naiveSearchRao is a brute force optimization of the anisotropic
ratio
%     'd' based on the Rao and Farris twisted yarn model. It uses the
%     standard error of the regression to determine the model goodness of
%     fit for each guessed value.
%
% INPUT:
%     d0 - (double) initial guess of anisotropic ratio
%     diff - (double) width of search
%     x - (double) array of twist angles
%     y - (double) array of yarn modulus
%     conv - (double) minimum convergence required
%
% OUTPUT:
%     df - (double) optimal anisotropic ratio
%     s - (double) sum of square of errors for model at df
%
% ASSUMPTIONS AND LIMITATIONS:
%     - x and y are the same size
%     - values are monotonically decreasing
%
% REVISION HISTORY:
%     09/21/2018 - bcheung2
%         * Initial implementation
%     05/23/2019 - bcheung2
%         * Formatting and header updated

%% Search loop - Compares model error at 3 values of d
stest = 1;
n = 1;
while diff > conv
    d1 = d0 + diff; % New d value (high)
    d2 = d0 - diff; % New d value (low)
    ym0 = RaoFarrisCurve(x, d0); % Calculate model values w/ d0
    ym1 = RaoFarrisCurve(x, d1); % Calculate model values w/ d1
    ym2 = RaoFarrisCurve(x, d2); % Calculate model values w/ d2

    s(1) = sum((y-ym0).^2); % Sum of square errors for d0
    s(2) = sum((y-ym1).^2); % Sum of square errors for d0
    s(3) = sum((y-ym2).^2); % Sum of square errors for d0
```

```
45
46      if s(1) < s(2) && s(1) < s(3)
47          diff = diff*0.5; % Decrease search size and search again
48          %disp('Currently optimal, searching again');
49      elseif s(2) < s(1) && s(2) < s(3)
50          d0 = d1; % Move centre of search to d1
51          %disp('Decreasing anisotropic ratio');
52      elseif s(3) < s(2) && s(3) < s(1)
53          d0 = d2; % Move centre of search to d2
54          %disp('Increasing anisotropic ratio');
55      else
56          diff = diff*0.5; % Decrease search size
57          %disp('Decreasing search size');
58      end
59      df = dO;
60      n = n+1;
61      %disp(df);
62  end
63  outdisp = sprintf('%d iterations performed total',n);
64  disp(outdisp);
```

E.3 RamOsFit

This function performed the fitting of the Ramberg-Osgood equation to the stress strain data through a least-squares method.

```
function [E_linear, nRamOs, Sy, SyOffset, RamOsMdl, NE, sProp] =...
      RamOsFit(e, S, eLow, eHigh, alpha, sProp, plotOpt, plotTitle)
% FUNCTION NAME:
%     RamOsFit
%
% DESCRIPTION:
%       RamOsFit is a least-squares method of fitting the Ramberg-Osgood
%       equation to stress-strain results.
%
% INPUT:
%      e - (double) sample strain, in %
%      S - (double) sample stress, in MPa.
%      eLow - (double) lower limit for modulus calc
%      eHigh - (double) strain limits modulus calc
%      alpha - (double) yield offset, in % strain (i.e. 0.2)
%      sProp - (double) proportional limit for linear elastic region
%
% OUTPUT:
%      E_linear - (double) linear modulus for elastic region
%      nRamOs - (double) Ramberg-Osgood power exponent
%      Sy - (double) Ramberg-Osgood yield value
%      SyOffset - (double) yield strength at alpha offset
%      RamOsMdl - (mdl) linear regression results
%
% ASSUMPTIONS AND LIMITATIONS:
%      - e and S are the same size
%      - there is a distinct linear region and plastic region
%
% REVISION HISTORY:
%      02/07/2019 - bcheung2
%          * Initial implementation

%% Linear modulus of stress-strain curve in elastic region

err = 1; % Initialize error for while loop
% Loop regression and shift until aligned with origin
while abs(err)>0.01
     mod = fitlm(e(e > eLow & e < eHigh), S(e > eLow & e < eHigh));
     err = -mod.Coefficients{1,1}/mod.Coefficients{2,1};
     e = e - err;
end
xInt = err; % Exact value of x-intercept
%% Create Offset Line
m = mod.Coefficients{2,1};  % Slope equal to elastic modulus
b = -m*(xInt + alpha); % Y-intercept of offset line
```

```
% Offset vector
offsetY = linspace(0, max(S),1000);
offsetX = (offsetY - b)./m;
%% Intersection from offset line
[eyOffset, SyOffset, ~, ~] = intersections(e, S, offsetX, offsetY);
% Check to see if intersection is there. If not, use max stres
if isempty(SyOffset) == 1
     SyOffset = max(S);
end
%% Fit Ramberg-Osgood function to plastic portion
ep = e - S/mod.Coefficients{2,1} - xInt; % Remove linear strain portion
E_linear = mod.Coefficients{2,1}/10;  % Return linear modulus
% Introduce loop to optimize based on increasing proportionality limit

RMSEOld = 1;
while 1
% Linear regression of log(S) vs log (ep)

       RamOsMdl_temp = fitlm(log(ep(e > eHigh   & S < SyOffset & S >
sProp)),...
           log(S(e > eHigh   & S < SyOffset& S > sProp)));  %& ep > 0.02
       nRamOs_temp = real(1/RamOsMdl_temp.Coefficients{2,1});  % Equation
exponent
       Sy_temp = real(exp(RamOsMdl_temp.Coefficients{1,1})*...
           alpha^(RamOsMdl_temp.Coefficients{2,1}));  % Yield at offset

       %% Create Ramberg-Osgood model

       RMSE_Model = RamOsMdl_temp.RMSE;

       sProp = sProp + 1;
       if RMSE_Model > RMSEOld % If error is worse than previous iteration
           break
       elseif sProp > SyOffset
           break
       end
       RMSEOld = RMSE_Model;
       RamOsMdl = RamOsMdl_temp;
       nRamOs = nRamOs_temp;
       Sy = Sy_temp;

end
eModel = real(S/m + alpha*(S/Sy).^nRamOs);
sProp = sProp - 1;

%% Create plot (optional)
if plotOpt == 'y'
       figure()
       hold on
       plot(e,S) % Scatterplot original dataset with shift correction
```

```
94        plot(eModel, S) % Plot model
95        plot(offsetX, offsetY) % Plot yield offset at alpha
96        title(plotTitle)
97        legend('Experimental Data',...
98            strcat(['Ramberg-Osgood at n = ',num2str(nRamOs,3)]),...
99            strcat(num2str(alpha),'% offset line'),...
100           'location', 'southeast');
101       xlabel('Strain [%]')
102       ylabel('Stress [MPa]')
103       txtSlope = {strcat(['\leftarrow E = ',num2str(m/10,3),' GPa, ',...
104           'R^2 = ',num2str(mod.Rsquared.Ordinary,4)])};
105       text((eHigh),m*(eHigh),txtSlope)
106       txtInt = {strcat([num2str(alpha),'% offset']),...
107           strcat(['e_y = ',num2str(eyOffset,3),'%']),...
108           strcat(['S_y = ',num2str(SyOffset,3),' MPa'])};
109
110       txtMdl = {'Ramberg-Osgood model',...
111           strcat(['S_y = ',num2str(Sy, 3),' MPa, R^2 = ',...
112           num2str(real(RamOsMdl.Rsquared.Ordinary),4)])};
113       if isempty(eyOffset) == 0
114           text(eyOffset, SyOffset, txtInt,...
115               'HorizontalAlignment','right',...
116               'VerticalAlignment', 'bottom')
117           text(eyOffset, SyOffset, txtMdl,...
118               'HorizontalAlignment','left',...
119               'VerticalAlignment', 'top')
120       end
121      % figure()
122      % scatter(log(ep(S>sProp & S < Sy)), log(S(S>sProp & S < Sy)))
123
124   end
125   %% Calculated normalized error of actual stress-strain values
126   NE = 100*sqrt(mean((eModel(e > eHigh & S < Sy) -...
127         e((e > eHigh & S < Sy))).^2))/eyOffset;
128   end
```